Magdalena Temmel, BSc

Spatio-temporal pattern analysis of Alzheimer´s disease-related vascular pathology in human and transgenic mouse brain

MASTER'S THESIS

to achieve the university degree of

Master of Science

Master's degree programme: Biochemistry and Molecular Biomedical Sciences

submitted to

Graz University of Technology

Supervisor

Ao.Univ.-Prof., Mag. Dr. Heinz Hutter

Institute of Cell Biology, Histology and Embryology
Medical University of Graz

in cooperation with QPS Austria GmbH

Graz, April 2015

AFFIDAVIT

I declare that I have authored this thesis independently, that I have not used other than the declared sources/resources, and that I have explicitly indicated all material which has been quoted either literally or by content from the sources used. The text document uploaded to TUGRAZonline is identical to the present master‘s thesis dissertation.

Date

Signature

“As a special thank, I dedicate this master´s thesis to my family and friends for their love and support.”

PREAMBLE

In order to gain my degree as Master of Science at the Graz University of Technology I wrote my empiric work entitled „Spatio-temporal pattern analysis of Alzheimer´s disease-related vascular pathology in human and transgenic mouse brain“ at QPS Austria, supervised by Dr. Heinz Hutter from the Medical University of Graz.

At this point I would like to thank all persons who supported me by creating this master´s thesis.

A special thank goes to Dr. Birgit Hutter-Paier, head of the Neuropharmacology department at QPS Austria, for the possibility of the traineeship. Additionally I would particularly like to thank Dr. Heinz Hutter from the “Institute of Cell Biology, Histology and Embryology” from the Medical University of Graz for the supervision and Daniel Havas, MSc., head of the histological department at QPS Austria, who supported me in all phases of my work. Furthermore I deeply thank Dr. Johannes Attems for his support during the provision of human brain samples and further cooperation.

Last but not least I´m very grateful to the whole QPS Austria histology team for assistance.

This work was founded by a grant from the Österreichische Förderungsgesellschaft mbH (FFG) (844453).

ABSTRACT

During recent years, evidence for a connection between neurovascular dysfunction and the pathogenesis of Alzheimer's disease (AD) has accumulated. Alterations in the brain vasculature, such as microvascular atrophy, decreased clearance of amyloid β (Aβ), and loss of astrocytic water channels, have been shown to occur in the progression of the disease. The current study was designed to investigate whether vascular changes may be similar in human AD and in the transgenic APP_{SL} mouse model.

Using indirect immunofluorescence and quantitative image analysis, AD-associated vascular changes in cortical areas of healthy and diseased human brain sections and both transgenic APP_{SL} mice and non-transgenic controls were investigated. I initially replicated established findings in humans and investigated APP_{SL} mice in parallel. Readouts were AD-associated accumulation of Aβ and occurrence of cerebral amyloid angiopathy (CAA); the suitability and validity of the quantitative approach was confirmed during this phase. As expected, the analysis revealed that the amount of Aβ deposits in the isocortex and hippocampus positively correlates either with AD progression (as determined by Braak stage) on human tissue or with age on mouse tissue. Furthermore, the occurrence and progression of CAA is associated with age in APP_{SL} mice, whereas a positive correlation of CAA and Braak stage was less obvious in human AD, because only a few human samples showed CAA probably due to methodical reasons. The approach was then extended to test AD-related hypotheses on collagen IV, and the data show total intensity of collagen IV immunofluorescence increases similarly in the hippocampus of transgenic mice and AD individuals. Detailed analysis revealed that in mice this is due to enlargement of existing blood vessels, whereas in human subjects it is associated with an increasing numerical density of blood vessels. The evaluation of aquaporin 4-immunofluorescence suggests that these water channels may be expressed following complex spatio-temporal patterns in humans and transgenic mice. An abnormally low amount and a delocalization of isocortical aquaporin 4 were detected at early Braak stage, and, if confirmed by independent investigations, this could be potentially useful as an early marker for AD.

In conclusion, the present study supports the notion that APP_{SL} mice represent a useful model for several aspects of human AD histopathology.

ZUSAMMENFASSUNG

In den letzten Jahren haben sich Hinweise verdichtet, die auf eine Verbindung zwischen neurovaskulärer Dysfunktion und der Pathogenese der Alzheimer-Krankheit (AD) deuten. Es wurde deutlich, dass Veränderungen in den Blutgefäßen des Gehirns – wie mikrovaskuläre Atrophie, verminderte Beseitigung von Amyloid β (Aβ) und Verlust von wassertransportierenden Kanalproteinen in Astrozyten mit dem Fortschreiten der Krankheit assoziiert sind. Die vorliegende Studie wurde durchgeführt, um zu untersuchen, ob sich ähnliche Gefäßveränderungen in den Gehirnen menschlicher AD-Patienten und im transgenen APP_{SL} Mausmodell nachweisen lassen.

Mittels indirekter Immunfluoreszenz und quantitativer Bildanalyse wurden AD-assoziierte vaskuläre Veränderungen in kortikalen Schnitten des gesunden und erkrankten menschlichen Gehirns sowie in transgenen APP_{SL} Mäusen und nicht-transgenen Kontrolltieren untersucht. Zunächst wurden gesicherte Erkenntnisse zur AD-Histopathologie bei Menschen repliziert und die Methoden in Parallelexperimenten auf APP_{SL} Mäuse ausgedehnt. Die Bestimmung AD-assoziierter Akkumulation von Aβ und das Auftreten von zerebraler Amyloid-Angiopathie (CAA) dienten dazu, die Eignung und die Wirksamkeit des quantitativen Ansatzes zu bestätigen. Wie erwartet zeigte sich, dass die Menge an Aβ-Ablagerungen im Isokortex und Hippocampus am menschlichen Gewebe mit dem Fortschreiten der AD-Erkrankung korreliert (bestimmt durch das Braak-Stadium), während beim Mausgewebe eine Korrelation mit dem Lebensalter nachweisbar ist. Bei APP_{SL} Mäusen zeigte sich ein ähnlicher Zusammenhang zwischen dem Alter der Tiere und dem Beginn und Fortschritt der CAA, während eine positive Korrelation von CAA und Braak-Stadium in menschlichem Gewebe weniger offensichtlich war; hierbei könnten methodische Gründe eine Rolle spielen, denn nur wenige menschliche AD-Proben zeigten eine eindeutige CAA. Der quantitative Ansatz wurde dann erweitert um Hypothesen zu testen, die die gesteigerte Expression von Kollagen IV mit AD in Verbindung bringen. Die Daten zeigen, dass die Gesamtintensität der Kollagen IV-Immunfluoreszenz im Hippocampus sowohl von AD-Betroffenen als auch in transgenen Mäusen in ähnlicher Weise ansteigt. Die detaillierte Analyse verdeutlicht, dass der Anstieg von Kollagen IV bei Menschen vermutlich auf die zunehmende Häufigkeit von Blutgefäßen zurückzuführen ist,

während bei Mäusen die Vergrößerung bestehender Blutgefäße ursächlich scheint. Die Auswertung der Aquaporin 4 (AQP4)-Immunfluoreszenz legt nahe, dass diese Wasserkanäle komplexe räumliche und zeitliche Expressionsmuster in Menschen und transgenen Mäusen aufweisen. Eine erhöhte Menge und eine Delokalisierung der AQP4-Expression wurde in frühen Braak-Stadien festgestellt; falls diese Ergebnisse in unabhängigen Untersuchungen bestätigt werden, könnte vermindertes isokortikales AQP4 als früher Nachweis für AD im Menschen etabliert werden.

Die Ergebnisse der vorliegenden Studie stützen zusammengefasst die Annahme, dass APP_{SL} Mäuse ein nützliches Modell für verschiedene Aspekte der menschlichen AD Histopathologie darstellen.

CONTENT

1 INTRODUCTION

Alzheimer´s Disease (AD) is a progressive neurodegenerative disease and is today´s most common form of senile dementia[1]. Other degenerative and non-reversible dementias are, for example, vascular dementia (VaD)[2], Lewy Body dementia, and frontotemporal dementia[3]. The prevalence of all of them increases with age. In detail, within the age group of 65-69 years seven of 1000 women and six of 1000 men suffer from dementia, whereas in the age group of 85-89 years 140 women of 1000 and 90 men of 1000 have dementia. In total, 60 to 80 % of all dementia cases belong to AD[4].

AD is characterized by progressive behavioral and cognitive impairment. Histopathologically, positive features are neurofibrillary tangles, amyloid plaques, glial response and cerebral amyloid angiopathy, and negative features are synaptic and neuronal loss[5,6]. Currently, *post mortem* diagnosing of AD is based on neurofibrillary tangle staging and on semi quantitative evaluation of neuritic plaque load corresponding to the "Consortium to Establish a Registry for Alzheimer's Disease" (CERAD)-criterion[7].

1.1 Etiology of Alzheimer´s Disease

According to the time of disease outbreak, AD can be classified into early-onset AD (EOAD) and late-onset AD (LOAD)[8].

EOAD occurs in less than 1 % of all cases and is characterized by an onset before the age of 65. It is typically an autosomal dominant, familial disease, which is caused by mutations in the presenilin-1 *(PSEN1)* and presenilin-2 *(PSEN2)* genes, as well as in the gene encoding amyloid precursor protein (APP)[8,9]. Within this gene more than 30 missense mutations have been identified, whereof approximately 25 are considered as pathogenic[8]. In general, these mutations lead to an altered processing of APP[10]. The *PSEN1* gene is located on chromosome 14, *PSEN2* on chromosome 1 and *APP* on chromosome 21. According to that, people who suffer from Down´s syndrome, which means the chromosome 21 is triplicated, produce 1.5-fold more APP than normal, and consequently the disease appears already in early adulthood[11].

LOAD starts late in life, typically at 65 years and older. It occurs spontaneously and heterogeneously[8]. As the epidemiology indicates, the age is the most important factor for developing AD, followed by sex. In total more women suffer from the disease compared to men. Overall this depends on the fact that women have longer life expectancy than men and therefore the age-depending factor applies[11]. Additionally, it has been suggested that a decreased level of circulating estrogen in postmenopausal women may negatively influence the outbreak of the disease. Consistent with this notion, the onset may be delayed by a postmenopausal estrogen replacement therapy[11,12]. Besides age and sex also genetic and environmental factors are thought to be causatively related to LOAD[8].

Furthermore, additional allele variations in the apolipoprotein E *(APOE)* locus, located on chromosome 19, were identified as a significant risk factor in LOAD[13,6]. As there is a connection between AD and the microvascular pathology, a number of risk factors such as atherosclerosis, stroke, hypertension or hyperlipidemia overlap between AD and VaD[14]. Altogether about 90 % of all AD cases occur sporadically whereas the remaining cases are of genetic origin[9].

1.2 Histopathological Features of Alzheimer´s Disease

In general, the main histopathological characteristics of AD are the neurofibrillary tangles, amyloid plaques, glial response, cerebral amyloid angiopathy, synaptic and neuronal loss[6].

Each of these modifications has its characteristic distribution pattern. For instance, plaques in general were regarded to be located throughout the cortical mantle, whereas the neurofibrillary tangles were found mostly in the limbic system and associated cortices[6].

1.2.1 Macroscopic Alterations

A typical feature of AD is weight loss of the whole brain[9] probably due to a cortical atrophy mostly affecting the medial temporal lobe and partly the primary motor, sensory and visual cortex (CTX)[6].

1.2.2 Classical Microscopic Alterations

Microscopically two essential hallmarks can be observed in AD - on the one hand the neurofibrillary tangles and on the other hand the amyloid plaques[9,15], which were already mentioned in Alzheimer's initial description[16].

1.2.2.1 *Neurofibrillary Tangles*

Under physiological conditions, the microtubule-associated protein "tau" is located to the axon, where it binds and stabilizes microtubules and thereby takes part in axonal transport[6].

Development and Composition of Neurofibrillary Tangles

Under pathological conditions the protein is hyperphosphorylated, misfolded and aggregated and is furthermore translocated to the somatodendritic compartment. This abnormal tau species is the major compound of neurofibrillary tangles (NFTs)[6]. The term refers to a structure that is made up of so-called paired helical filaments, which are intracellular fibrils with a diameter of about ten nanometer forming filaments with a helical three-dimensional conformation[6]. If tangle-bearing neurons die and the cellular structures are removed so-called "ghost" tangles can remain in the extracellular space[6].

Distribution of Neurofibrillary Tangles

The increase of the NFTs follows a stereotypical spatio-temporal pattern and is therefore predictable. Importantly, it correlates with the progression of the cognitive decline[6]. Based on that, Braak and Braak defined six stages[17], which can be merged into three neuroanatomical phases: 1) [I/II] entorhinal, 2) [III/IV] limbic and 3) [V/VI] isocortical (see Figure 1). Stage I is characterized by the formation of NFTs in the transentorhinal region, along with the entorhinal CTX. In stage II NFTs are evident in the CA1 (cornu ammonis area 1) of the hippocampus (HC). In stage III NFTs spread to the limbic structures (e.g. subiculum) and in stage IV into the amygdala, the thalamus and the claustrum. Thereafter NFTs develop in all cortical regions (stage V) and finally at stage VI in the primary sensory, visual and motor areas. Additionally within this stage the striatum and the substantia nigra might be affected[6].

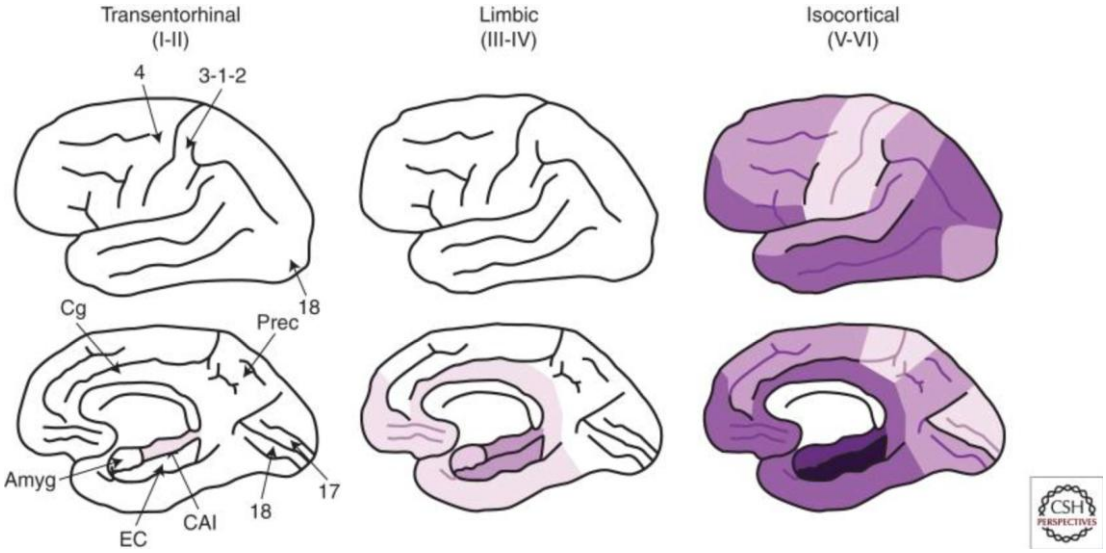

Figure 1: Braak stages associated with the spatio-temporal pattern of NFT development. Violet shading represents the distribution of NFTs, whereupon darker colors indicate an increasing density. Amyg = Amygdala, EC = Entorhinal cortex, CA1 = Cornu ammonis area 1, Cg = Cingulate cortex, Prec = Precuneus, 4 = Primary motor CTX, 3-1-2 = Primary sensory CTX, 17 = Primary visual cortex, 18 = Associative visual cortex. Figure and information was taken from[6].

1.2.2.2 *Amyloid Plaques*

Amyloid plaques denote the abnormal extracellular deposition and accumulation of the amyloid β (Aβ) peptide, mainly with sizes of 40 (Aβ40) or 42 (Aβ42) amino acids[6].

APP Processing and Amyloid Plaque Composition

The Aβ peptides are cleavage products of the amyloid precursor protein. Two independent proteolytic pathways, the non-amyloidogenic and the amyloidogenic one, are involved in the processing of APP (Figure 2). Within the non-amyloidogenic pathway first the α-secretase cuts APP, which leads to the release of the extracellular terminus – the „secreted amyloid precursor protein-α" (sAPPα). Thereafter the γ-secretase cleaves the now 83-residue carboxy-terminal fragment, thereby generating the extracellular p3 and the amyloid intracellular domain (AICD). Within the amyloidogenic pathway, first the β-secretase, named β-site amyloid precursor protein cleaving enzyme 1 (BACE-1) cleaves APP and creates a „secreted amyloid precursor protein-β" (sAPPβ) fragment and the C-terminal C99 peptide. This C99 fragment is furthermore split by the γ-secretase, leading to the creation of an AICD but also Aβ fragments[18] (see Figure 2).

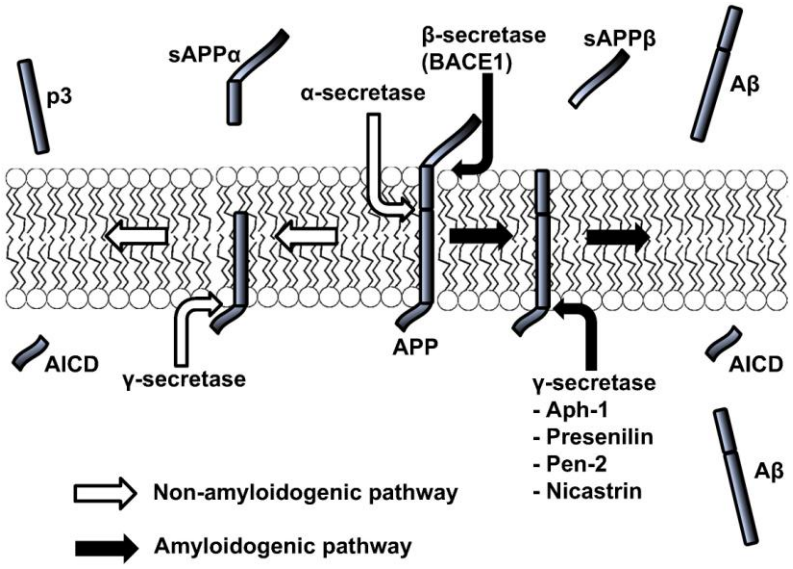

Figure 2: Schematic representation of the non-amyloidogenic and amyloidogenic pathway of amyloid precursor protein processing. The left side of the image represents the non-amyloidogenic pathway, whereby the α-secretase initially cleaves the APP and generates sAPPα and a C83 fragment, which then is separated by the γ-secretase into p3 and AICD. The right side shows the amyloidogenic pathway. This pathway is initiated by BACE-1 and causes the releasing of the sAPPβ. The retained C99 peptide is then also cleaved by the γ-secretase, generating the Aβ and also the AICD peptides. Aph-1 = anterior pharynx-defective 1, Pen-2 = presinilin enhancer 2. Figure and information was taken from[8].

Due to unknown reason, the Aβ monomers can aggregate into oligomers and finally accumulate in the form of amyloid plaques in the brain[19].

The „Amyloid Cascade Hypothesis“

Following the discovery of Aβ, the “Amyloid Cascade Hypothesis” was developed, which is today considered as the most constant and influential theory of the molecular pathology of AD. The main idea of this model is that the development of Aβ peptides is an initial event in AD, first causing the formation of amyloid plaques and NFTs, and later incorporating other proteins such as apolipoprotein E and ubiquitin into the process. This cascade of detrimental effects is thought to finally lead to cell death and dementia[20].

Classification of Amyloid Plaques

Based on the molecular composition of the amyloid plaques, various morphological forms have been described, including diffuse (“pre-amyloid”), primitive (“immature”), classic (“neuritic”) and compact-type (“burnt-out”) plaques[21].

The Aβ42 peptides are less soluble, they exhibit a high rate of fibrillization, and they occur a higher percentage within plaques compared to Aβ40 peptides[6].

Classic or neuritic plaques are characterized by a dense central core, mostly composed of Aβ40, and a less compact peripheral halo predominantly consisting of Aβ42. The primate or immature plaques are spherical deposits of mainly Aβ42 being dispersed within the neuropil, and they are missing a defined core. The compact or burnt-out plaques are composed of a dense core enriched with Aβ40. Diffuse plaques are similar to primitive plaques, but with irregular contour and shape. They often surround neurons and glia cells[21].

Plaques sometimes show perivascular orientation, usually in association with cerebral amyloid angiopathy. Microglia may join the dense central core and reactive astrocytes often encircle the border of plaques, especially those with a dense core[21].

Distribution of Amyloid Plaques

Based on the progress of amyloid deposition an alternative system for classifying and staging of AD pathology has been developed by Thal et al. in 2002 (see chapter 1.2.2.1 for staging based on NFTs). This system uses Campbell-Switzer silver staining and immunohistochemistry to visualize amyloid[22]. Initially the amyloid deposits occur in isocortical structures (stage 1 or isocortical), followed by limbic and allocortical areas (stage 2 or limbic), and finally in subcortical structures including basal ganglia, selected nuclei in diencephalon and brainstem, and the cerebellum (stage 3 or subcortical) (Figure 3)[6].

Figure 3: Spatio-temporal pattern of progression of amyloid plaque deposition. Coronal (A) axial (B) and sagittal (C) section through the brain. The five Thal stages of amyloid deposition are summarized in three stages. Deposition starts in isocortical areas (stage 1, red), followed by limbic and allocortical structures (stage 2, orange), and finally includes subcortical areas (stage 3, yellow). Amyg = Amygdala, EC = Entorhinal cortex, Hipp = HC, Cg = Cingulate cortex, Cd = Caudate nucleus, Put = Putamen, Gpe = Globus pallidus externus, Gpi = Globus pallidus internus, Cl = Claustrum, Ins = Insular cortex, Die = Diencephalon, Mid = Midbrain, Med = Medulla oblongata, Cblm = Cerebellum. Figure and information was taken from[6].

1.2.3 Cerebrovascular Alterations in Alzheimer´s Disease

Beside additional changes, such as a glial response or neuronal and synaptic loss[9,15], approximately 60% of AD patients are present with vascular modifications[23]. These changes include cerebral amyloid angiopathy, an impaired blood-brain-barrier (BBB), decreased microvascular density, changes in vessel diameter, heterogeneity of blood flow, and accumulation of collagen or other proteins[15]. Increasing evidence supports the notion that different vascular factors may promote the pathogenesis of LOAD[3] or be even upstream of the amyloid cascade. It is currently unknown whether these abnormalities are the initial cause for the development of the disease or if they appear as a consequence of AD[3]. Fact is, that microvascular alterations reduce the cerebral blood flow, consequently leading to decreased oxygen saturation, and a reduction of energy substrates and nutrients in the brain. This may interfere with proper clearance of neurotoxic molecules that falsely accumulate in the interstitial fluid or in brain cells[24].

The cerebral blood system originates from large arteries at the base of the brain, the so-called “Circle of Willis”. These large arteries run through the dura mater and branch into leptomeningeal and pial arteries also at the surface of the brain. The pial arteries further branch into penetrating intracerebral arteries and arterioles, with a diameter of 20-90 micrometer in the human brain[10].

1.2.3.1 *Pial and Intracerebral Arteries*

Physiological Cerebral Vascular Architecture

The pial arteries run within the sub-arachnoid space along the brain surface. Surrounded by cerebrospinal fluid (CSF), pial vessels branch into smaller arteries that are able to penetrate into the Virchow-Robin space, an extension of the subarachnoid space[25]. They enter the brain neuropil and split into smaller vessels—the parenchymal arterioles—that are surrounded by astrocytic end-feet which constitute part of the BBB (see Figure 4)[26,27]. The wall of cerebral arteries is composed of three layers, the tunica intima, tunica media and tunica adventitia. The tunica intima is built up of endothelium, the tunica media mainly consists of vascular smooth muscle cells and the tunica adventitia is constituted from collagen, fibroblasts and nerves[10]. The dense mesh of parenchymal arteries ensures sufficient supply of oxygen to the neuronal network[28,29].

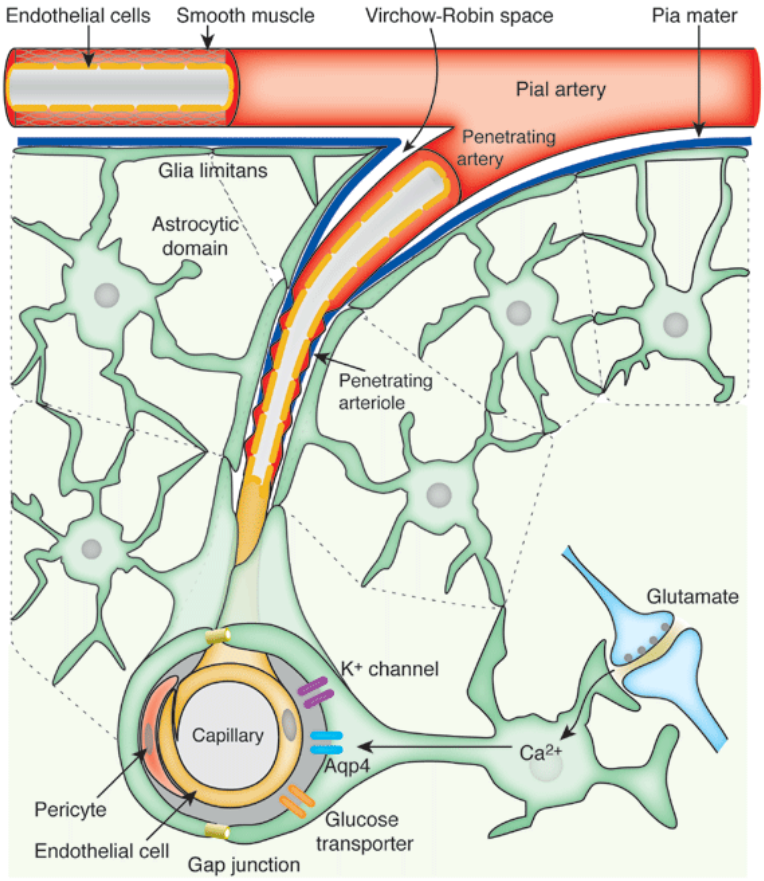

Figure 4: Scheme of pial arteries that run along the surface of the brain and branch into smaller arteries that penetrate into the Virchow-Robin space and further into the brain neuropil, thereby becoming parenchymal arterioles. Aqp4 = aquaporin 4, Ca^{2+} = calcium, K^{+} = potassium. Figure and information was taken from[29].

The structure and the function of pial arteries differ in some aspects from parenchymal arterioles. First, pial arteries are “extrinsically” innervated, which means they are innervated perivascular by the peripheral nervous system, whereas the parenchymal arteries are “intrinsically” innervated by neurons of the central nervous system. Another difference is the amount of smooth muscles. The parenchymal arterioles contain just one layer of circumferentially running smooth muscle cells and a higher myogenic basal tone which is largely insensitive to modulation by neurotransmitters[30]. Last but not least, the pial vessels are structured as an effective network, where an occlusion of one vessel is compensated by others. The penetrating and parenchymal arterioles in contrast are long and each one supplies blood to a spatially segregated area. Consequently, the occlusion of a single arteriole leads to a significant reduction in the blood flow, and to damage of the surrounding local tissue[31].

Histopathological Alterations of Cerebral Vascular Architecture in AD – Cerebral Amyloid Angiopathy

In addition to the deposition of the amyloid plaques within the parenchyma, the amyloid spreads into the wall of pial and intracranial vessels – leading to the cerebral amyloid angiopathy (CAA)[6,32]. Aβ is predominantly localized in pial and cortical arteries, but also in cerebral capillaries[33]. Venules, veins and white-matter arteries in contrast are rarely affected[6]. It has been reported that the vascular dysfunction may cause neuronal dysfunction and neurodegeneration and support the development of cerebrovascular 'storage' disorders, such as β-amyloidosis and CAA[24]. The CAA occurs also in 30-40% in non-demented elderly people; the prevalence, however, rises to 60-95% in AD brains[33].

The major part of CAA consists of the Aβ40 peptides, which are more soluble than the Aβ42 peptides. Aβ preferably accumulates in the interstitium, in detail between the smooth muscle cells of the tunica media[6]. The mechanism how and why CAA occurs is not fully understood, but there is a significant body of evidence indicating that Aβ accumulates in the wall of cerebral vessels and also in the brain parenchyma, because of an impaired balance between Aβ production and Aβ clearance[10]. Another alteration of the pial and intracranial vessel is the reduction of the smooth muscle layer which leads to a damaged vessel wall and consequently intracerebral bleeding[32].

1.2.3.2 *Brain Capillaries*

Physiological Cerebral Capillary Architecture and the Blood-Brain-Barrier

Intracerebral arteries branch into arterioles and capillary microvasculature with a diameter of six to ten micrometer[10]. In total the length of the capillaries within the brain is about 640 kilometers. Primarily, the oxygen and nutrient exchange occurs at the capillary bed of the brain, which is a dense network comprised out of intercommunicating blood vessels that consist of specialized endothelial cells and no smooth muscles[26,14]. At any time, all capillaries of the brain are perfused with blood[14]. The brain makes up 2 % of the total body weight, however it consumes 15-20 % of the total cardiac output, which leads to the fact, that the brain is obviously a highly perfused organ[28]. In general, there is a tight relationship between the neuronal and vascular compartments[34]. For instance it has been reported, that nearly every neuron has direct access to a capillary[32]. Depending on the location

and the locally required energy, the frequency of brain capillaries varies. Therefore there is a higher capillary density in the gray versus white matter[35].

In total there are three main interfaces within the brain – the blood-CSF interface, the CSF-blood interface and the blood-brain interface. Epithelial cells of the choroid plexus form the CSF-blood barrier is built by the vascular arachnoid epithelium. The largest barrier is the BBB, which is formed by the cerebral endothelium. In general its function is to protect the brain on the one hand from blood-borne particles and pathogens and on the other hand to maintain the homeostasis and an optimal milieu for neuronal activity[36,37].

The function and the integrity of the BBB are organized by the “neurovascular unit”, which is built up of vascular endothelial cells, pericytes, astrocytes and neurons. The endothelial cells are hold together by tight junctions and cover the cerebral microvessels, thereby forming a physical barrier—the core of the BBB—that enables limited paracellular diffusion. In contrast to the leaky vessels of the periphery, the cerebral microvessels have no fenestration. A part of the basal membrane, the basal lamina, and the end-feet of astrocytes encircle these endothelial cells, together constituting the neurovascular unit (see Figure 5)[5,19].

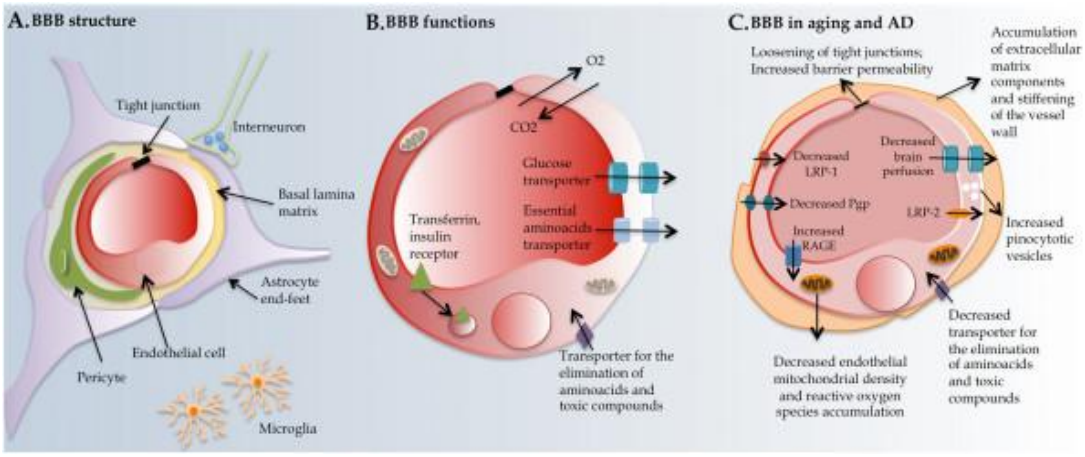

Figure 5: Scheme representing the structure, function and alteration of the BBB under physiological and pathological conditions. The core of the BBB is formed by endothelial cells, which are connected by the so-called tight junctions. The central BBB is surrounded by the basal lamina, pericytes and astrocytic end-feet (A). Transporters and receptors on the basolateral and apical side of endothelial cells are able to transport molecules into and out of the brain transfer receptor-mediated signals in both directions (B). Under pathological circumstances the normal activity of the endothelial cells alters (C). CO2 = carbon dioxide, O2 = oxygen, LRP-1 = low density lipoprotein receptor-related protein 1, LRP-2 = low density lipoprotein receptor-related protein 2, RAGE = receptor for advanced glycation endproducts. Image and information was taken from[19].

Astrocytes, the most frequent glia cells in the central nervous system (CNS)[38], are located between capillary endothelial cells, pericytes and neurons, and

communicate with these cells via their “foot processes”[14]. They fulfill multiple roles in organizing and maintaining brain structure and function, e.g. they are involved in synaptic transmission or neurovascular coupling[38]. Furthermore astrocytes influence the cerebral blood flow. For example they regulate local CNS blood flow in response to changes in neuronal activity or they produce a large variation of molecules, such as prostaglandins or nitric oxide which alter CNS blood vessel diameter and blood flow[39]. The function of astrocytes depends on the amount and composition of channel proteins, which are located within the cell membrane and enables the transport of water and ions into and/or out of the cells[38].

Today, at least 13 members of the aquaporin (AQP) family are known in mammals[40]. From these, three—AQP1, AQP4 and AQP9—are expressed in the CNS[41,42]. AQP4, the predominant water channel in the brain, is located in astrocytic end-feet, where it permits the passage of water and therefore contributes to fluid homeostasis of the CNS[39,43,44] (see Figure 4).

Histopathological Alterations of Cerebral Capillary Architecture in AD – Changes of the Neurovascular Unit or the Blood-Brain-Barrier

BBB dysfunction has been reported in the pathogenesis of different neurodegenerative disorders, such as AD, Parkinson´s disease or multiple sclerosis[14]. Alterations of the neurovascular unit in AD include focal necrosis of the endothelium, reduction of mitochondrial density in the endothelium, decreased amount of tight junctions, alterations of astrocytic end-feet and less elasticity of the vascular wall (Figure 5)[19].

Zlokivic tried to combine different models, which might explain the pathway or pathways of AD, focusing on the neurovascular unit. At the early symptomatic phase reduced blood flow and impaired BBB clearance of Aβ cause accumulation of neurotoxic Aβ oligomers in the brain. The hypoperfusion and the accumulated Aβ oligomers can both start the neuronal injury. The combination of the distinct reduction in cerebral blood flow, activation of the endothelium and pericytes, loss of BBB Aβ clearance function, enhanced accumulation of Aβ in the brain, and activation of astrocytes and microglia lead to impaired synaptic transmission and neuronal function. Furthermore, NFTs may accumulate in neurons in response to both ischemic injury and Aβ deposition. In late stages the degeneration of the endothelial cell wall and pericytes prohibits the clearance of Aβ and stops the blood flow from the capillary unit, resulting in accumulation of metabolic waste products,

changes in the pH, and electrolyte imbalance. These chemical changes lead to deposition of amyloid in the vessel wall and accelerate accumulation of the intraneuronal tangles. At the end stage the profound neuroinflammatory response and a collapse of the capillary unit occur, accompanied by a loss of axonal-dendritic synapses and neurons[14] (see Figure 2).

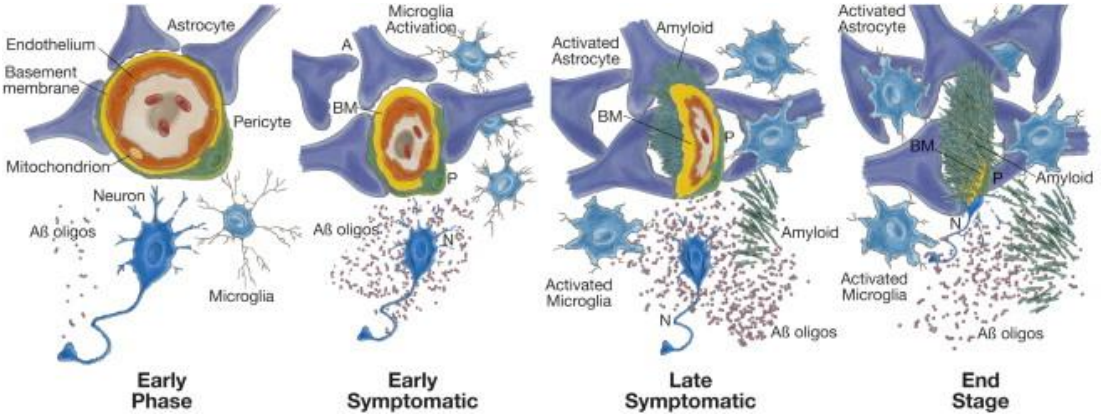

Figure 6: Scheme representing the neurovascular unit and its participation and modification in AD. In the early phase the BBB starts loosing membrane functions concerning Aβ clearance, and the endothelium starts secreting proinflammatory cytokines and suppressors of the cerebral blood flow. This leads to advanced synaptic dysfunction and microglia activation. In the late symptomatic phase, the capillaries are deformed, containing a degenerated endothelial barrier. Altogether this results in a severely reduced Aβ clearance, thus again facilitating amyloid formation on the outer side of the capillary membrane. Simultaneously, the numbers of activated astrocytes, microglia, and NFTs increase. At the end stage, the capillary unit collapses, and deteriorating neurons and synapses are buried by amyloid deposits. A = astrocyte, BM = basal membrane, P = pericyte, N = neuron. Figure and information was taken from[14].

Another event concerning the neurovascular unit in the broadest sense—the loss of AQP4 from end-feet membranes—has been observed in a model of AD and in other disorders such as epilepsy or traumatic brain injury[45]. Aquaporins are a family of integral channel proteins that facilitate the bidirectional water transport across the cell membrane. The highly polarized distribution of AQP4 in reactive astrocytes is impaired in different diseases; this might result from either reduced AQP4 in end-feet or from increased AQP4 expression in parenchymal membranes[45]. Iliff et al. showed in 2012 that the water channel AQP4 might play a crucial role in Aβ clearance, and consequentially in AD[46]. However, the connection of AQP4 and AD needs to be investigated.

1.2.3.3 *Vascular Basal Membranes*

Physiology of Vascular Basal Membranes

Basal membranes (BMs) are present in every human tissue, in detail every epithelium and endothelium is connected with BMs[47]. BMs are structures built by different extracellular matrix structural proteins, such as collagen and laminin[14]. Collagen type IV, one of the 28 currently known types[48,49], is the most widely expressed non-fibrillar collagen and the most abundant protein in BMs[47,49]. Cerebrovascular BMs are important for the development and health of blood vessels, formation and support of the BBB, and transfer of peripheral cells into the brain[33].

Histopathological Features of Vascular Basal Membranes in AD – Changes of Collagen Type IV

Duplication and splitting of the cerebrovascular BM occurs frequently in the brain of aged individuals, but is especially common in human AD and in animal models of AD[33]. Another event in AD is the accumulation of extracellular matrix components, especially collagen IV in the vascular basal lamina[19,32], thus leading to the thickening of the capillary BM[15].

1.3 Mouse Models of Alzheimer´s Disease

The limited knowledge of Aβ pathology and the lack of therapeutics against AD have led to the production of a wide range of transgenic (tg) animal models that overexpress genes that are associated with hereditary (familial) forms of AD. These animal models provide a useful tool to investigate different pathways of the disease and to develop and test new strategies for AD treatment. The ideal animal model should help to find the onset and to understand the progression of the disease on the one hand and, should be a valuable tool for developing and testing clinically useful drugs on the other hand[50,51].

Due to the disease prevalence and the bad prognosis many animal models for dementia have been created. Therefore different organisms such as mice, rats, fish, flies, and worms were modified[52].

Tg remodeling of Drosophila and *Caenorhaditis elegans* enable a high degree of experimental control and offer benefits because of their short life span. Contrariwise,

they are in many ways unlike mammals. So with respect to creating treatment options they have less impact than models in mammalian systems. In general, the most used species among the vertebras are mice. They are relatively inexpensive, they have a relative short life span and the technique for developing tg mice is well known. Additionally some tg rodent models have been generated[52]. Nevertheless, at present the ideal animal model which mimics cognitive, behavioral, biochemical and histopathological abnormalities of AD is still missing[52,53].

In 2001 Rockenstein et al. developed a single-tg mouse model that expresses the human APP gene, containing the London (V717I) and Swedish (K670M/N671L) mutations under the regulatory control of the murine (m)Thy-1 promoter. The mice express high levels of APP_{SL}, leading to an age-depending increase of Aβ40 and Aβ42 deposition. Animals show early plaque formation starting at an age of three months, that further progresses over time[54]. Age-dependent histopathological events are in line with behavioral deficits[55]. The occurrence of neuroinflammation in the brain has additionally been described[56].

Within this master thesis the above-mentioned tg mouse model is referred to as "APP_{SL}". These mice serve as a valuable tool in drug testing for the customers of QPS Austria. The model is also useful for basic research and for investigating histopathological features using new readouts, such as the current master project on cerebrovascular abnormalities of AD. Human brain samples were investigated in parallel experiments using identical or very similar reagents and methods. The goal of this parallel approach was to detect and quantify whether similar histopathological processes occur in human AD and in the APP_{SL} mouse model. Ultimately, such comparative studies aim at establishing data-based sets of rules for deciding which model is most useful for investigating a specific scientific question.

2 MATERIALS AND METHODS

For the present experiments human cortical and hippocampal brain samples and entire brains of transgenic (tg) APP_{SL} mice were analyzed by immunohistochemistry (IHC).

2.1 Sample Preparation of APP_{SL} and nTg Mice

A total of 18 female APP_{SL} mice and 18 female non-transgenic controls (nTg) were included. Tg mice of three different age groups (6, 9 and 12 months) were compared to age- and sex-matched littermates. Accordingly, mice were allocated to one of six experimental groups (n = 6 per group). Table 1 shows genotype and age on the day of sacrifice, the individual registration number (IRN), and the code numbers ("Histo-ID") assigned for blinding of the histological samples of APP_{SL} mice and their nTg littermates.

2.1.1 Sacarifice and Tissue Sampling

Mice were euthanized by inhalation of an overdose of an isofluorane based air mix (Isoba®). After blood sampling mice were transcardially perfused with 0.9 % saline and thereafter the brain of each mouse was sampled and hemisected. The left hemisphere was processed for biochemical investigations, the right was fixed in freshly prepared 4 % paraformaldehyde in 0.1 M phosphate buffer (pH 7.4) for one to two hours at room temperature, cryo-protected with 15 % sucrose/phosphate buffered saline (PBS) solution over night at 4 °C, shock-frozen in liquid dry ice cooled isopentane and stored in the corresponding labeled vial at -80 ± 5 °C in an ultra deep freezer.

2.1.2 Sectioning

The right brain hemispheres were systematically sectioned. Therefore the hemispheres were embedded to a tissue freezing medium (Leica) and sagitally cut on a cryotome (CM 3050 S, Leica). Ten µm thick sections were produced from in total 12 different mediolateral levels according to the morphology atlas "The Mouse

Brain in Stereotaxic Coordinates" from Paxinos and Franklin (2nd edition)[57] (see Figure 7).

Table 1: List of APP_{SL} and nTg mice used within the study. The table shows the genotype, the age at sacrifice, the IRN and the corresponding Histo-ID.

Genotype	Age	IRN	Histo-ID
APP_{SL}	6 months	99	335/11
		103	336/11
		149	669/11
		223	909/11
		465	2098/11
		775	1891/12
	9 months	109	1081/11
		125	1082/11
		301	2025/11
		309	2026/11
		311	2027/11
		361	2238/11
	12 months	29	1653/11
		61	1827/11
		189	2097/11
		283	2241/11
		285	2242/11
		203	2445/11
nTg	6 months	83	338/11
		93	340/11
		225	916/11
		375	1657/11
		761	1893/12
		773	1894/12
	9 months	115	1084/11
		119	1085/11
		121	1086/11
		179	1377/11
		185	1378/11
		193	1379/11
	12 months	41	1659/11
		81	1834/11
		163	2099/11
		165	2100/11
		167	2101/11
		171	2244/11

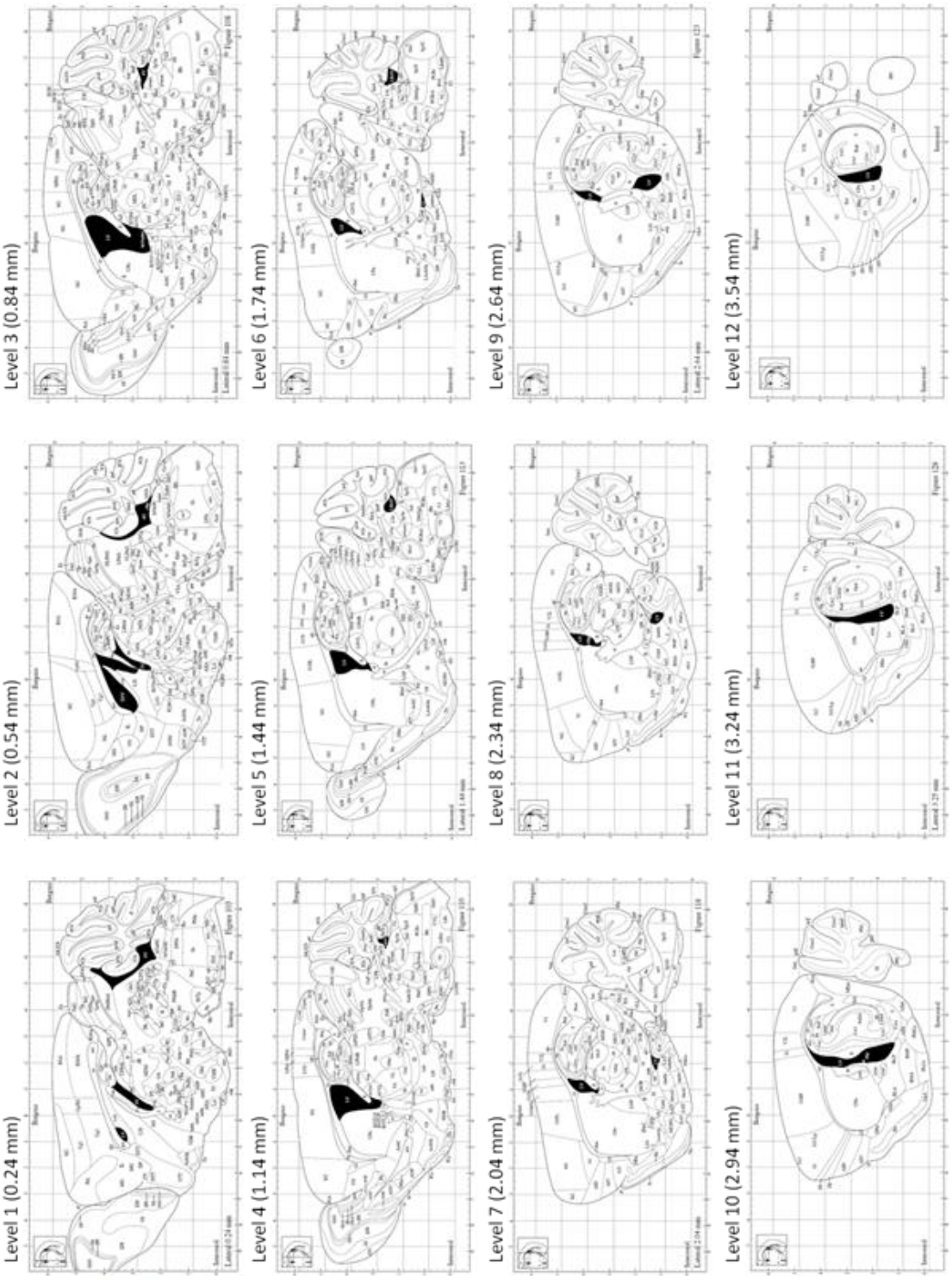

Figure 7: Mediolateral levels in sagittal cryosectioning. In total seven or 10 sections from 12 mediolateral levels were produced per right hemisphere for histological investigations. Illustrations were taken from[57].

The starting coordinate of the first level was approximately 0.24 mm lateral from midline. From there sectioning continued uniformly and systematically. Per level seven or in some cases ten consecutive sections were retained and 23 or 20

sections were discarded, respectively. Each section was collected on a uniquely labeled and coated glass slide (Polysine® slides, Gerhard Menzel GmbH). This labeling includes information to the section thickness, the Histo-ID, the sectioning level and the section number. The sections were stored in a box at -20 ± 5 °C in a deep freezer until used for histological investigations.

2.2 Human AD and Control Samples

Formalin fixed paraffin sections of different human brain regions from subjects that suffered from AD, as well as of control subjects without any AD-related pathological features, were provided by the brain bank from the University of Newcastle. Subjects had been staged according to Braak, and the samples were assigned to one of three “Braak groups” (I/II, III/IV and V/VI) or to the control group by pathologists of the University of Newcastle. Six µm thick sections of five different brain regions – frontal cortex (CTX), cingulate CTX, occipital CTX, temporal CTX and hippocampus (HC) (for an overview see Figure 8) – of five subjects per group were investigated. To perform a randomized study, just the individual registration number and the according Braak stages were known (see Table 2), whereas further sample information is by now blinded and will stay blinded as long as analyses are proceeding.

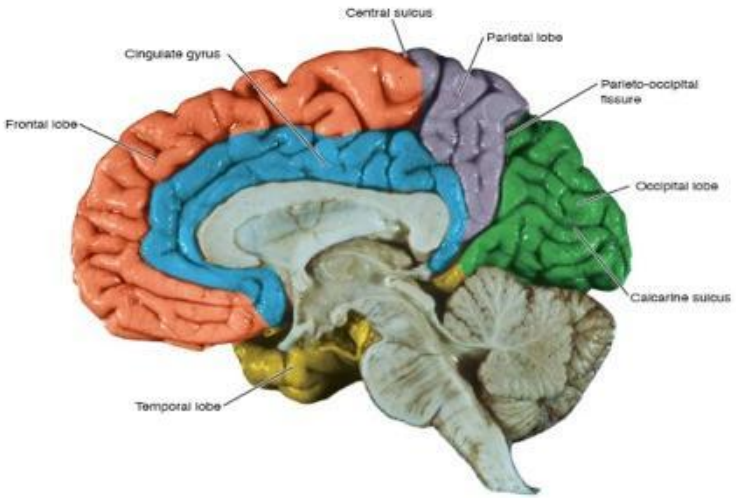

Figure 8: Image represents a midsagittal section of the human brain highlighting different cortical regions. Within this study, sections of the frontal (red), cingulate (blue), occipital (green) and temporal (yellow) CTX were investigated. Systematic blocks were prepared according to the standard protocol of the University of Newcastle, embedded and sectioned. Image was taken from[58].

Table 2: List of human samples used within this study. The table shows the four experimental groups and the five associated samples.

Braak Stage	IRN	Braak Stage	IRN
Control	729/10	III/IV (Medium)	65/09
	272/11		104/09
	118/09		719/10
	891/11		1067/10
	87/05		9991/11
I/II (Low)	1016/11	V/VI (High)	02/09
	43/09		561/11
	150/10		102/08
	359/10		100/09
	80/11		205/11

2.3 Immunohistochemistry

Samples were investigated by indirect immunofluorescence. Two different multichannel labeling experiments were performed. 1) Immunofluorescent labeling with specific antibodies against smooth muscle actin (SMA), human amyloid (clone 6E10, residues 1-16) and collagen IV as well as a counterstaining of cell nuclei with DAPI was done. 2) Labeling of Aβ40/42 (clone MOAB-2, residues 1-4), collagen IV and AQP4 was performed. The binding of primary antibodies was visualized using highly cross-adsorbed secondary antibodies conjugated to different DyLight fluorophors. In order to assess any unspecific binding of secondary antibodies an operational negative control was produced within each experiment. Such sections were treated exactly as the other sections of the experiments, except that the primary antibodies were omitted. Details to antibodies are presented on the following pages in Table 3 and Table 4. Detailed information on buffers and solutions is provided in Table 5.

2.3.1 Immunolabeling of SMA, 6E10, Collagen IV and DAPI (Experiment I)

After some pretests, which were necessary to set the ideal incubation conditions, systematically four sections of four different levels (levels 2, 4, 6 and 8) per animal and five sections per human (one of each region) were labeled with specific antibodies against SMA, human amyloid (clone 6E10, residues 1-16) and collagen IV. Cell nuclei were stained using a DAPI counterstaining. Therefore a total of 144

mouse cryo sections and 100 human paraffin sections were incubated as described below.

Table 3: Primary antibodies used for IHC.

Antibody Name	Host	Clone	Concentration [mg/ml]	Dilution	Company	Item Number
Alpha smooth muscle actin	rabbit	polyclonal	0.2	1/1000	Abcam	ab5694
AQP4 (C-19)	goat	polyclonal	0.2	1/700 (mouse sections); 1/250 (human sections)	Santa Cruz	sc-9888
Beta Amyloid [residues 1-16]	mouse	6E10	1	1/1000	Covance	SIG-39329
Beta Amyloid peptide (40/42)	mouse	MOAB-2	1	1/1000	Biosensis	M-1586-100
Collagen IV	rabbit	polyclonal	1	1/700	Abcam	ab6586

Table 4: Secondary antibodies used for IHC.

Antibody Name	Conjugation	Host	Species Reactivity	Concentration [mg/ml]	Company	Item Number
Donkey Anti-Rabbit IgG (H+L)	DyLight® 488	donkey	rabbit	0.5	Abcam	ab96919
Donkey Anti-Goat IgG (H+L)	DyLight® 650	donkey	goat	0.5	Abcam	ab96938
Donkey Anti-Mouse IgG (H+L)	DyLight® 650	donkey	mouse	0.5	Abcam	ab98797
Donkey Anti-Mouse IgG (H+L)	DyLight® 488	donkey	mouse	0.5	Abcam	ab98794
Donkey Anti-Rabbit IgG (H+L)	Alexa Fluor® 555	donkey	rabbit	2	Abcam	ab150066
Dilution of all antibodies was 1/500						

Table 5: Buffers and solutions used for IHC.

Buffer/Solution	Composition/Preparation	Compound	Company	Item Number
Antibody Diluent	-	Antibody Diluent	Dako	S3022
Citrate buffer saline (CBS)	Citrate buffer (10X) diluted 1:10 with aqua bidest.	Citrate buffer (10X)	Thermo Scientific	AP-9003
		Aqua bidest.	Fresenius Kabi	B230673
DAPI – working solution	1,25 µl DAPI stock solution diluted in 50 µl methanol	DAPI (4',6-diamidino-2-phenylindole)	AppliChem GmbH	1001.0025
		Methanol	Merck	1.06009.1000
10 % Donkey serum	10 µl Normal donkey serum + 90 µl phosphate buffered saline (PBS)	Normal donkey serum	Jackson Immuno Research	017-000-121
		PBS: see "phosphate buffered saline" in this table		
Ethanol absolute	-	Ethanol absolute	Merck	1.00983.1000
M.O.M. Blocking reagent (Experiment I)	1 gt M.O.M. Mouse IgG Blocking Reagent + 1.25 ml 1 % Triton X-100/PBS	M.O.M. Mouse IgG Blocking Reagent	Vector Laboratories, Inc (from M.O.M. Kit Basic)	BMK-2202
		PBS: see "phosphate buffered saline" in this table		
		Triton X-100	AppliChem GmbH	A1388,0500
M.O.M. Blocking reagent (Experiment II)	1 gt M.O.M. Mouse IgG Blocking Reagent + 1.25 ml PBS	M.O.M. Mouse IgG Blocking Reagent	Vector Laboratories, Inc (from M.O.M. Kit Basic)	BMK-2202
		PBS: see "phosphate buffered saline" in this table		
M.O.M. Diluent solution	80 µl M.O.M. Protein Concentrate + 1 ml PBS	M.O.M. Protein Concentrate (from M.O.M. Kit Basic)	Vector Laboratories, Inc	BMK-2202
		PBS: see "phosphate buffered saline" in this table		
Moviol – working solution	20 g Moviol + 74 ml phosphate buffered saline → stirring at least 16 hours → +46 ml Glycerol → stirring at least 16 hours → centrifuged for 15 minutes at 12000 g	Moviol®	Sigma-Aldrich®	81381
		PBS: see "phosphate buffered saline" in this table		
		Glycerol	Merck	1.04094.1000
Phosphate buffered saline (PBS)	<u>20 x:</u> 4 g potassium chloride + 4 g potassium dihydrogen phosphate + 160 g sodium chloride + 29 g di-sodium hydrogen phosphate dihydrate → volumetric flask has been filled up to 1 liter with aqua bidest. and adjusted to pH 7,05 <u>1 x:</u> 20x concentrate diluted 1:20 with aqua bidest.	Potassium chloride	Sigma-Aldrich®	P5405-250G
		Potassium dihydrogen phosphate	Merck	1.04877.1000
		Sodium chloride	Roth	P029.3
		Di-sodium hydrogen phosphate dehydrate	Merck	1.06580.1000
		Aqua bidest.	Fresenius Kabi	B230673
Sodium borohydride solution	250 mg sodium borohydride + 250 ml cooled PBS	Sodium borohydride	Sigma-Aldrich®	213462
		PBS: see "phosphate buffered saline" in this table		
1 % Triton X-100/PBS	1 ml Triton X-100 ad 100 ml aqua bidest.	Triton X-100	AppliChem GmbH	A1388,0500
		Aqua bidest.	Fresenius Kabi	B230673

2.3.1.1 *Labeling Protocol*

In order to improve the adhesion of the cryosections on slides, sections were air-dried for one hour. The paraffin sections, in contrast, were deparaffinized in Tissue Clear® for ten minutes and Tissue Clear®/100 % ethanol for another five minutes, washed in 100 % ethanol for five minutes and then rehydrated with decreasing alcohol concentrations (96 % ethanol for two minutes, 70 % ethanol for two minutes and 50 % ethanol for two minutes). Thereafter the sections were washed two times for five minutes with PBS (i.e. standard washing step).

Afterwards slices were incubated with 10 % CBS in a steamer. Slides were allowed to heat-up to 95°C, were then incubated for 15 minutes, and cooled down to room temperature for another 15 minutes outside of the steamer. This “antigen retrieval” step opens cross-links due to the fixation with 4 % paraformaldehyde and formalin. At the same time, it leads to a heat fixation, in combination resulting in better accessibility of epitopes due to the denaturation of proteins. At the end of this procedure the sections were washed.

To reduce autofluorescence (AF) and saturate free aldehyde groups within the fixed tissue, the sections were treated with cold sodium borohydride solution for four minutes and then washed.

Next, the sections were encircled with a hydrophobic pen and then the tissue was covered with blocking solution in order to reduce unspecific bindings of primary antibodies. The mouse samples were incubated with M.O.M. Blocking Reagent, whereas the human samples were treated with 10 % donkey serum in 1 % TritonX-100/PBS for one hour in a damp chamber.

After another washing step the sections were labeled with the anti-smooth muscle actin antibody (mouse sections: dilution 1/1000 in M.O.M.-Diluent; human sections: dilution 1/1000 in Antibody-Diluent) and the anti-human amyloid (clone 6E10, residues 1-16) antibody (mouse sections: dilution 1:1000 in M.O.M.-Diluent; human sections: dilution 1/1000 in Antibody-Diluent) for one hour in a damp chamber and after this washed.

To avoid quenching of the fluorescence of the secondary antibodies the slides were protected from light during all subsequent procedures. The sections were incubated with a donkey anti-rabbit (DyLight® 488) antibody (mouse sections: dilution 1/500 in

M.O.M.-Diluent; human sections: dilution 1/500 in Antibody-Diluent) and a donkey anti-mouse (DyLight® 650) antibody (mouse sections: dilution 1/500 in M.O.M.-Diluent; human sections: dilution 1/500 in Antibody-Diluent) for one hour in a damp chamber and washed again.

After this, sections were blocked with 10 % donkey serum/PBS for one hour and washed.

Thereafter the slides were labeled with an anti-collagen IV antibody (mouse sections: dilution 1/700 in M.O.M.-Diluent; human sections: dilution 1/700 in Antibody-Diluent) for one hour in a damp chamber and then washed with PBS.

Afterwards they were incubated with a donkey anti-mouse (Alexa Fluor® 555) antibody (mouse sections: dilution 1/500 in M.O.M.-Diluent; human sections: dilution 1/500 in Antibody-Diluent) for one hour in a damp chamber and then washed.

Cell nuclei were then visualized by counterstaining the sections with DAPI working solution for 15 minutes. The slides were differentiated two times for three minutes each with 80 % ethanol, were washed five minutes in PBS, followed by one minute in aqua bidest..

Finally, the sections were covered with moviol and coverslips.

2.3.2 Immunolabeling of Aβ40/42, Collagen IV and AQP4 (Experiment II)

After some pretests, a systematic random set of five sections from five different mediolateral levels (levels 2, 4, 6, 8 and 10) per animal and one section per region per human brain were labeled with antibodies against Aβ40/42 (clone MOAB-2, residues 1-4), collagen IV and AQP4. A total of 180 mouse cryo sections and 100 human paraffin sections were incubated as described in the following paragraph.

2.3.2.1 *Labeling Protocol*

In order to improve the adhesion of the cryosections on slides, sections were air-dried for one hour. The paraffin sections, in contrast, were deparaffinized in Tissue Clear® for ten minutes and Tissue Clear®/100 % ethanol for another five minutes, washed in 100 % ethanol for five minutes and then rehydrated with decreasing alcohol concentrations (96 % ethanol for two minutes, 70 % ethanol for two minutes

and 50 % ethanol for two minutes). Thereafter the sections were washed two times for five minutes with PBS (i.e. standard washing step).

Afterwards slices were incubated with 10 % CBS in a steamer. Slides were allowed to heat-up to 95°C, were then incubated for 15 minutes, and cooled down to room temperature for another 15 minutes outside of the steamer. This “antigen retrieval” step opens cross-links due to the fixation with 4 % paraformaldehyde and formalin. At the same time, it leads to a heat fixation, in combination resulting in better accessibility of epitopes due to the denaturation of proteins. At the end of this procedure the sections were washed.

To reduce AF and saturate free aldehyde groups within the fixed tissue, the sections were treated with cold sodium borohydride solution for four minutes and then washed.

To facilitate the accessibility from the antibodies to their epitopes a permeabilization step with a 1 % Triton X-100/PBS solution for ten minutes was performed.

Next, the sections were encircled with a hydrophobic pen and then the tissue was covered with blocking solution in order to reduce unspecific bindings of primary antibodies. The mouse samples were incubated with M.O.M. Blocking Reagent, whereas the human samples were treated with 10 % donkey serum for one hour in a damp chamber.

After three washing steps and encircling of the tissue with a hydrophobic pen, the unspecific bindings were blocked with either M.O.M. Blocking Reagent (mouse sections) or 10 % donkey serum (human sections) for one hour in a damp chamber.

After another two washing steps the sections were labeled with all three primary antibodies – Aβ40/42 (mouse sections: dilution 1/1000 in M.O.M.-Diluent; human sections: dilution 1/1000 in Antibody-Diluent), collagen IV (mouse sections: dilution 1/700 in M.O.M.-Diluent; human sections: dilution 1/700 in Antibody-Diluent) and AQP4 (mouse sections: dilution 1/700 in M.O.M. Diluent; human sections: dilution 1/700 in Antibody-Diluent) for one hour in a damp chamber and after this washed.

To avoid quenching of the fluorescence of the secondary antibodies the slides were protected from light during all subsequent procedures. The sections were incubated with a donkey anti-mouse (DyLight® 488) antibody, a donkey anti-rabbit (Alexa Fluor® 555) and a donkey anti-goat (DyLight® 650). Every secondary antibody has

been diluted 1/500 in either M.O.M. Diluent (mouse sections) or Antibody-Diluent (human sections). Incubation occurred for one hour in a damp chamber and washed again.

Finally, the sections were washed in aqua bidest. for five minutes and covered with moviol and coverslips.

2.4 Imaging

2.4.1 Imaging of Mouse Sections

Mosaic images including the whole cerebral CTX and HC of the stained sections from experiment I and II were recorded on a fully automated Zeiss AxioImager.Z1 microscope using a high aperture lens and the AxioVision (version 4.8) software driven AxioCam MRm digital camera (10x lens, numeric aperture 0.45, 1x optocoupler). Excitation was achieved by LED illumination (Colibri, Zeiss Ag). Further imaging parameters are provided in Table 6.

Table 6: Imaging parameters of mouse sections of experiment I and II. AF = autofluorescence.

Experiment	Antigen	Exposure time [ms]
Experiment I	green AF	95
	human Aβ	400
	collagen IV	50
	DAPI	11
Experiment II	AQP4	300
	collagen IV	100
	Aβ40/42	60

2.4.2 Imaging of Human Sections

On each stained section of experiment I two mosaic images with a size of approximately three mm^2 each including white and grey matter were captured. A Zeiss AxioImager.Z1 microscope using a high aperture lens and an AxioVision 4.8 software driven AxioCam MRm digital camera (20x lens, numeric aperture 0.8, 1x optocoupler) served for recording. An example of scale and positions of recorded images is shown in Figure 9. The sections were imaged with a z-stack height of nine µm and captured stacks were collapsed to 2D in AxioVision and converted for

subsequent image analysis in Image-Pro Plus (version 6.2). Excitation was achieved by LED illumination (Colibri, Zeiss Ag). For further imaging parameters see Table 7.

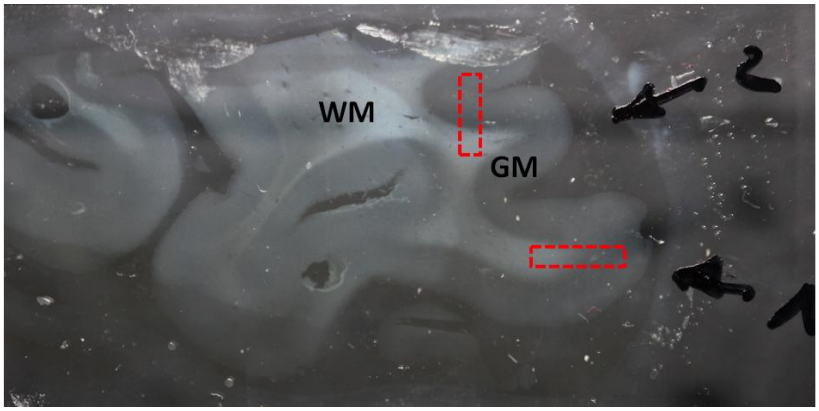

Figure 9: Exemplary photograph of a frontal CTX section representing imaged areas. From each section two mosaic images were captured, which were marked on the cover slip with permanent marker as “1” and “2”. Red dashed rectangles indicate areas from which 20x tiles (each with approximately 3 mm²) were recorded including white and grey matter. Two sections per subject and brain region were processed, resulting in an investigated section area of approximately 2 x 3 mm² = 6 mm² per region. GM = gray matter, WM = white matter. Image was taken from a yet unpublished master´s thesis of Dominik Schmied.

Table 7: Imaging parameters of green AF + human amyloid + collagen IV labeling on human sections. AF = autofluorescence.

Antigen	Exposure time [ms]
green AF	80
human amyloid	277
collagen IV	100
DAPI	130

From experiment II two mosaic images were recorded on a Nikon Eclipse E400 microscope with a high aperture lens (20x lens, numerical aperture 0.5, 1x optocoupler), equipped with a Cool LED pE-300-W lamp and the Nikon DS-Qi1MC camera. The Nikon NIS-Elements AR software supported imaging. An example of the image scale and position of captured images is shown in Figure 9. The sections were imaged with a z-stack height of 30 µm and after capture, images collapsed to 2D in AxioVision and converted for subsequent image analysis in Image-Pro Plus (version 6.2). An example of imaged position is shown in Figure 9. Further imaging parameters see Table 8.

Table 8: Imaging parameters of green AF + collagen IV + AQP4 - labeling of human sections. AF = autofluorescence.

Antigen	Exposure time [ms]	Gain
green AF	60	9.60
collagen IV	60	16.0
AQP4	600	19.2

2.5 Evaluation

Image-Pro Plus software (version 6.2) was used to generate a manual delineation of the CTX and the HC for macro-based image analysis of both experiments. This area of interest (AOI) serves 1) to evaluate the region size of the individual brain areas and 2) to normalize the measured variables to the individual region size per section. An example of the AOIs defining the cerebral CTX and HC in mouse brain sections is shown in Figure 10.

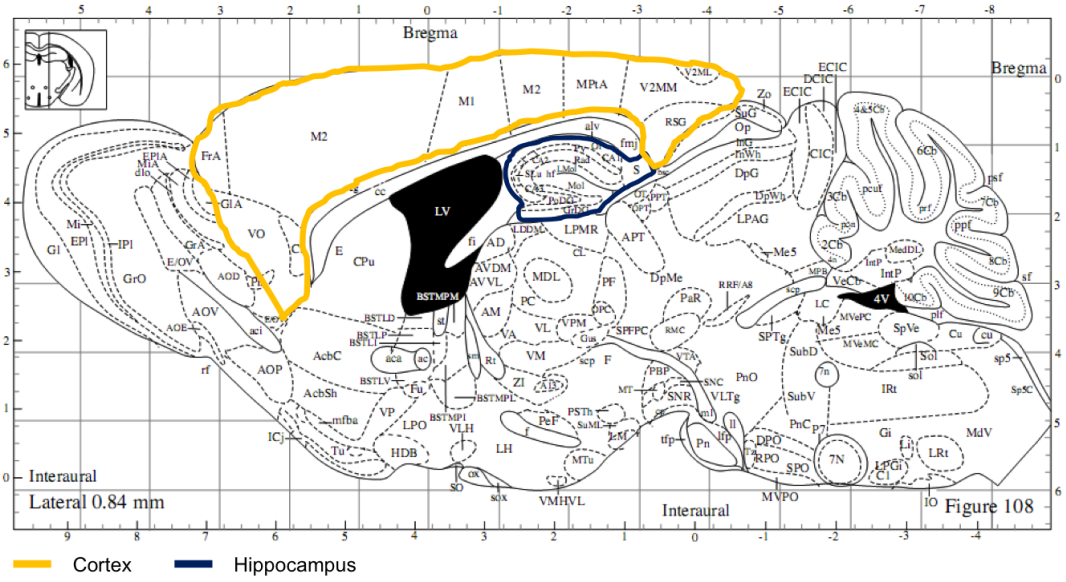

Figure 10: Manual delineation of measured brain regions. The orange line encircles the cerebral CTX and the blue one the HC of mouse sections. Note that white matter of the HC such as the fimbria (fi) was excluded and the subiculum (S) was included in delineation and evaluation. Image was taken from[57] and adapted.

From the human sections, the whole recorded image was defined as one AOI of the particular region for both experimental setups.

The individual quantitative evaluations were performed using the Image-Pro Plus software (version 6.2). Measurements were macro-based, automated and rater-independent.

The evaluations of the 1st experiment include the quantitative analysis of:

- total region size of the different mouse brain areas
- normalized sum pixel intensity of fluorescent signal for 6E10,
- normalized sum pixel intensity, object density and mean object size of collagen IV fluorescent signal,
- and normalized sum pixel intensity of fluorescent signal for CAA.

The evaluations of the 2nd experiment contain the quantitative analysis of:

- normalized sum pixel intensity of fluorescent signal for Aβ40/42 only in mouse tissue
- and normalized sum pixel intensity of fluorescent signal for total AQP4, vascular related and parenchymal AQP4.

IHC measurements except region size determinations were threshold based, therefore objects above a certain intensity and above a size of seven μm^2 were automatically detected by Image-Pro Plus software (version 6.2). The threshold ensures that only objects with an intensity higher and a size larger than the specified limits are counted. Measured variables were normalized to the size of the distinct AOI areas. Special features of distinct measurements are described in the following sub-chapters. Details of the used measurement parameters for all evaluations are given in Table 9.

2.5.1 Evaluation of 6E10

In order to optimize the measurement of total 6E10 intensity first a lowpass-filtered (size 500, passes 1) image was subtracted from the 6E10 channel. Thereafter the 6E10 immunoreactivity (IR) of mouse section was measured with an adaptive threshold, which is defined as mean signal within the AOI plus a factor times the standard deviation of the signal within the AOI. 6E10 IR of human tissue in contrast was measured after subtracting the green AF and above a constant threshold to avoid measurement of unspecific signal emitted by autofluorescent particles. The outlines of measurements on low pass corrected images were reloaded onto original images to obtain original signal values. Based on this measurement the sum pixel intensity of the original images was quantified. Examples of the procedures are shown in Figure 11 (mouse) and Figure 12 (human).

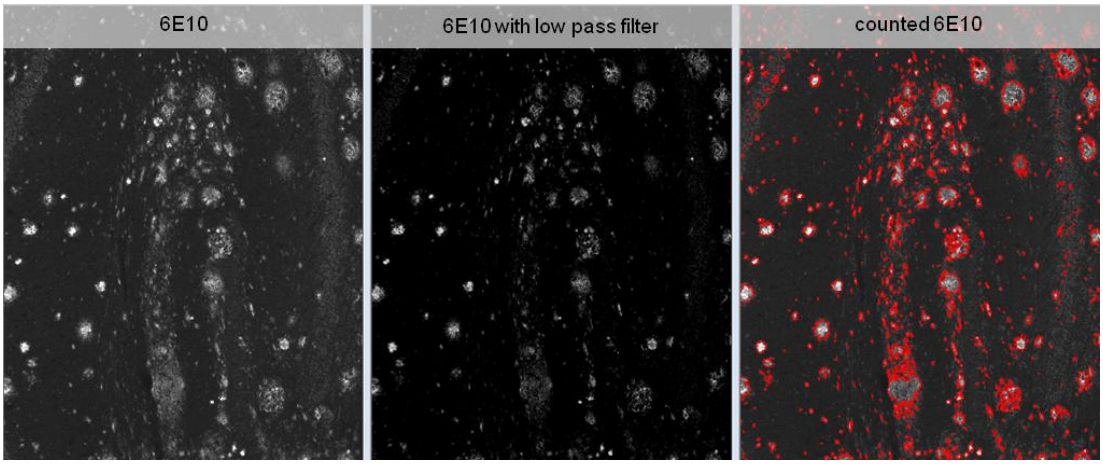

Figure 11: Example of the 6E10 measurement process in the HC of a 12 months old APP_{SL} mouse (Histo-ID 2445/12, level 8). The left image shows the original 6E10 immunolabeling. The mid one represents the low pass filter corrected picture and on the right side, the final measurement of 6E10 positive objects (red encircled) is visualized by reloading the measurement outline onto the original image. The latter was automatically done to obtain original signal values.

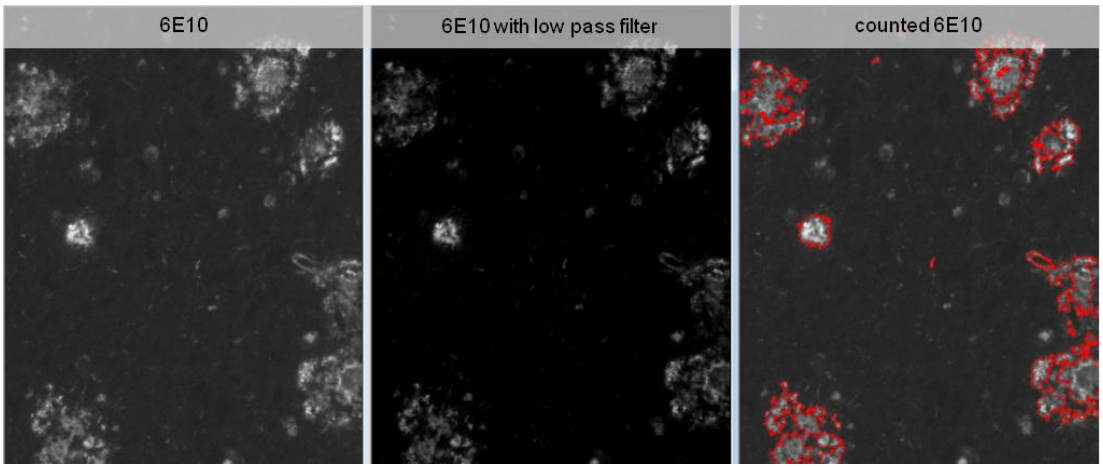

Figure 12: Illustration of 6E10 measurement in human HC at Braak stage V/VI (IRN 02/09). The left image shows the original 6E10 immunolabeling. The mid one represents the low pass filter corrected picture and on the right side, the final measurement of 6E10 positive objects (after subtracting the green AF (not shown)) (red encircled) is visualized by reloading the measurement outline onto the original image. The latter was automatically done to obtain original signal values.

2.5.2 Evaluation of Collagen IV

To obtain an optimal measurement of the collagen IV immunolabeling of mouse tissue, an edge plus filter (size 300, strength 3, iterations 1) was applied to increase signal/noise at the edges of vessels. Due to an automatic undo of the filter no reload on original images was required. Since the antibody shows higher affinity to human collagen IV, no correction option was used for the measurement of human tissue. To measure vessels as closed objects (size including the lumen), object detection utilized the “8-pixel connect” and “fill holes” options. Furthermore, positive objects

had to overcome a size restriction of 13 µm^2. In parallel masks of the distinct measurements were generated for the following evaluation of CAA. Examples of the particular measurements are shown in Figure 13 (mouse) and Figure 14 (human).

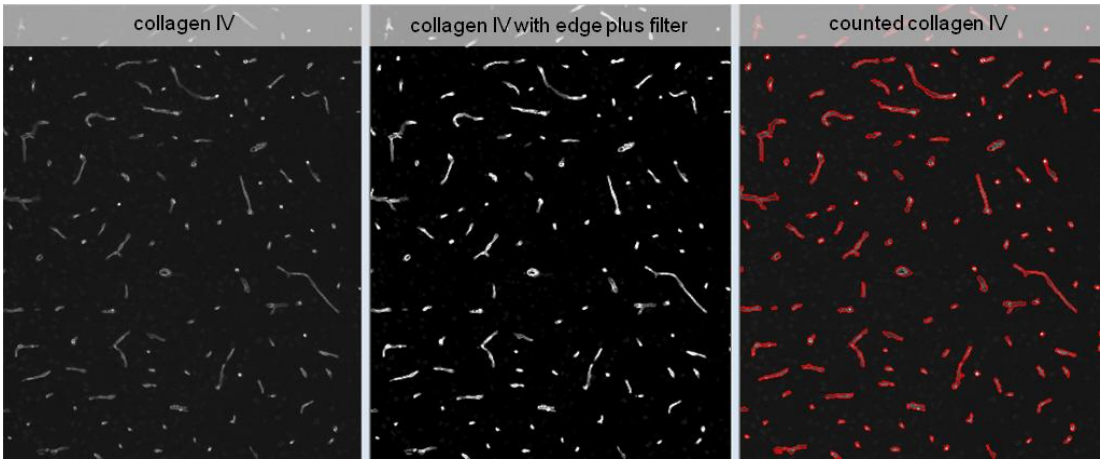

Figure 13: Images represent the measurement process of collagen IV immunolabeling in the CTX of a 12 months old APP$_{SL}$ mouse (Histo-ID 2445/12, level 8). From the original image (left), an adapted picture using the edge plus filter was generated to facilitate object detection (middle). The red encircled objects in the right image display counted collagen IV-positive objects.

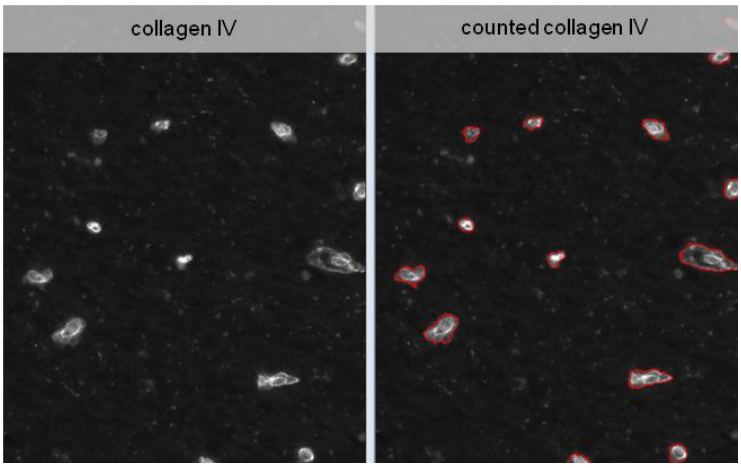

Figure 14: Example of collagen IV evaluation in the frontal CTX of a human section (Braak stage V/VI, IRN 02/09). The left image shows the original collagen IV staining. The red encircled objects in the right image display counted collagen IV-positive objects.

2.5.3 Evaluation of CAA

For the determination of CAA exclusively 6E10 labeling overlapping with collagen IV IR was counted. To achieve this, an inverted bilevel mask of the collagen IV count (described in chapter 2.5.2) was subtracted from the 6E10 channel. Further measurement of CAA of mouse sections was performed as the evaluation of total human amyloid (see chapter 2.5.1). Objects were measured above a fixed threshold of 90. Examples of the CAA determinations are given in Figure 15 (mouse) and Figure 16 (human).

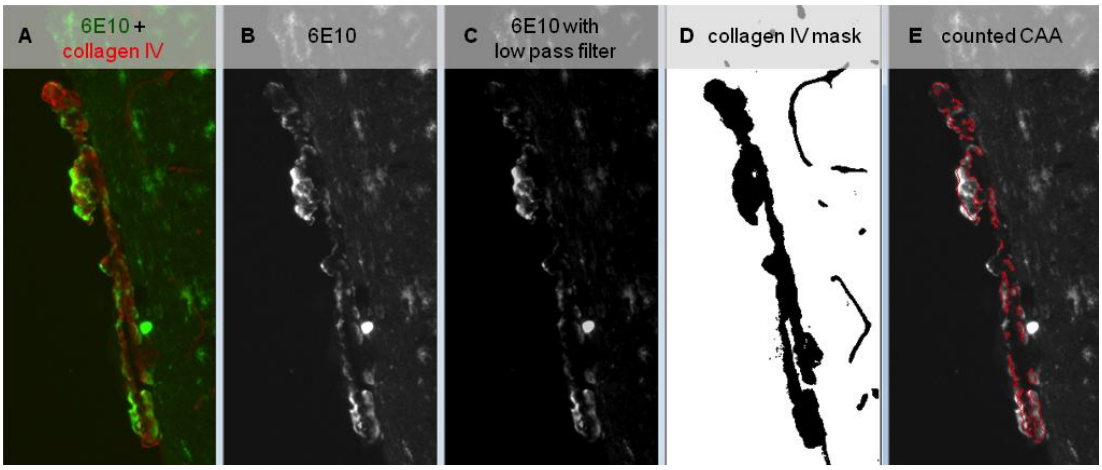

Figure 15: The images show an exemplary measurement process of CAA in the CTX of a 12 months old APP_{SL} mouse (Histo-ID: 2445/12, level 8). A shows the composite image of the 6E10 + collagen IV channels. B represents the single 6E10 labeling. C illustrates the modified human amyloid labeling with the low pass filter correction. D presents the inverted collagen IV mask. Finally, C shows the ultimate count of CAA (red encircled).

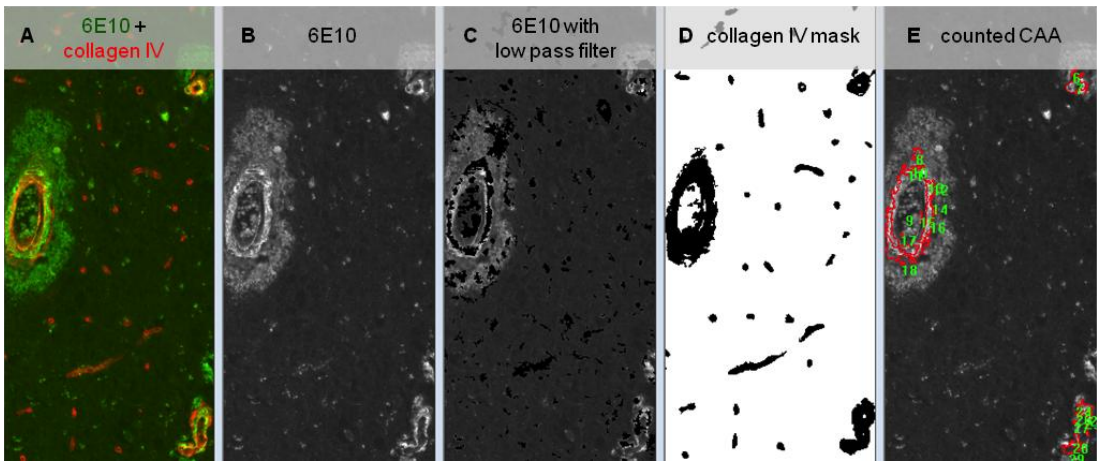

Figure 16: Example of CAA determination in the HC of a human brain section (Braak stage V/VI, IRN 02/09). A shows the composite image of the 6E10 + collagen IV channels. B represents the single 6E10 labeling. C illustrates the modified human amyloid labeling after subtracting the imaged green AF. D presents the inverted collagen IV mask. Finally, C shows the ultimate count of CAA (red encircled).

2.5.4 Evaluation of Aβ40/42 (clone MOAB-2)

To obtain an optimal measurement of Aβ40/42 immunolabeling of mouse tissue, an edge plus filter (size 500, strength 3, iterations 1) was applied to increase signal/noise at the edges of positive objects. Due to an automatic undo of the filter no reload on original images was required. An example of the measurement is presented in Figure 17.

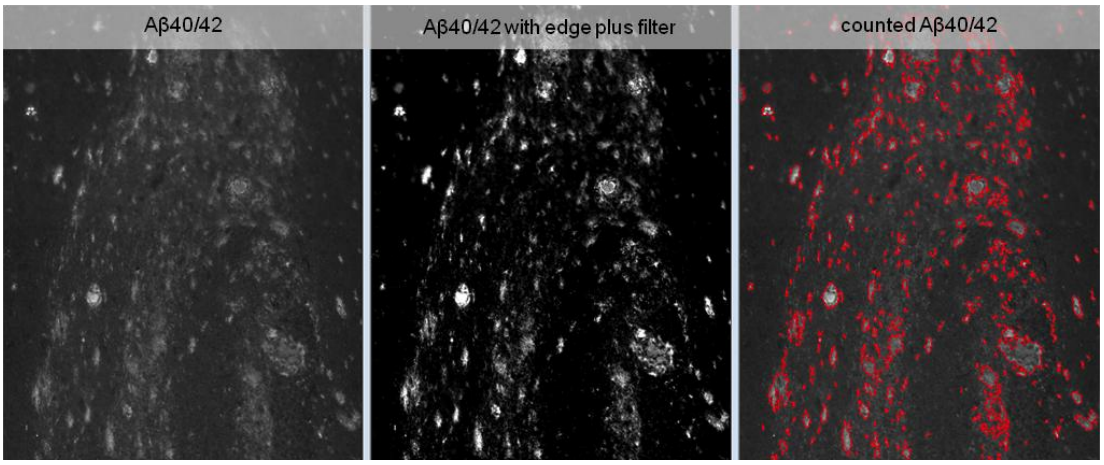

Figure 17: The images show an example of MOAB-2 determination process in the HC of a 12 months old APP_{SL} mouse (Histo-ID 2445/12, level 8). The left image shows the original MOAB-2 immunolabeling. The mid one represents the edge plus filter corrected picture and on the right side, the final measurement of MOAB-2 positive objects (red encircled) is visualized on the original image.

2.5.5 Evaluation of AQP4

To obtain an optimal measurement of AQP4 immunolabeling of mouse and human tissue, an edge plus filter (size 500, strength 3, iterations 1) was applied to increase signal/noise at the edges of positive objects. Due to an automatic undo of the filter, no reload on original images was required. Examples of AQP4 determinations are shown in Figure 18 (mouse) and Figure 19 (human).

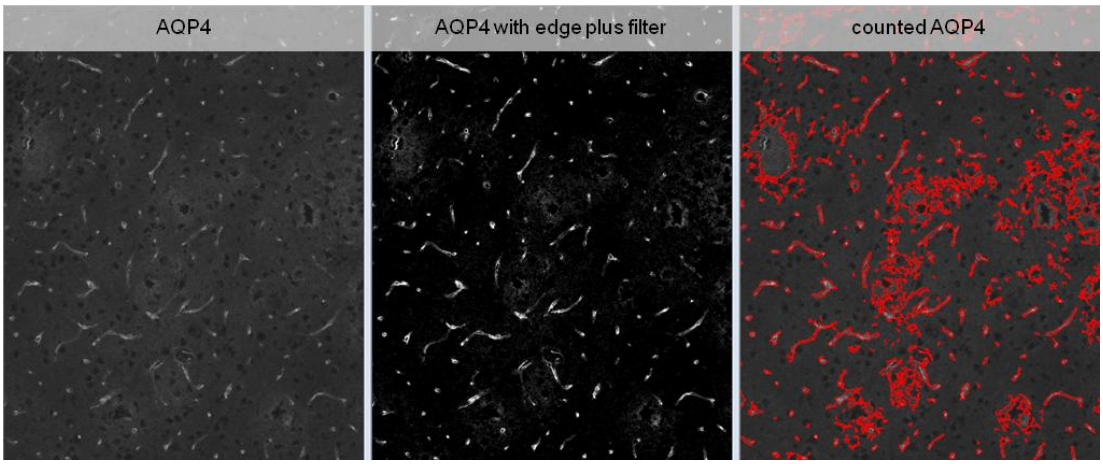

Figure 18: Example of the total AQP4 measurement process in the CTX of a 12 months old APP_{SL} mouse (Histo-ID 2445/12, level 8). From the original image (left), an adapted picture using the edge plus filter was generated to enable an optimal measurement (middle). The red encircled objects in the right image display counted AQP4-positive objects.

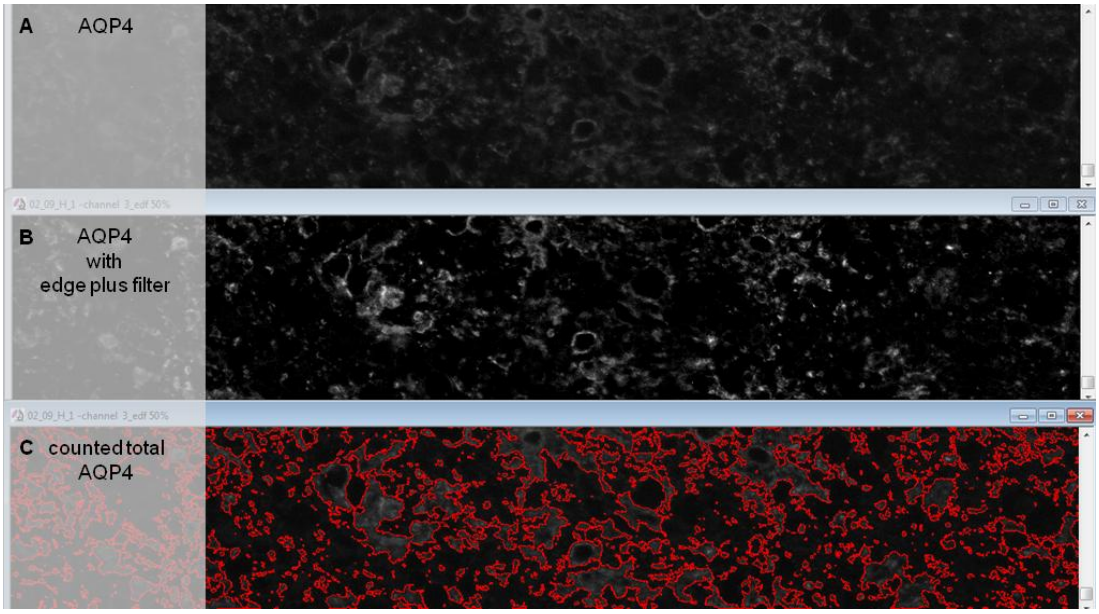

Figure 19: Example of total AQP4 measurement in the HC of a human section (Braak stage V/VI, IRN 02/09). The upper image shows the original AQP4 immunolabeling. The mid one represents the edge plus filter corrected picture and the lower picture shows the final measurement of AQP4-positive objects (red encircled) on the original image.

2.5.5.1 *Evaluation of Vascular Related and Parenchymal AQP4*

To determine collagen IV-overlapping AQP4 (= vascular related AQP4) of mouse and human sections, a bilevel mask of total collagen IV labeling was inverted and subtracted from the AQP4 image and then AQP4 was measured.

To evaluate the non-collagen IV-overlapping AQP4 (= parenchymal AQP4) of mouse and human sections, in contrast a bilevel mask of total collagen IV labeling was subtracted from the AQP4 image and then AQP4 was measured.

Measurement options were the same as the measurement of total AQP4 (see above). Examples of distinct measurements are presented in Figure 20 (vascular related AQP4, mouse), Figure 21 (vascular related AQP4, human), Figure 22 (parenchymal AQP4, mouse) and Figure 23 (parenchymal AQP4, human).

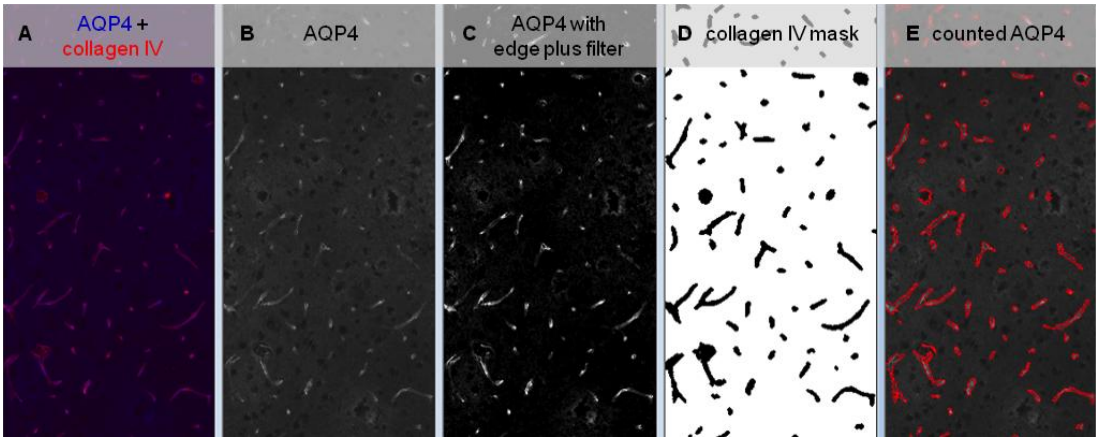

Figure 20: Images show an example of vascular related AQP4 measurement in the CTX of a 12 months old APP_{SL} mouse (2445/12, level 8). A shows the overlay of AQP4 and collagen IV, whereas B only displays the AQP4 immunolabeling. This image was modified with an edge plus filter (C) to reduce background labeling and to optimize unbiased measurement. Furthermore, the collagen IV mask (D) was inverted and used as pattern for the overlapping measurement. Finally counted objects are shown as red encircled items (E).

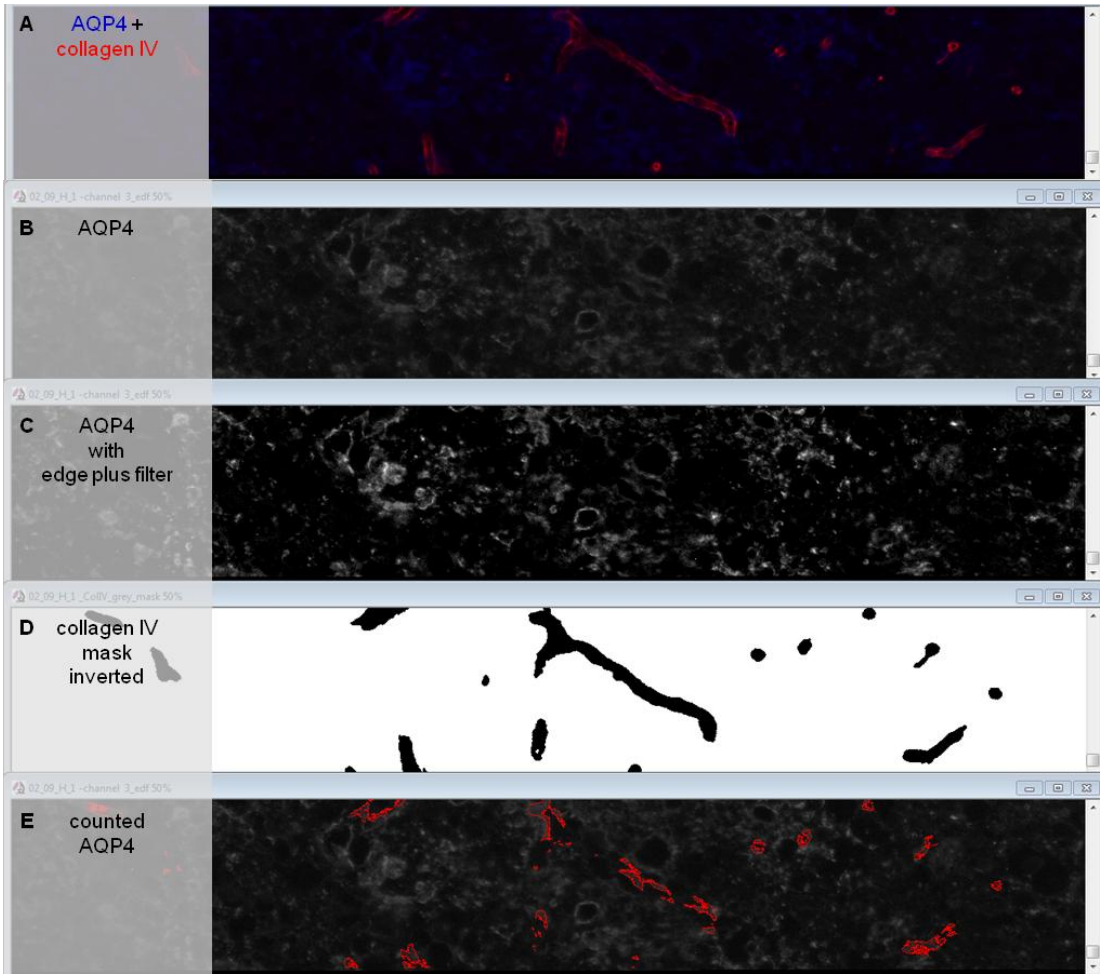

Figure 21: Images show an exemplary measurement process of vascular related AQP4 in the HC of a human section (Braak stage V/VI, IRN 02/09). A represents the composite image of the AQP4 and collagen IV immunolabeling, whereas B shows simply the AQP4 channel. C illustrates the AQP4 channel modified by an edge plus filter. D displays the collagen IV mask and E reveals the final measurement objects.

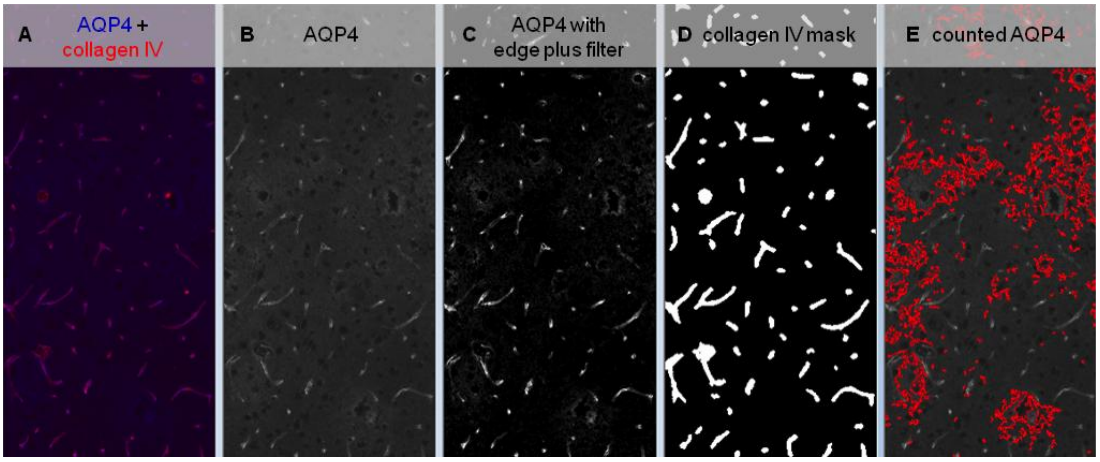

Figure 22: Example of the measurement of parenchymal AQP4 in a mouse CTX (Histo-ID 2445/12, level 8). A shows the composite image of the AQP4 and collagen IV channel, whereas B only presents the AQP4 immunolabeling, which was corrected using the edge plus filter to optimize measurement (C). Furthermore the collagen IV mask (D) was subtracted to obtain the total amount of parenchymal AQP4 (encircled in red, E).

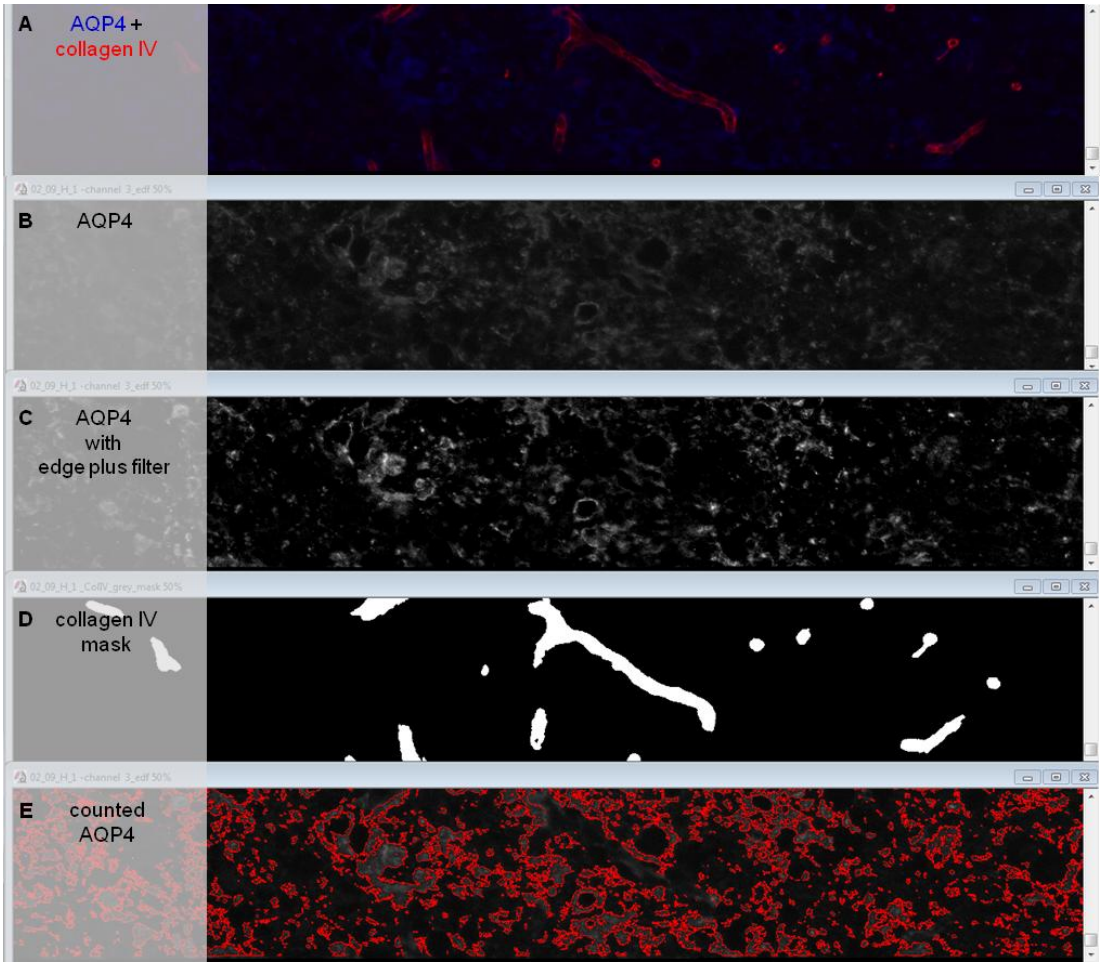

Figure 23: Example of parenchymal AQP4 measurement in the HC of a human section (Braak stage V/VI, IRN 02/09). A shows the composite image of the AQP4 and collagen IV channel, whereas B only presents the AQP4 immunolabeling, which was corrected using the edge plus filter to optimize measurement (C). Furthermore the collagen IV mask (D) was subtracted to obtain the total amount of parenchymal AQP4 (encircled in red, E).

Table 9: Measurement parameters. Table shows threshold range, dynamic factor and minimal object size of the distinct evaluations.

Evaluation	Threshhold Range	Dynamic Factor	Minimal Object Size
Total human amyloid (6E10) in mouse tissue	10 - 255	1.2	> 7 µm^2
Total human amyloid (6E10) in human tissue	20 - 255	n.a.	> 7 µm^2
Total collagen IV in mouse tissue	20 - 255	n.a.	> 13 µm^2
Total collagen IV in human tissue	30 - 255	1.2	> 13 µm^2
CAA in mouse tissue	10 - 255	1.2	> 7 µm^2
CAA in human tissue	90 - 255	n.a.	> 7 µm^2
Total Aβ40/42 (MOAB-2) in mouse tissue	40 - 255	1.2	> 7 µm^2
Total AQP4 in mouse tissue	20 - 255	n.a.	> 7 µm^2
Total AQP4 in human tissue	7 - 255	n.a.	> 7 µm^2
Vascular related AQP4 in mouse tissue	20 - 255	n.a.	> 7 µm^2
Vascular related AQP4 in human tissue	7 - 255	n.a.	> 7 µm^2
Parenchymal AQP4 of mouse tissue	20 - 255	n.a.	> 7 µm^2
Parenchymal AQP4 of human tissue	7 - 255	n.a.	> 7 µm^2

2.6 Statistical Analysis

All data were analyzed using Graph-Pad Prism (version 4.03). Descriptive statistical analyses were performed on all evaluated parameters including tests for normal distributions (Kolmogorov-Smirnov test). Data were averaged and represented as mean + standard error of mean (SEM). An alpha-error level of $p < 0.05$ was considered significant.

For comparison of the size of mouse regions, Student's *T* test was applied as the variables met the normal distribution.

Group differences were calculated by either one-way or two-way ANOVA, followed by Bonferroni's post-hoc analysis. Values of nTg mice were excluded in analysis of human amyloid and CAA since they do not have human protein.

3 RESULTS

3.1 Quality of Labelings

3.1.1 Labeling of SMA, 6E10, Collagen IV and DAPI (Experiment I)

Structures of blood vessels and features of CAA were visualized using a combination of three antibodies directed against smooth muscle actin (SMA), Aβ and APP C-terminal fragments (clone 6E10), and collagen IV.

With the exception of the SMA antibody, which did not label mouse and human tissue, immunofluorescent labeling of 6E10 and Collagen IV worked well on both tissue types. 6E10 and collagen IV labeling, as well as DAPI counterstaining had an excellent signal to noise ratio suitable for automated object detection. The protocol led to highly specific labeling of the primary antibodies. Figure 24 and Figure 25 show examples of the labeling on an APP_{SL} mouse section and a human sample, respectively. Unspecific binding of secondary antibodies was absent from operational negative control sections; examples are presented in Figure 26 (mouse section) and Figure 27 (human section). This excludes any cross-reactions of the applied secondary antibodies to the tissue and suggests that blocking worked well. The remaining signal derives from autofluorescent lipofuscin (LF) deposits that are frequent in aged brains or in brains of tg mice that overexpress large amounts of foreign protein due to use of an excessively strong promotor. Considering the contribution of LF and other unspecific sources is of importance, since this signal can severely bias fluorescent quantification. Unspecific AF must therefore be identified and excluded from the measurement. Technically, LF-derived AF can be distinguished from immunofluorescence by imaging in additional channels that should be devoid of immunofluorescent signal from fluorophore-labeled secondary antibodies.

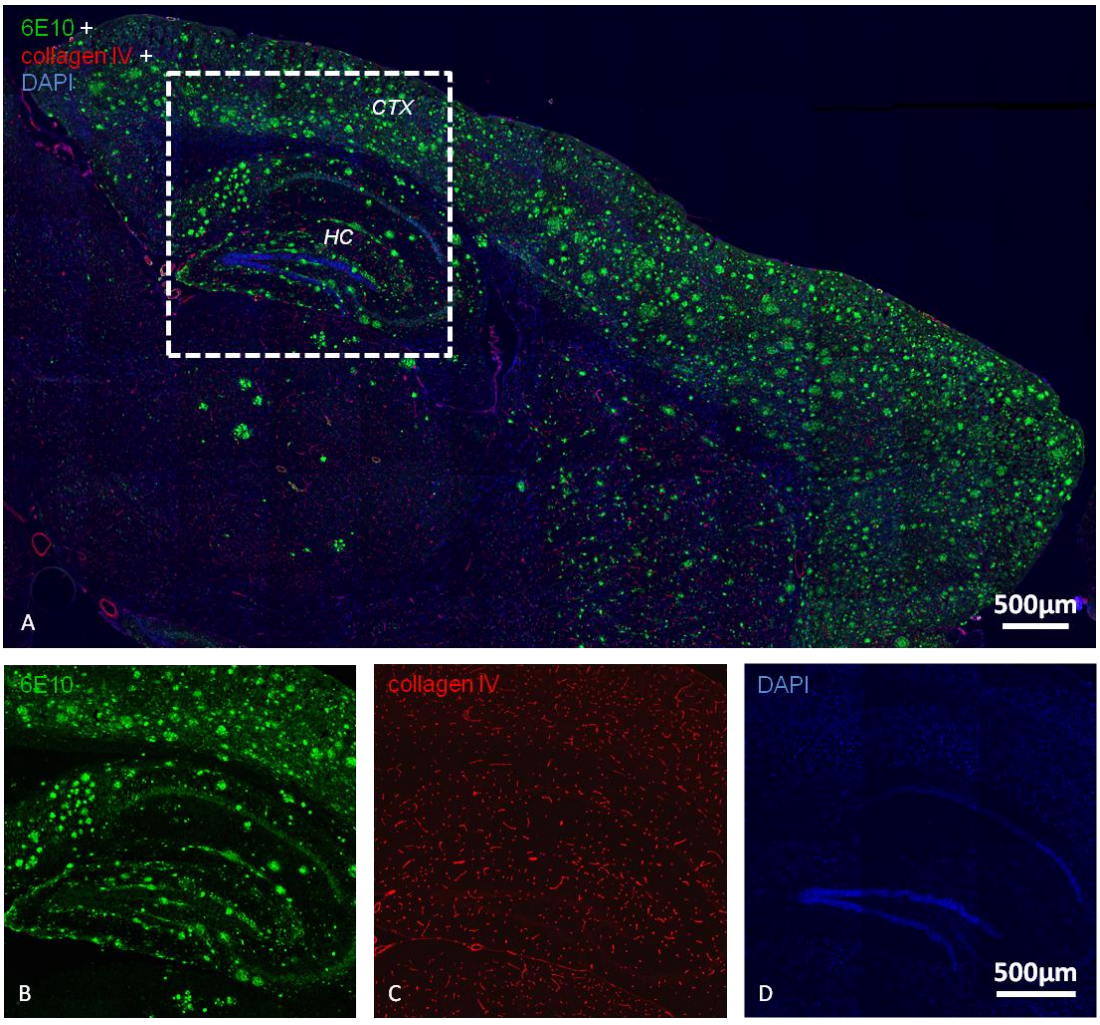

Figure 24: Quality of immunofluorescent labeling of a mouse section. No cross-reactivity was observed, ensuring optimal separation of the markers. A merged image of 6E10 (green), collagen IV (red) and DAPI (blue) labeling is shown in A. Details of the particular labelings are presented in B, C and D, separate for each channel. Histo-ID 1653/11, level 6; CTX = cortex, HC = hippocampus.

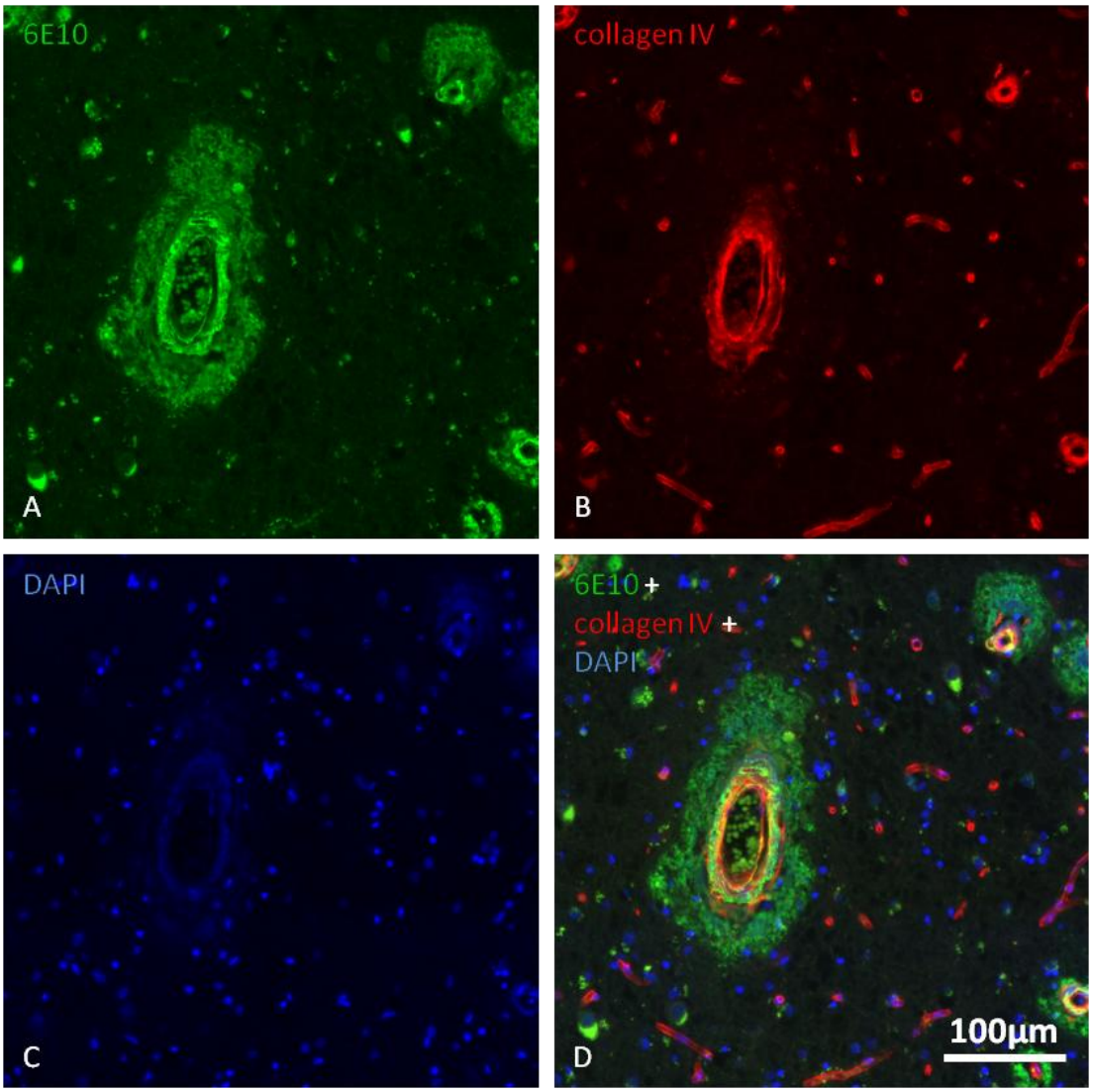

Figure 25: Representative images of the double immunofluorescent labeling of 6E10 and blood vessels by collagen IV in the HC of human tissue. Images show 6E10 (green, A), and collagen IV (red, B) IR as well as cell nuclei counterstained with DAPI (blue, C). The composite image of the different channels is presented in D. Note that in late stage AD amyloid accumulates in a large penumbra around the vessel wall. IRN 02/09, stage V/VI.

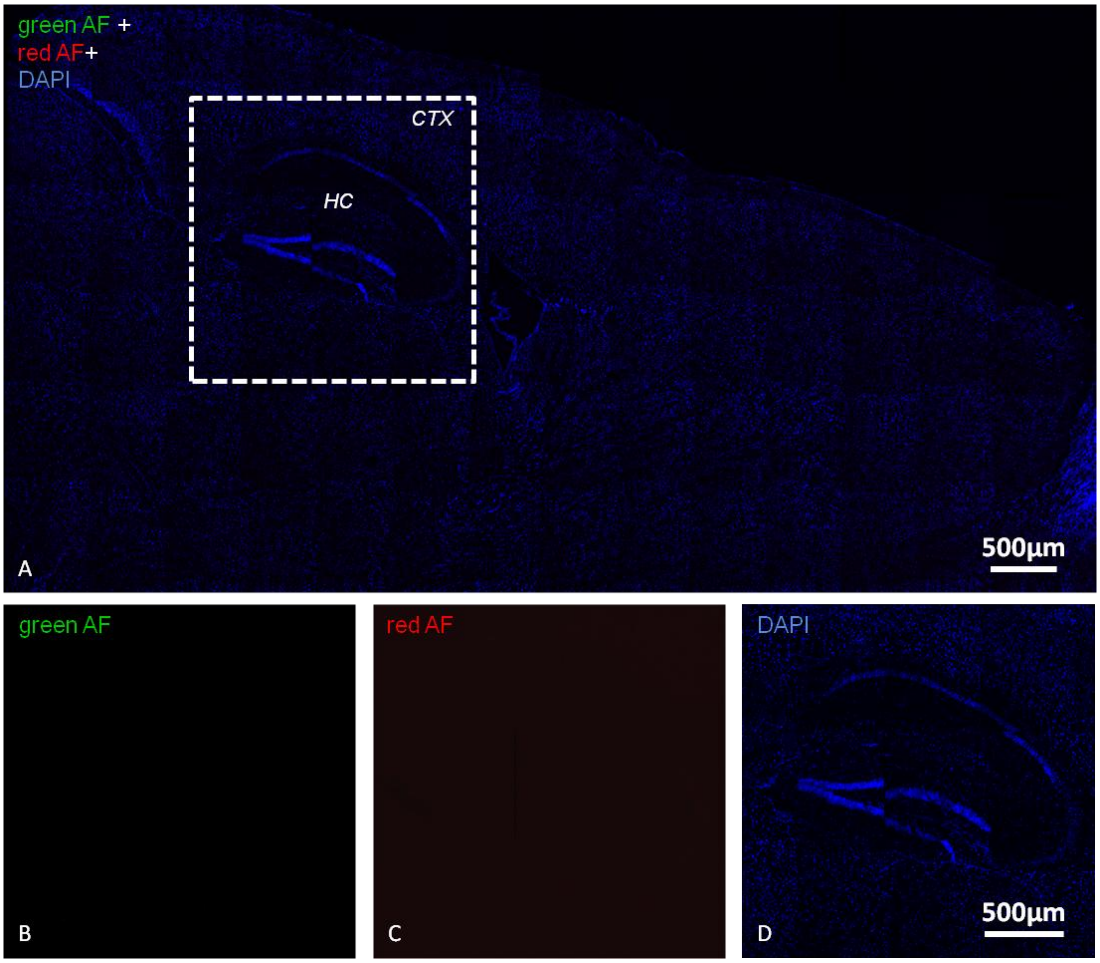

Figure 26: Example of immunohistochemical labeling of the negative control. Secondary antibodies did not show unspecific bindings. Image A shows the composite image of all channels, whereas B and C show the absence of the secondary antibody labeling. D displays cell nuclei due to the DAPI counterstaining (blue, D). Remaining AF derives from LF. Histo-ID 1653/11, level 5; AF = autofluorescence, CTX = cortex, HC = hippocampus.

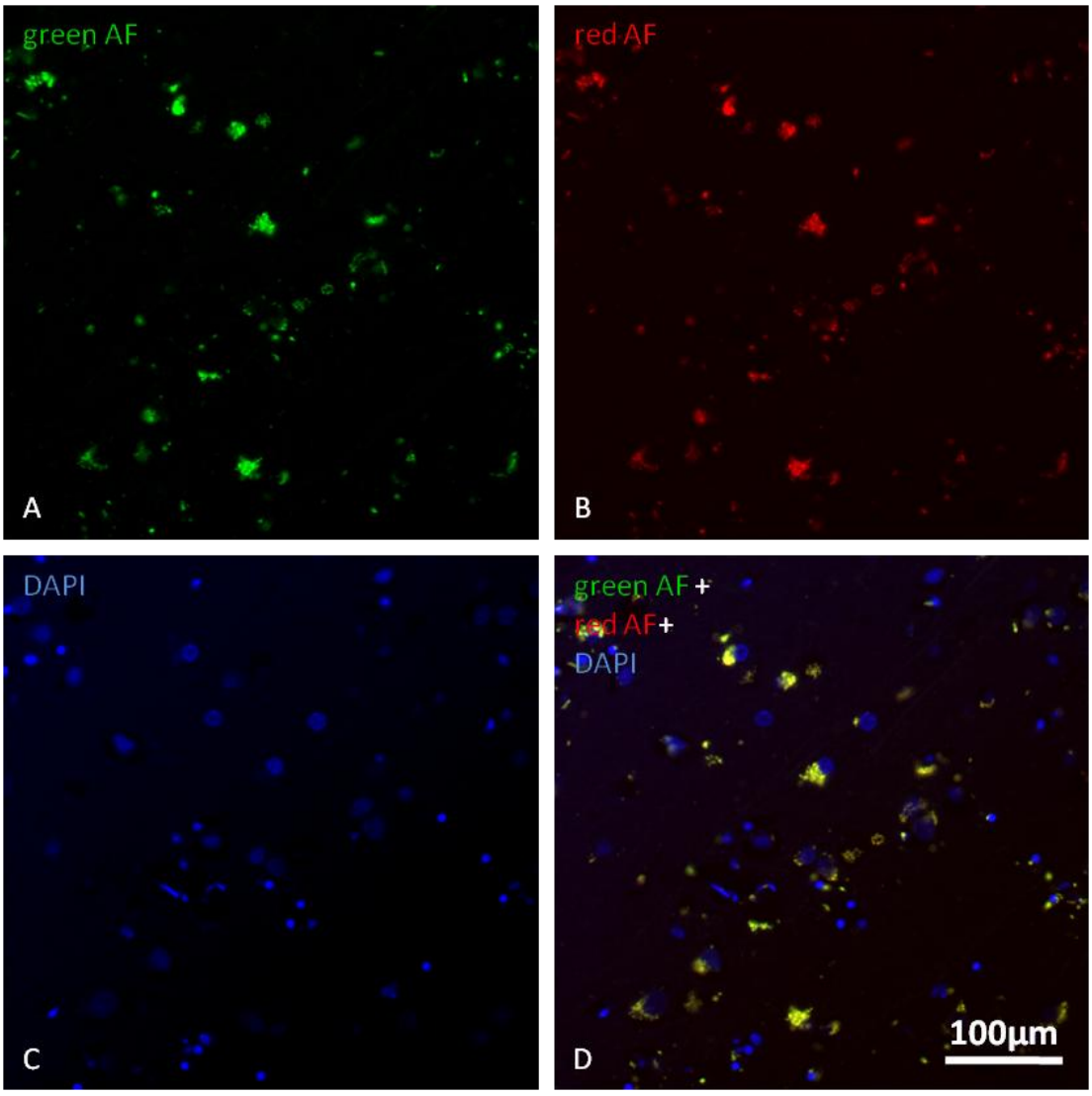

Figure 27: Negative control labeling of the HC of human tissue. No unspecific binding of secondary antibodies is visible. Images show autofluorescent objects, mainly erythrocytes and LF deposits in human brain samples. Examples of the separately recorded channels are provided in panels A-D – green AF (green, A), red AF (red, B) and DAPI (blue, C), as well as the merged image (D). Remaining AF derives from LF. IRN 1016/11; AF = autofluorescence.

3.1.2 Labeling of Aβ40/42, Collagen IV and AQP4 (Experiment II)

For the quantification of human Aβ40 and Aβ42, a monoclonal anti-amyloid β antibody (clone MOAB-2) was used. Determination of blood vessels was as previously performed using the anti-collagen IV antibody, and AQP4, which forms specialized water channels in the CNS, was detected by a polyclonal anti-AQP4 antibody.

MOAB-2 only worked on mouse brain sections. A reason for dysfunction on human tissue might be that the samples were paraffin embedded. All other antibodies

worked well on mouse and human sections. Therefore the labeling was suitable for automated quantification of collagen IV and AQP4. Representative examples for the triple- or double- staining are shown in Figure 28 (mouse section) and Figure 29 (human section). The secondary antibodies specifically detected their corresponding primary antibodies. Images of the omitted primary negative controls are presented in Figure 30 (mouse section) and Figure 31 (human section).

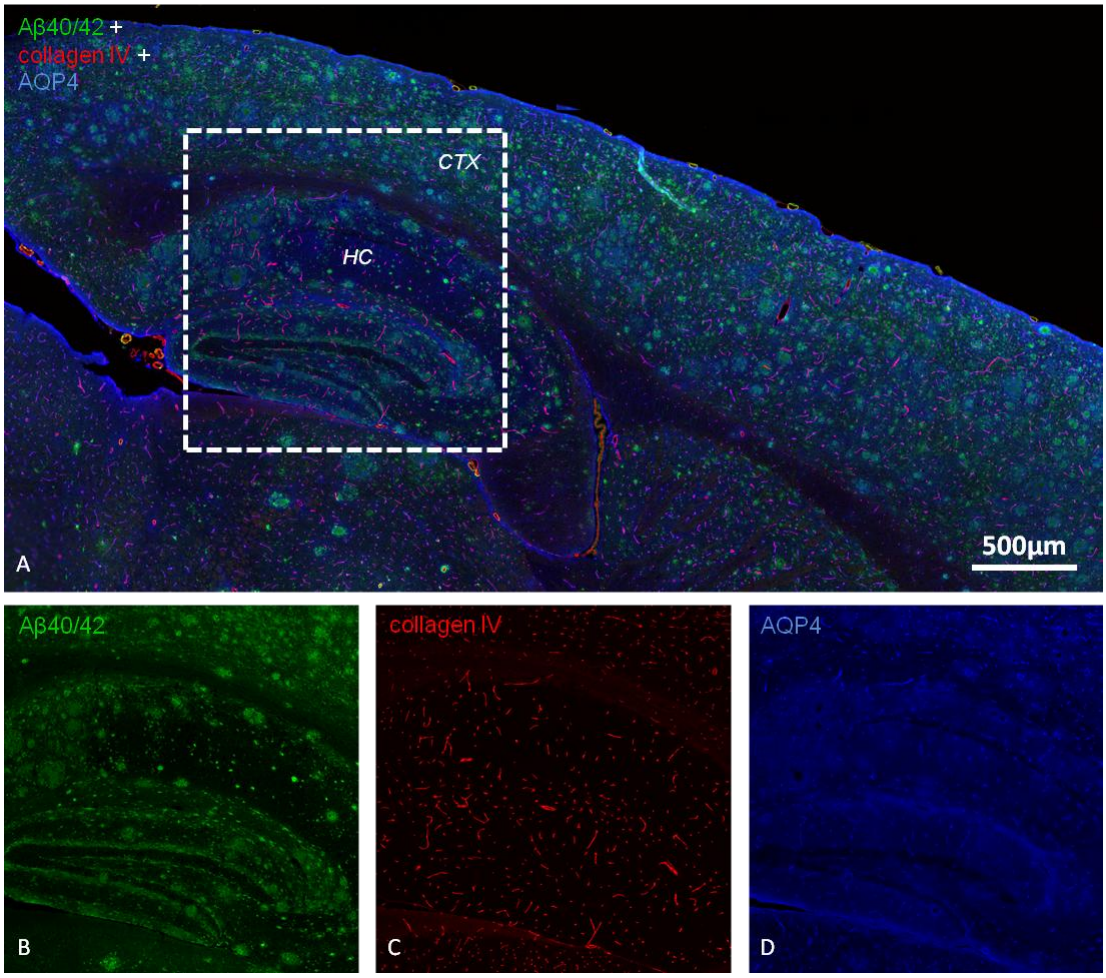

Figure 28: Representative example of triple immunofluorescent labeling in brain tissue of a 12 months old APP_{SL} mouse. A merged image of Aβ40/42 (green), collagen IV (red) and DAPI (blue) labeling is shown in A. B, C and D show individual labelings of Aβ40/42 (green), collagen IV (red) and AQP4 (blue). Histo-ID 2242/11, level 6; CTX = cortex, HC = hippocampus, AQP4 = aquaporin 4.

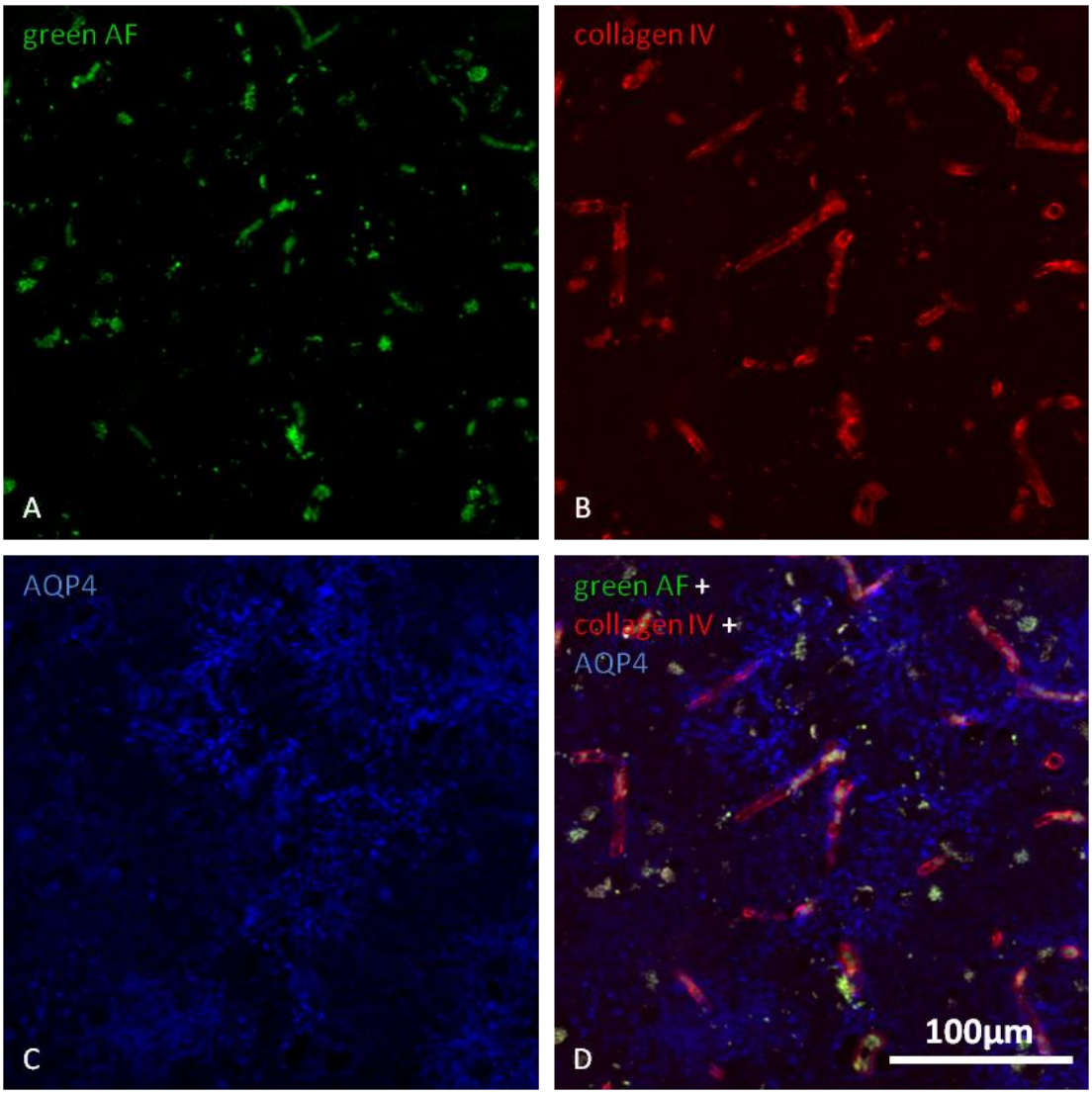

Figure 29: Quality of immunofluorescent labeling of collagen IV and AQP4 in the frontal CTX of a human section (IRN 561/11, Braak stage V/VI). Panels show green AF (green, A), collagen IV (red, B) IR and AQP4 (blue, C). The composite image of the different channels is presented in D. IRN 02/09, stage V/VI; AF = autofluorescence, AQP4 = aquaporin 4.

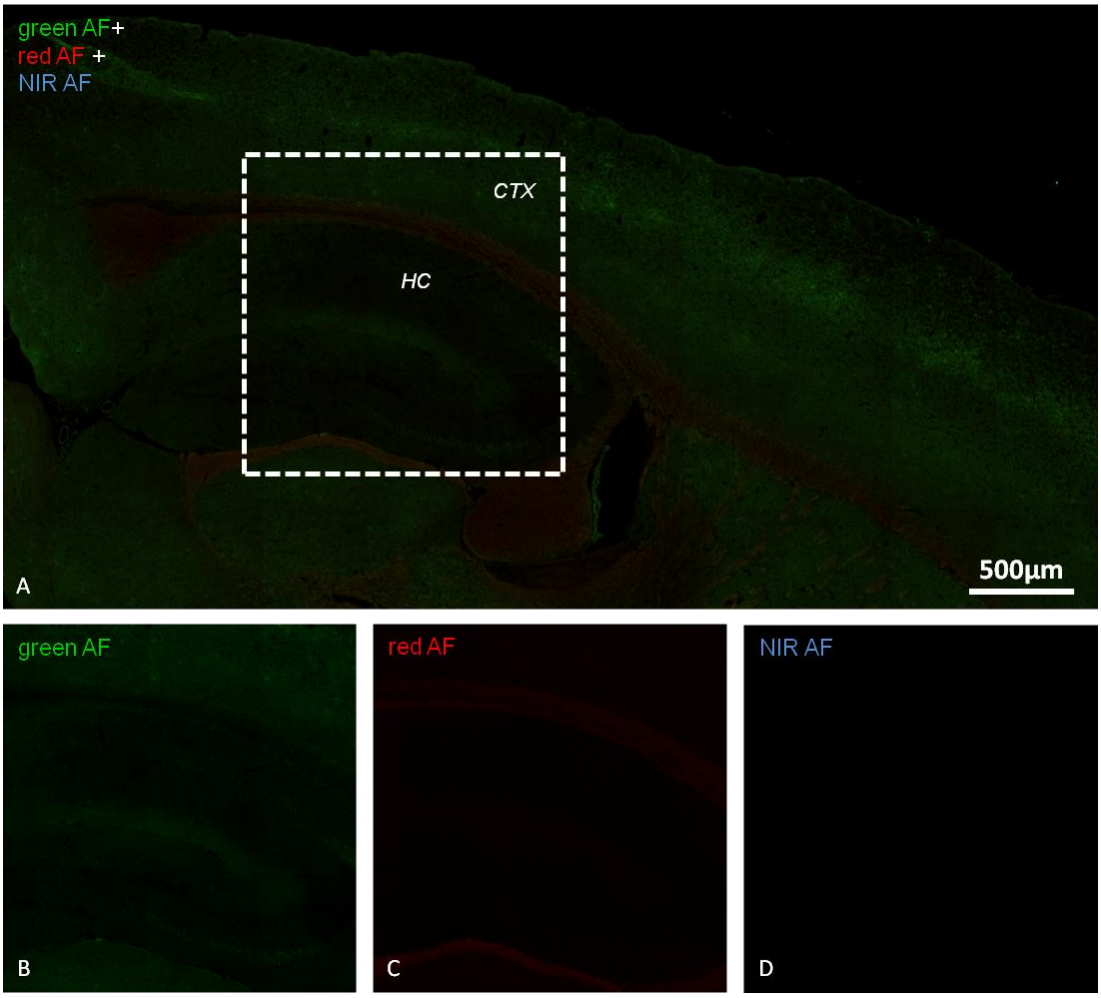

Figure 30: Imaging the negative control section showed absence of immunofluorescence in each channel. The negative control was labeled in parallel with all other sections, except the primary antibody incubation steps were skipped. No labeling was observed in the merged (A), and also distinct channels (B-D). This result indicates that secondary antibodies did not cross-react with tissue immunoglobulins. Remaining AF derives from LF. Histo-ID 336/11, level 7; NIR AF = near infrared autofluorescence, CTX = cortex, HC = hippocampus.

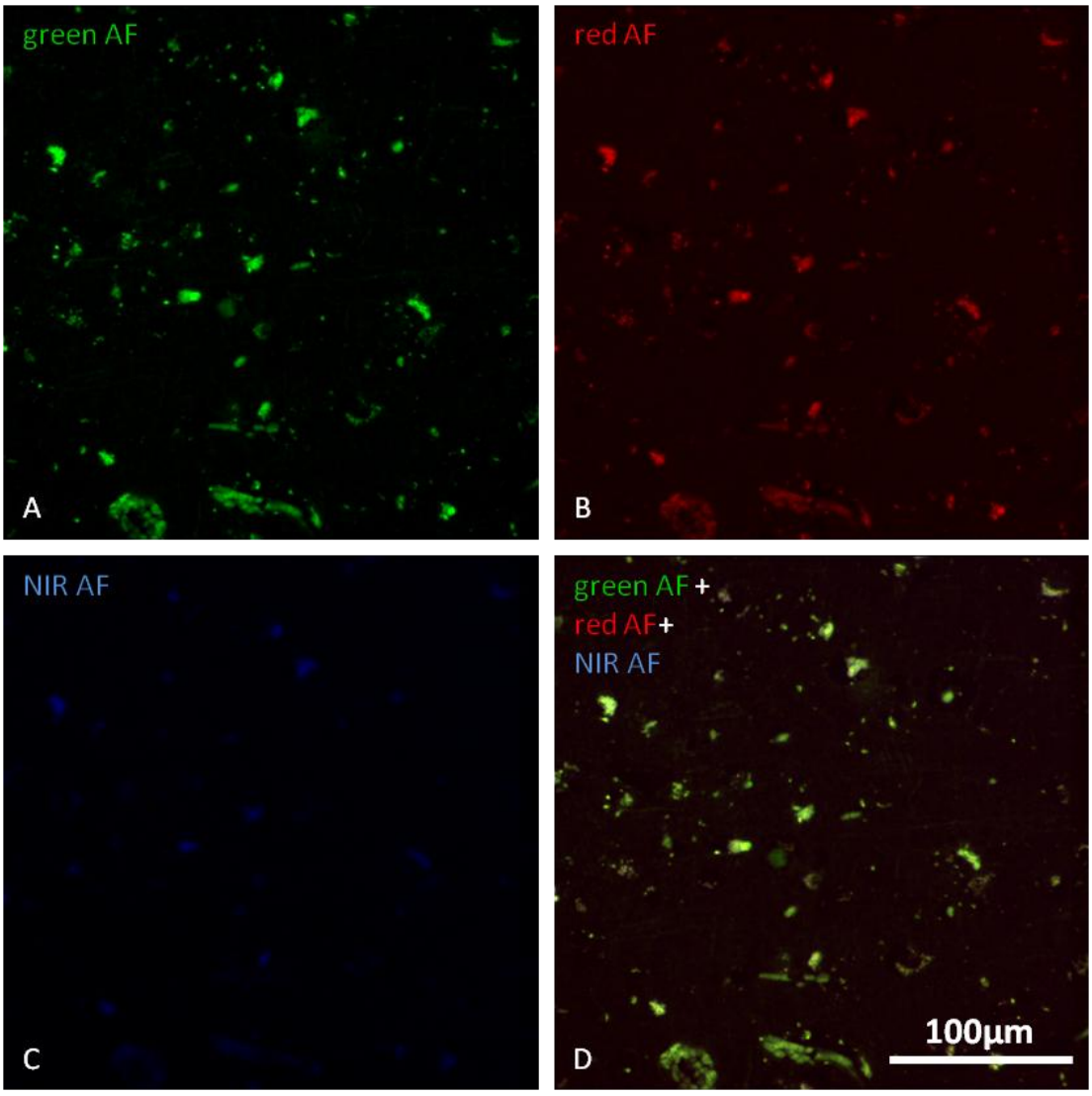

Figure 31: Negative control labeling of the frontal CTX of human tissue. In order to test whether the secondary antibodies may cross-react with tissue, a negative control was included in each experiment. They were treated as the normal sections, except the primary antibodies were omitted from the incubation. Images present the imaged channels – autofluorescence (green, A), collagen IV (red, B) and AQP4 (blue, C), as well as the merged image (D). Remaining AF derives from LF. IRN 561/11, Braak stage V/VI, frontal CTX; NIR AF = near infrared autofluorescence.

3.2 Quantification of Mouse Brain Region Size

The analysis of the total average region size of either the CTX or the HC shows that in both experiments the size of the evaluated brain regions did not differ between the APP_{SL} mice and the nTg controls and the variation of the regions within the groups was low (see Figure 32). This result indicates that no sampling bias occurred during tissue sampling and that adverse effects such as uneven tissue shrinkage were avoided. Furthermore, it demonstrates that in total the size of the analyzed

regions per animal was equal and that no atrophy was evident in the model up to the age of twelve months.

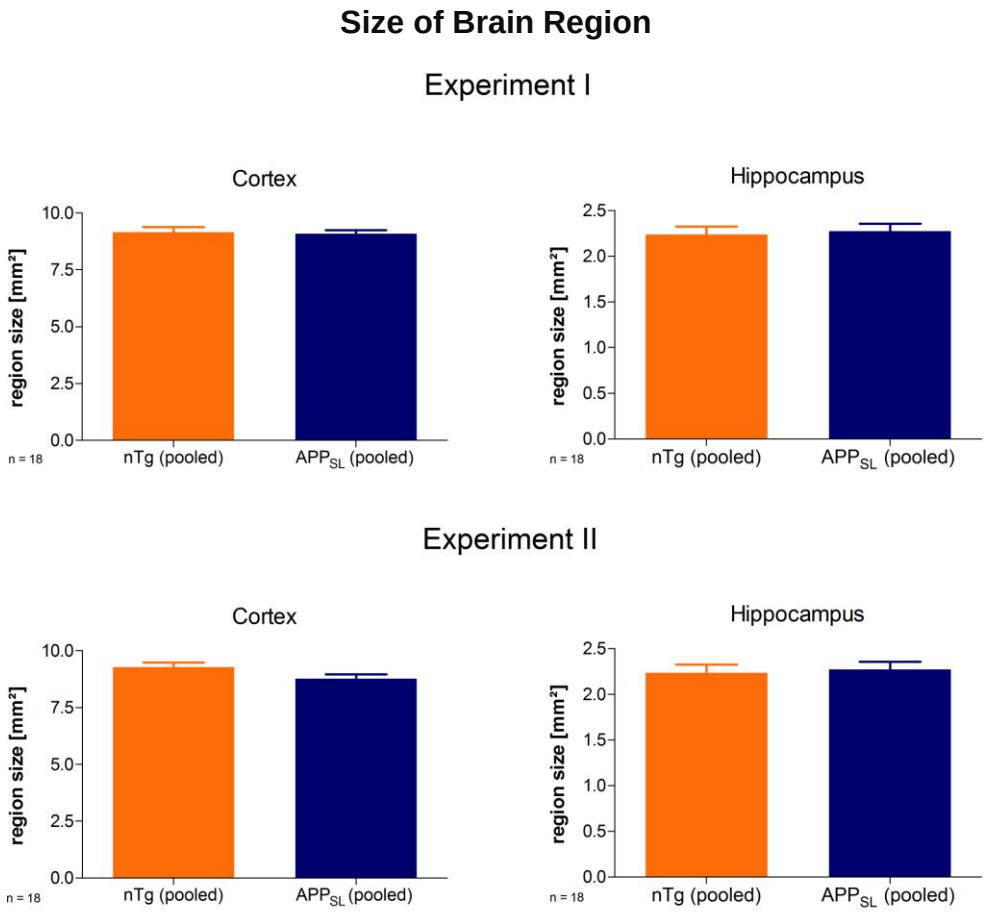

Figure 32: Quantification of region size of the CTX and the HC in nTg (orange bars) and APP_{SL} mice (blue bars). In total the average region size does not differ between genotypes. Bar graphs show group means + SEM. Group size: n = 18.

3.3 Quantification of 6E10

Immunostaining of the amino acid residues 1-16 of Aβ using the 6E10 antibody was quantified in the CTX and in the HC of human and mouse brain sections.

3.3.1 6E10 Immunofluorescence in Mouse Sections

The nTg group showed small amounts of measured signal, indicating the quantity of biological “waste”, especially LF, in the evaluated regions. APP_{SL} mice had high 6E10 IR, which was significantly increased with age in the CTX (at least $p < 0.05$). In the HC the progression was significant between nine and twelve months of age

($p < 0.001$). Representative images of the 6E10 labeling are presented in Figure 33 and results of quantifications are shown in Figure 34.

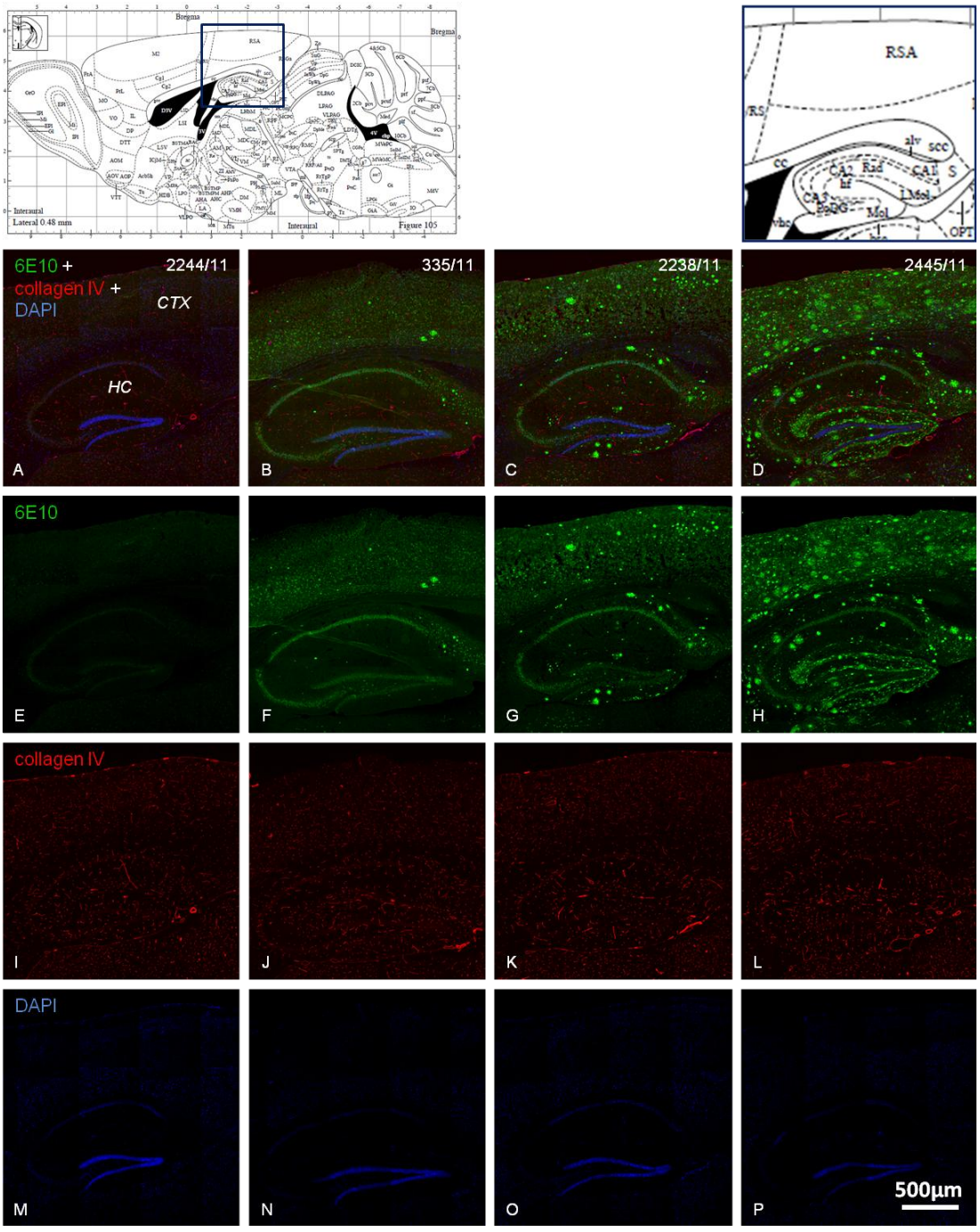

Figure 33: Representative examples of 6E10 + collagen IV + DAPI labeling. Images on the left show the merged image (A) and the individual color channels of the triple-labeling of a 12 months old nTg mouse, which does not show any 6E10 IR (E), whereas collagen IV IR (I) is similar to APP_{SL} mice. Images of 6 (B), 9 (C) and 12 (D) months old APP_{SL} mice display high intensity of 6E10 that increases with age (F, G and H). Further, they showed increasing intensity and density of collagen IV-positive objects over age (J, K and L). M-P show cell nuclei with DAPI. Layouts on the head of the images give an overview of the coordinates of the presented images. Schemes were taken from[57]. CTX = cortex, HC = hippocampus.

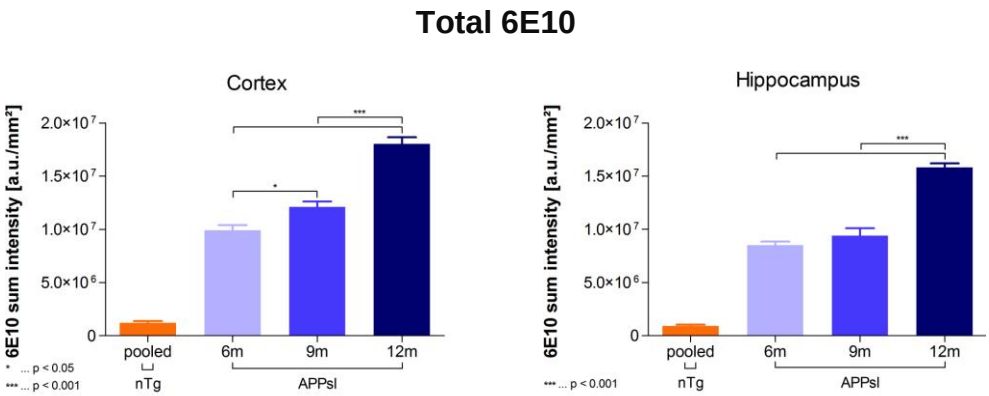

Figure 34: Graphs show normalized sum intensity of 6E10 immunolabeling in the CTX and the HC of nTg (data of 6, 9 and 12 months old animals were summarized; orange bars) and APP_{SL} mice with different ages (6, 9 and 12 months; blue bars). Tg animals showed an age-depend increase of 6E10. Small amount of density in nTgs shows the amount of autofluorescent objects, such as LF. Data are presented as means + SEM. Group size of nTg: n = 18; Group size of Tg: n = 6.

3.3.2 6E10 Immunofluorescence in Human Sections

At Braak stage V/VI the frontal, temporal and cingulate cortices (and due to this the total CTX) showed significantly increased 6E10 IR (at least $p < 0.05$) compared to the control group. A non-significant trend of increasing 6E10 IR was noted in most cortical regions already at earlier Braak stages, especially at stage III/IV in the frontal and occipital CTX (see Figure 35).

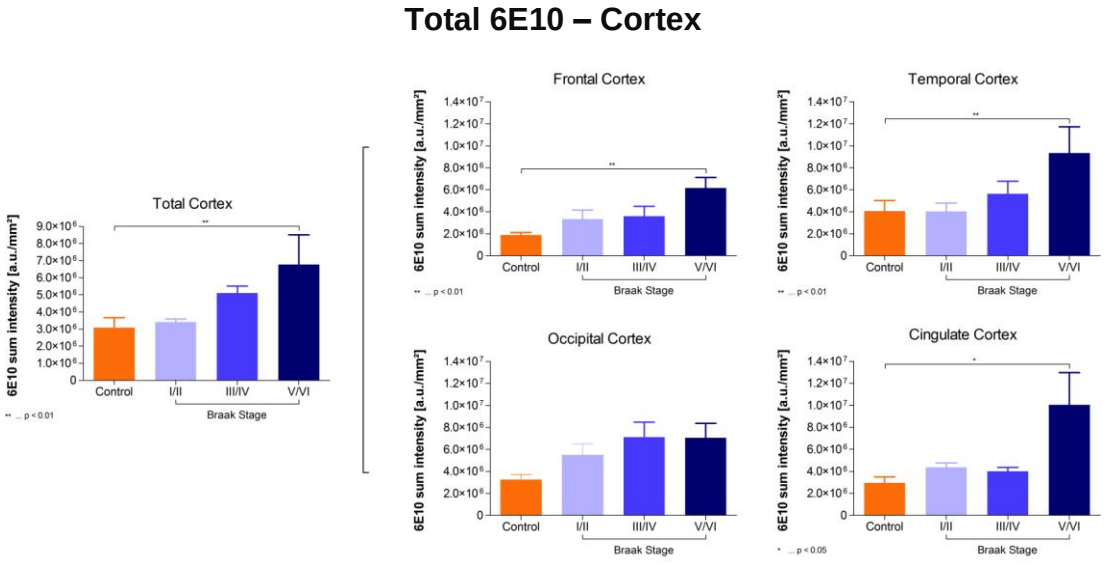

Figure 35: Quantification of total 6E10 IR in total human CTX and in distinct cortical areas in the control group (orange bars) versus the AD groups at different Braak stages (I/II, III/IV and V/VI; blue bars). Graphs show the normalized sum signal intensity of 6E10 in the total human CTX and in several different cortical areas. 6E10 intensity was significantly increased in the total CTX, as well as in the frontal, temporal and cingulate CTX at Braak stage V/IV compared to the control group. Furthermore in all areas a trend towards increasing 6E10 IR in higher Braak stages was observed. Data are presented as means + SEM. Group size: n = 5.

Within the HC a significantly (at least $p < 0.05$) higher level of 6E10 IR was observed at Braak stages III/IV and V/VI compared to the control group (see Figure 36). Notably, 6E10 IR was already high at early stage and did not show a stage-dependent progression in this region. Representative examples of the immunolabeling are presented in Figure 37.

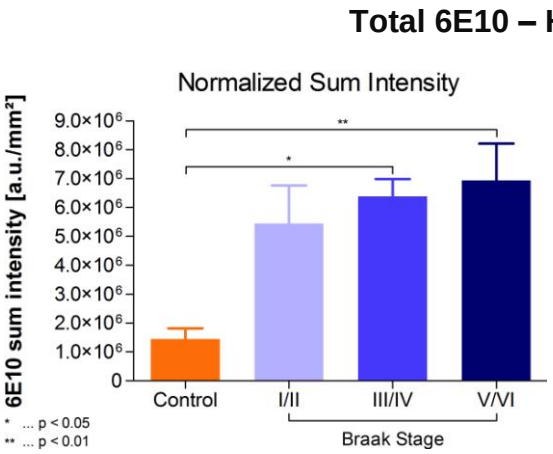

Figure 36: Quantification of 6E10 in the HC of the control group (orange bars) versus the groups at different Braak stages (I/II, III/IV and V/VI; blue bars). Graph shows the normalized sum signal intensity of 6E10 IR in the human HC, indicating a significantly higher load of 6E10 IR in advanced Braak stages. Note that at early Braak stage I/II 6E10 IR was non-significantly higher already compared to the control group. Data are presented as means + SEM. Group size: n = 5.

3.4 Quantification of Total Collagen IV

For the examination of cerebrovascular structures a specific anti-collagen IV antibody was used for labeling blood vessels on mouse and human sections. Based on the immunofluorescence, the total amount of collagen IV and the numerical density and the average diameter of cerebral blood vessels were quantified.

3.4.1 Collagen IV Immunofluorescence in Mouse Sections

Quantitative analysis of the collagen IV labeling of mouse tissue showed a significant (at least $p < 0.05$) increase of sum collagen IV signal in the CTX and the HC of nine and twelve months old tg mice compared to APP_{SL} mice at an age of six months. Additionally, the tg mice showed a significant (CTX: at least $p < 0.05$, HC: $p < 0.01$) rise of collagen IV between the age of nine and twelve months. The object density of collagen IV-positive object did not display any changes in both regions, indicating that there is no difference in the total number of blood vessels. In contrast, the mean object size was significantly (CTX: at least $p < 0.01$, HC: at least $p < 0.05$) increased over age in both regions. This result indicates that in average cortical and hippocampal blood vessels were significantly enlarged with increasing age. Data are

presented in Figure 38 and representative images of the triple-labeling are shown in Figure 33.

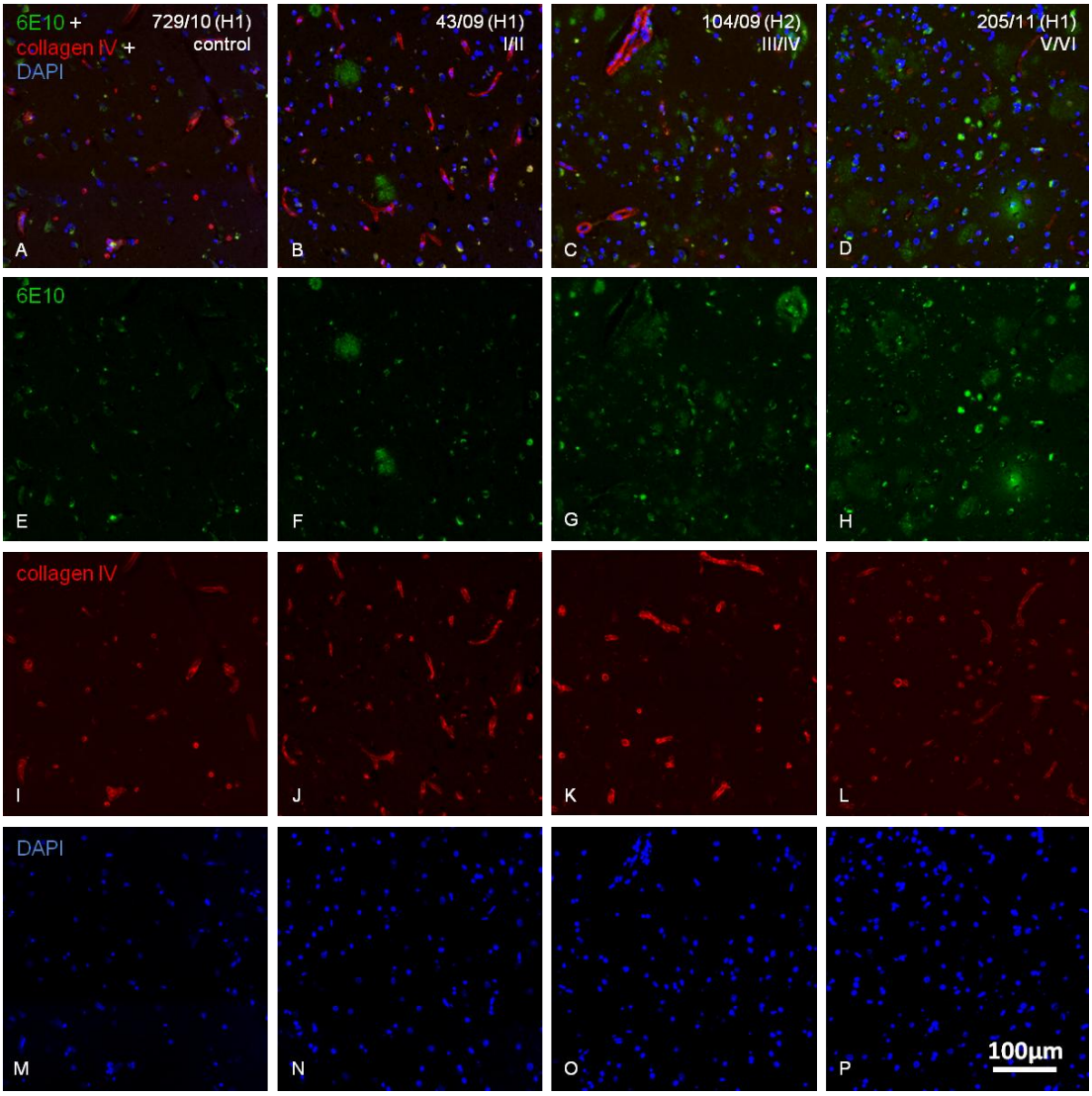

Figure 37: Representative examples of 6E10 + collagen IV + DAPI triple-labeling of human HC. Images on the left side present the labeling of one control sample (A, E, I and M), showing no 6E10 IR (E) and fewer blood vessels stained with collagen IV (I). Images in the center left column show the merged labeling and the individual channels of a patient at Braak stage I/II (B, F, J and N). The center right column represents images of the hippocampal labeling at stage III/IV (C, G, K and O) and the right column at stage V/VI (D, H, L and P). AD patients showed increasing intensity of 6E10 IR plaque load and collagen IV in advanced Braak stages. H = hippocampus.

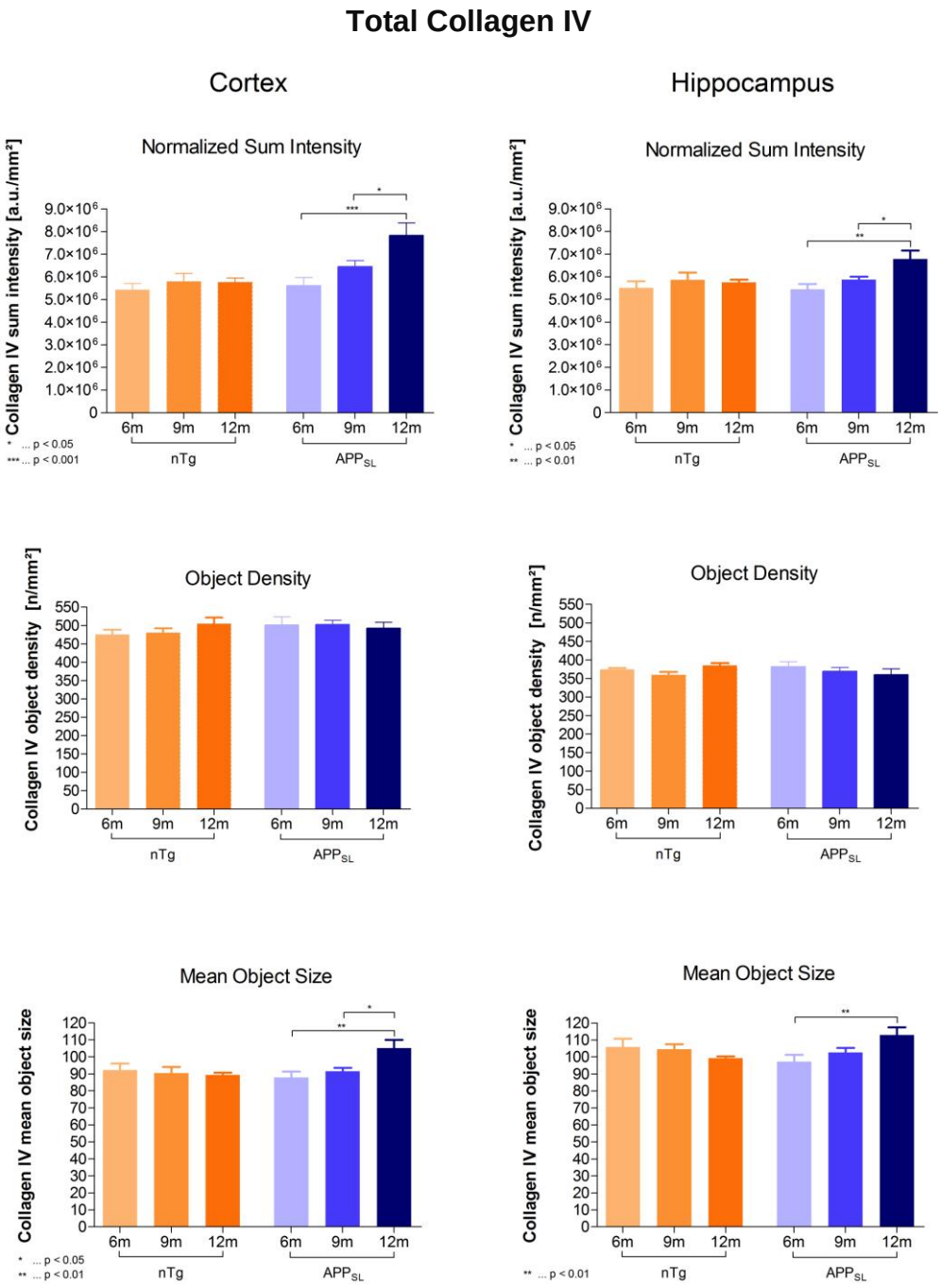

Figure 38: Graphs show normalized sum intensity, object density and mean object size of collagen IV immunolabeling in the CTX (left) and HC (right) of 6, 9 and 12 months old nTg (orange bars) and APP_{SL} (blue bars) mice. APP_{SL} mice exhibited significantly higher amounts of collagen IV in the CTX and the HC over age. The number of collagen IV-positive objects did not show any alteration in either genotype or brain region. Data are presented as means + SEM. Group size: n = 6.

In the comparison of the age-matched nTg and tg animals, the twelve months old APP_{SL} mice showed significantly higher collagen IV levels in the CTX ($p < 0.001$) and the HC ($p < 0.05$). Furthermore, the mean object size was significantly (CTX: $p < 0.01$, HC: $p < 0.05$) increased in twelve months old tg animals in both brain regions compared to nTgs. Data are presented in Figure 39.

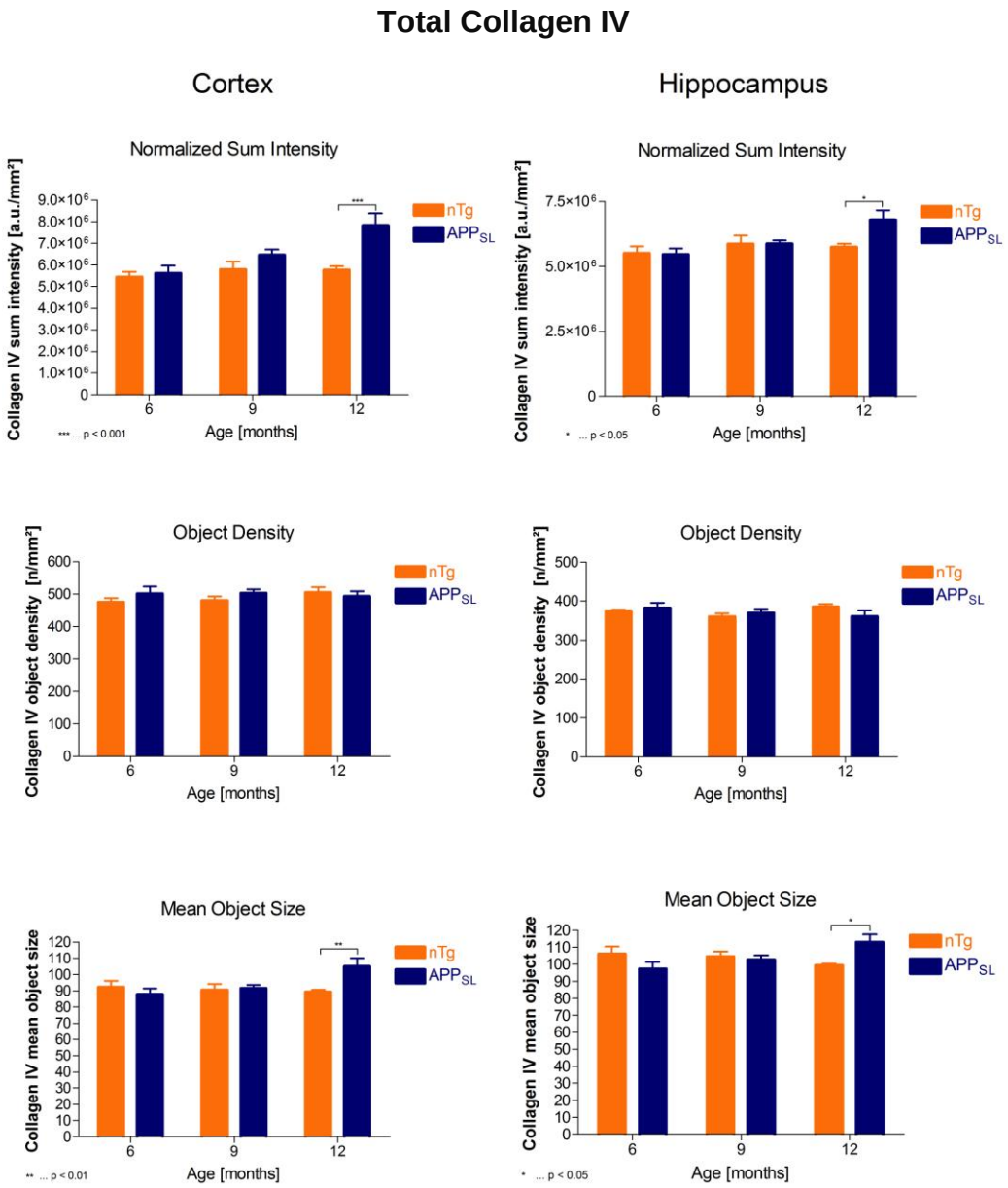

Figure 39: Graphs show normalized sum intensity, object density and mean object size of the collagen IV evaluation in an age-matched comparison of 6, 9 and 12 months old nTg (orange bars) and APP_{SL} (blue bars) mice. At 12 months collagen IV IR was significantly higher in the CTX and the HC of APP_{SL} compared to age-matched nTg mice. Furthermore the tg mice showed significantly larger objects in both regions at that age. Data are presented as means + SEM. Group size: n = 6.

3.4.2 Collagen IV Immunofluorescence in Human Sections

Quantification of collagen IV in human samples revealed no significant changes in any cortical area. At least, a trend in increasing collagen IV intensity with advanced stages was detected in the frontal and cingulate CTX (see Figure 40). Furthermore there were no indications of any changes in the numerical density of blood vessels (see Figure 41) and the mean vessel size (see Figure 42).

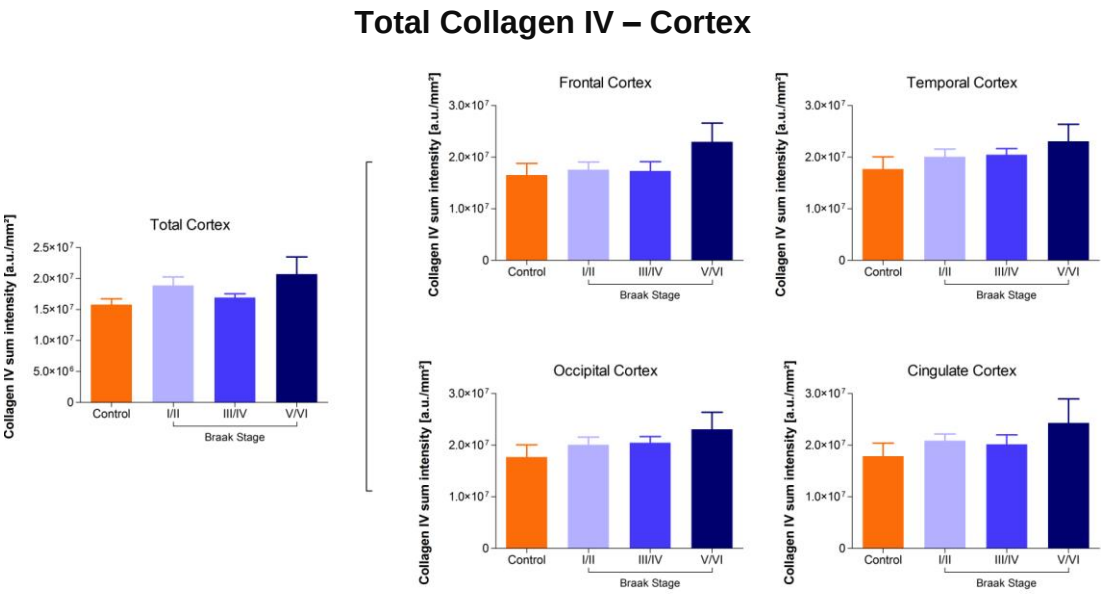

Figure 40: Quantification of total collagen IV IR in total human CTX and distinct cortical areas in the control group (orange bars) versus the groups at different Braak stages (I/II, III/IV and V/VI; blue bars). The collagen IV immunolabeling did not reveal any changes in the CTX. Nevertheless, a trend of increasing collagen IV intensity with advanced AD was detectable in the frontal and cingulate CTX. Data are presented as means + SEM. Group size: n = 5.

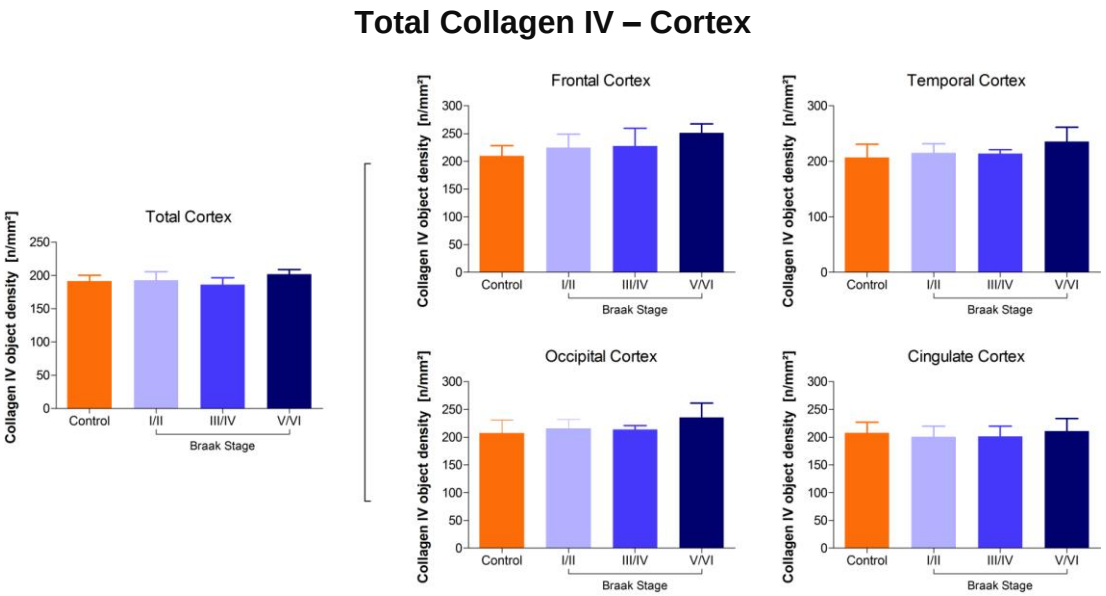

Figure 41: Graphs represent the density of collagen IV-positive objects in the total CTX and the different cortical areas in the control group (orange bars) as well as in three groups at different Braak stages (I/II, III/IV and V/VI; blue bars). There were no detectable changes in the number of collagen IV-positive objects. Data are presented as means + SEM. Group size: n = 5.

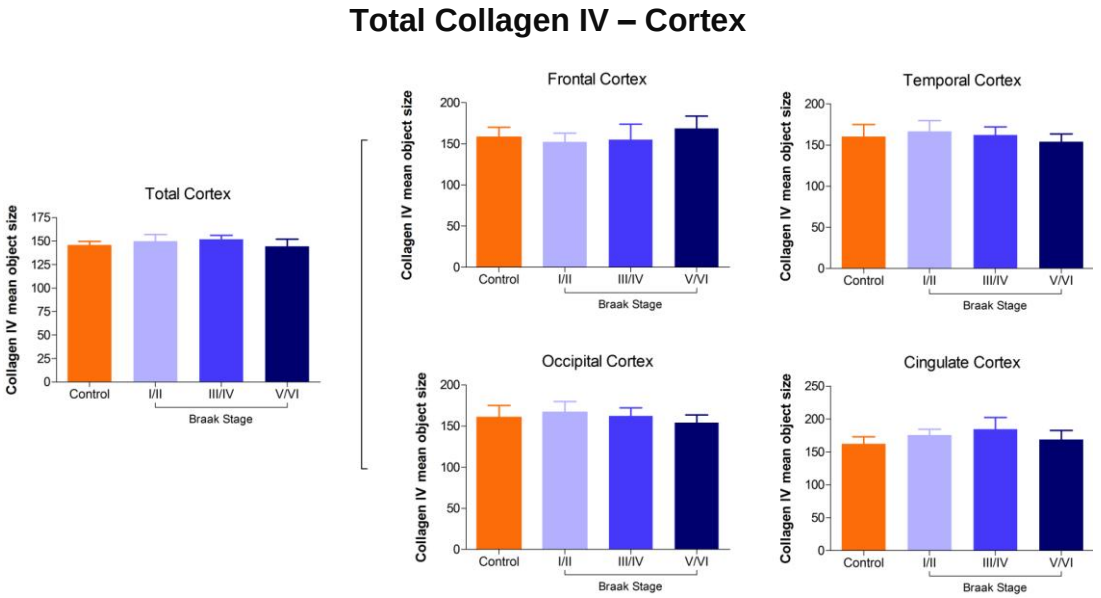

Figure 42: Graphs represent the mean object size of collagen IV-positive objects in the total and several analyzed cortical areas in the control group (orange bars) and in three groups at different Braak stages (I/II, III/IV and V/VI; blue bars). No alterations in the averaged size of collagen IV-positive objects were evident. Data are presented as means + SEM. Group size: n = 5.

In contrast to the CTX, the collagen IV intensity and the numerical object density were significantly ($p < 0.05$) higher in the HC at Braak stages V/VI compared to the control group, whereas the mean object size did not change. Importantly, both readouts are normalized to the area size, and any change in the structure of gray matter (e.g. due to neuronal cell loss) will affect these normalized data. The results are therefore consistent with the notion that the overall number and size of blood vessels does not adapt to AD-associated hippocampal shrinkage. Data of collagen IV quantification of the HC are presented in Figure 43.

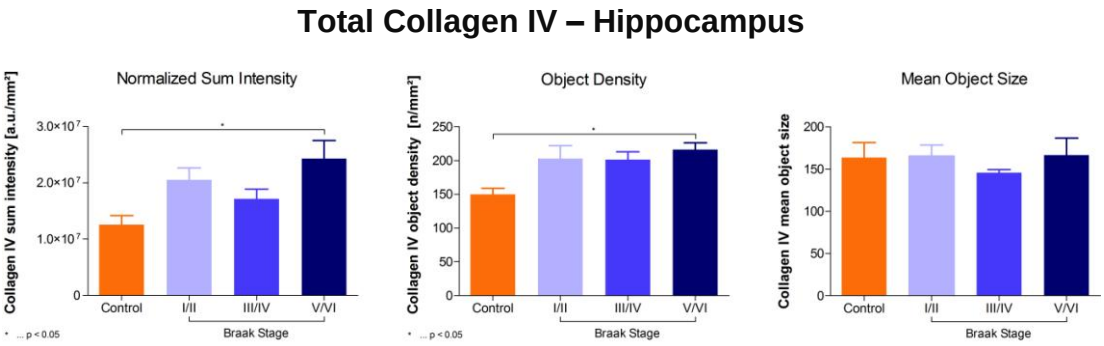

Figure 43: Graphs represent the normalized sum intensity, the object density and the mean size of collagen IV-positive objects in the HC in a control group (orange bars) and at different Braak stages (I/II, III/IV and V/VI; blue bars). The group with a Braak stage V/VI had significantly higher sum collagen IV intensity as well as more frequent collagen IV-positive objects than the control group. Data are presented as means + SEM. Group size: n = 5.

3.5 Quantification of CAA

The amount of CAA was analyzed in mouse and human brain samples. Therefore the 6E10 IR within the expression of collagen IV in cerebral blood vessels was quantified.

3.5.1 CAA in Mouse Sections

The CTX and the HC showed significantly (CTX: at least $p < 0.01$, HC: $p < 0.001$) increased amounts of CAA with advanced age (see Figure 44). This result indicates that the level of Aβ deposits within the cerebral wall increases with higher age. Example images of CAA are presented in Figure 45.

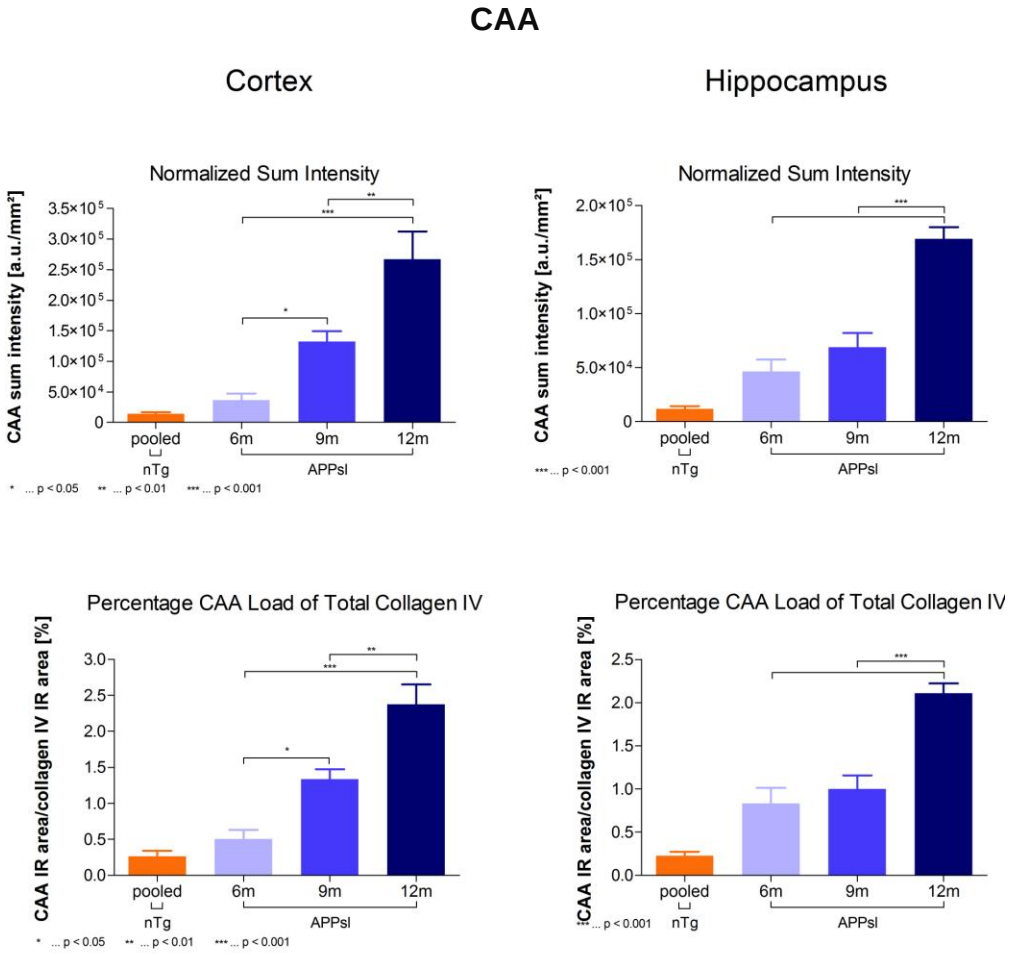

Figure 44: Graphs represent the normalized sum intensity of total CAA and the percentage of CAA load of total collagen IV in the CTX (left) and the HC (right) of nTg and 6, 9, and 12 months old APP_{SL} mice (blue bars). Data of 6, 9 and 12 months old nTg mice were averaged and presented as orange bars. APP_{SL} mice showed a significant age-associated increase of CAA. Also the percent load of 6E10 overlapping with collagen IV IR was significantly increased over age. Data are presented as means + SEM. Group size of nTg: n = 18; Group size of Tg: n = 6.

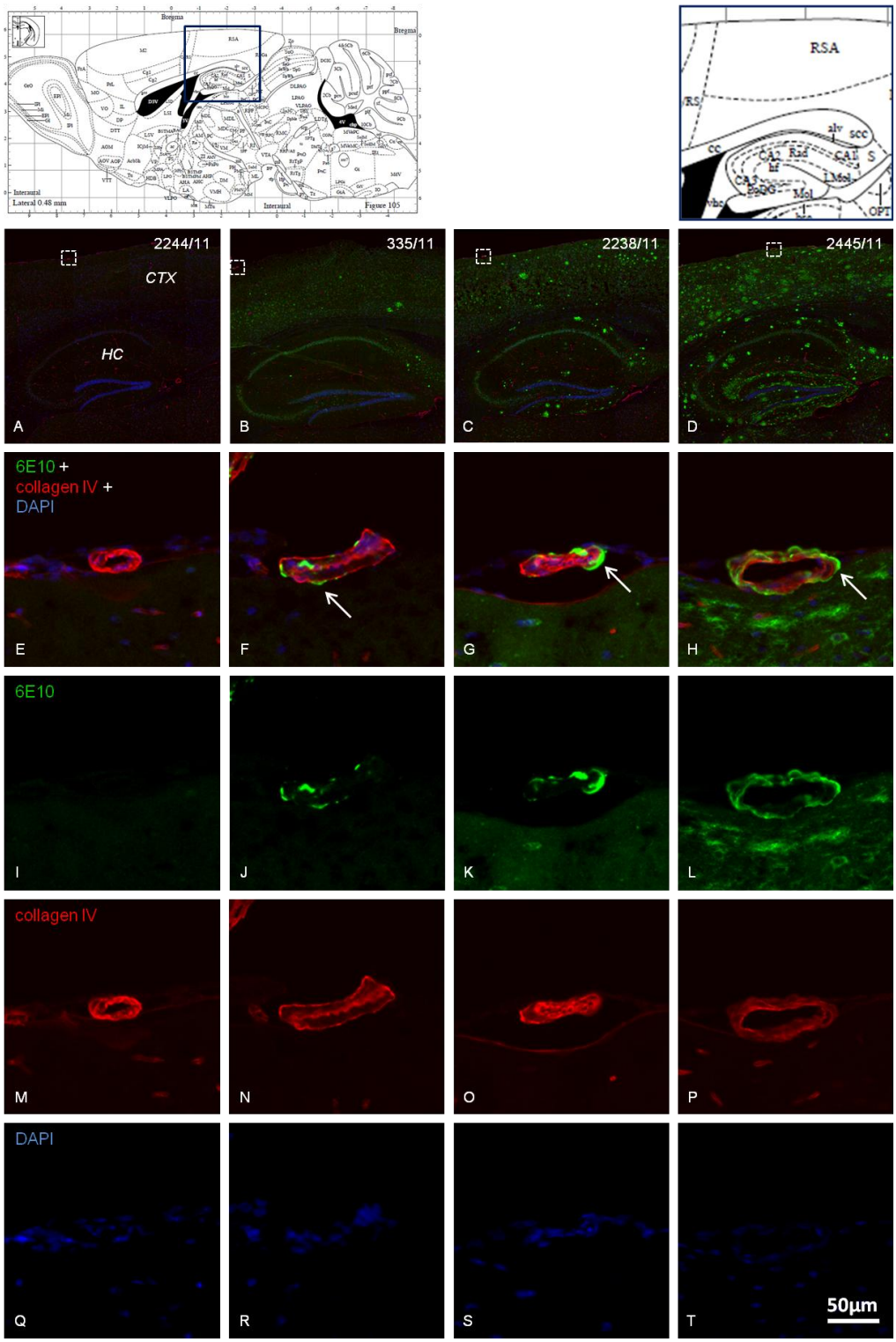

Figure 45: Images present the immunofluorescent staining of 6E10 and collagen IV and cell nuclei with DAPI. Panels show staining in one nTg (12 months, E, I, M and Q) and in 6 (F, J, N and R), 9 (G, K, O and S) and 12 (H, L, P and T) months old APP_{SL} mice, whereof magnified images display individual labeling of one representative blood vessel of each animal. A-D show merged images, whereas I-L present the 6E10 labeling, M-P the collagen IV labeling and Q-T cell nuclei with DAPI. The nTg mouse show no 6E10 IR (green, I), whereas 6E10 intensity is present in tg mice (J-L) in brain parenchyma and blood vessels (red N-P). CAA (white arrows) was age-dependently increased. Layouts on the head of the images give an overview of the coordinates of the presented images. Schemes were taken from[57]. CTX = cortex, HC = hippocampus.

3.5.2 CAA in Human Sections

One subject (IRN 1016/11) at Braak stage I/II and one at stage III/VI showed severe CAA in the occipital CTX. One subject at Braak stage V/VI had high CAA in all areas and another one had CAA in the temporal and occipital CTX. For the other subjects CAA was (nearly) not evident on parenchymal vasculature. Here it should be noted that comparable submeningeal vessels, particularly arteries were not part of the evaluation. Especially those are positive in APP_{SL} mice, thus data cannot be directly translated. Data are presented in Figure 46 and Figure 47. Representative images of IRN 02/09 are shown in Figure 48.

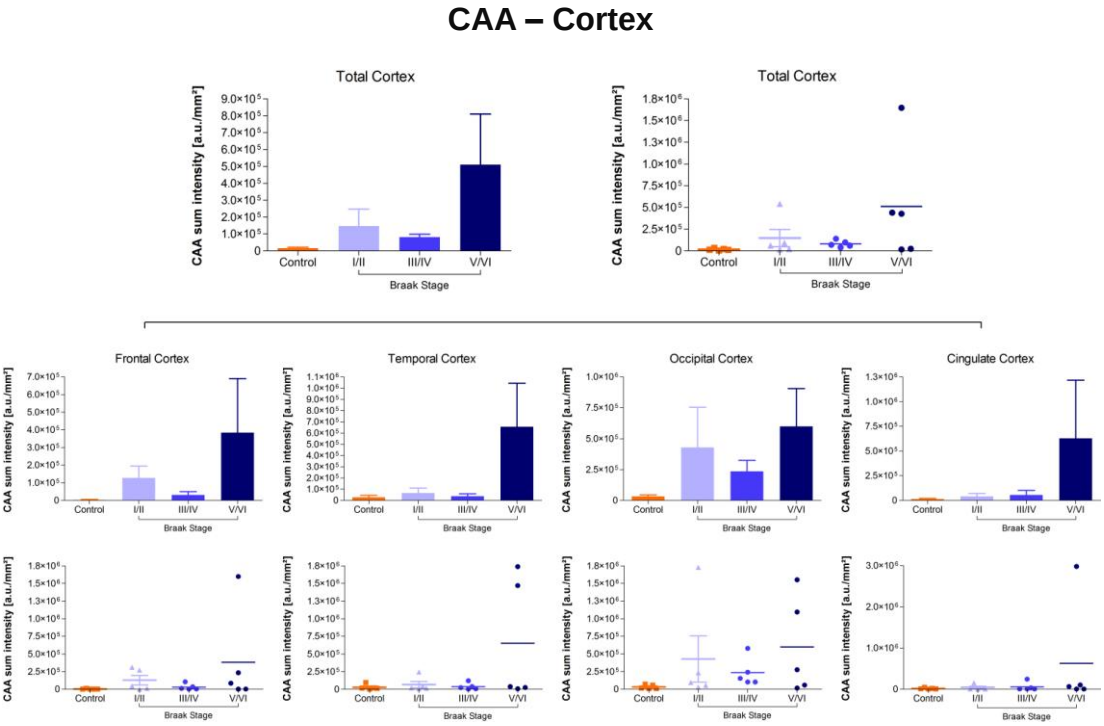

Figure 46: Quantification of CAA in total human CTX and distinct cortical areas in the control group (orange bars) versus the groups at different Braak stages (I/II, III/IV and V/VI; blue bars). Subject 1016/11 classified to Braak stage III/VI showed high levels in the occipital CTX. Subject 02/09 from Braak stage V/VI had distinct CAA in all cortical regions. Data are presented as means + SEM. Group size: n = 5.

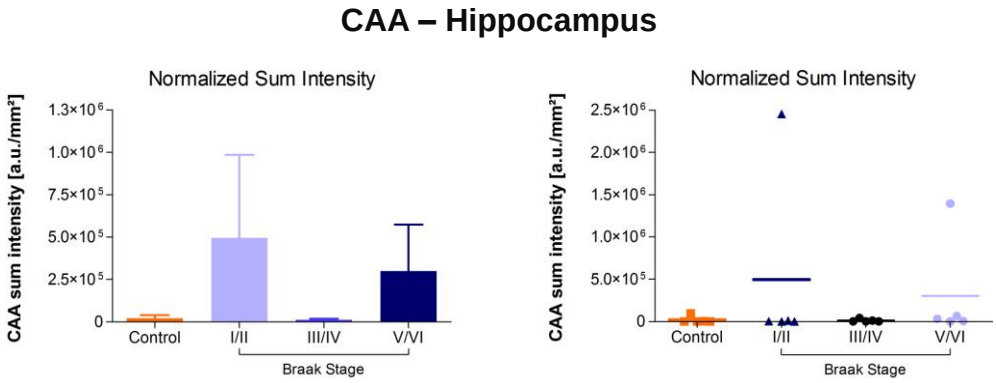

Figure 47: Quantification of CAA in the HC of the control group (orange bars) versus the AD groups at different Braak stages (I/II, III/IV and V/VI; blue bars). One person (IRN 1016/11) with a Braak stage of I/II and another one (IRN 02/09) with a stage V/VI showed distinct CAA, leading to the high standard deviation. All other subjects did not show CAA on parenchymal vasculature. Data are presented as means + SEM. Group size: n = 5.

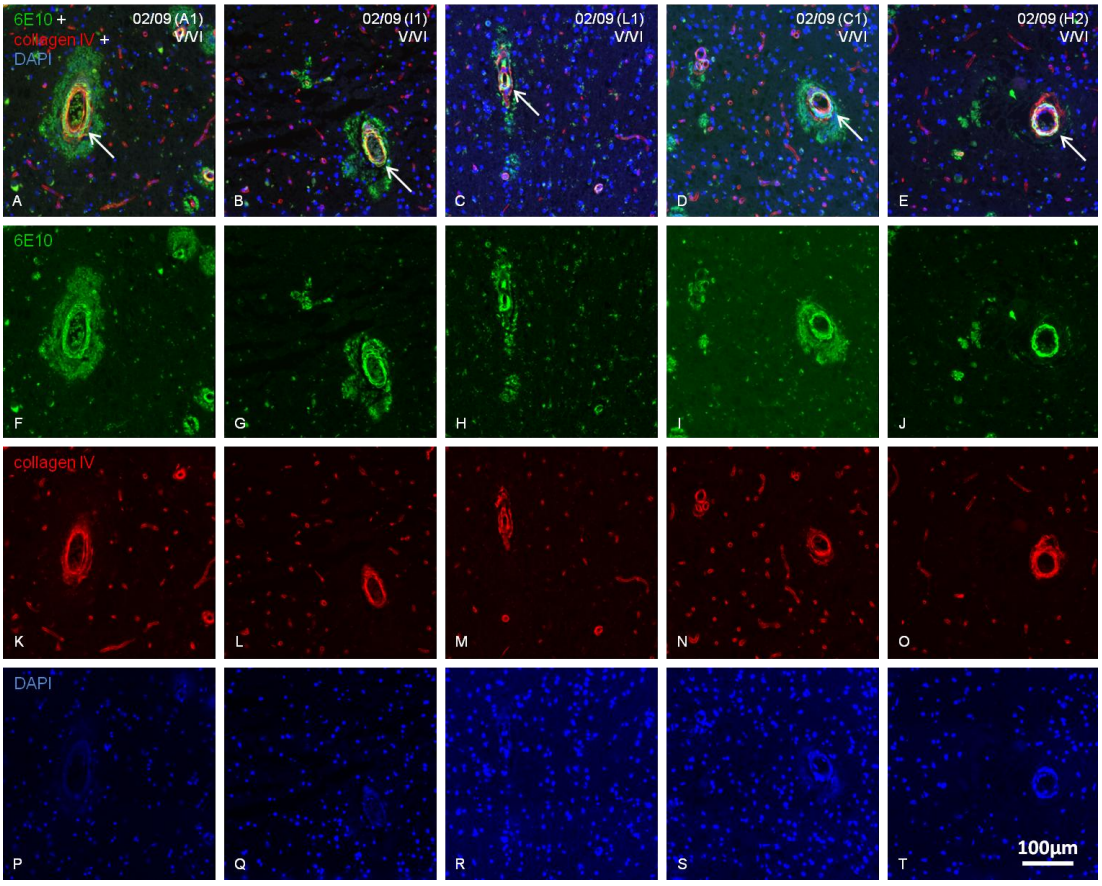

Figure 48: Example images of CAA in different cortical areas and the HC. Images of the upper row display merged pictures of the labeling with 6E10, collagen IV and DAPI in the particular investigated areas of IRN 02/09. This patient suffered from CAA (white arrows) in all investigated regions. A = frontal CTX, I = temporal CTX, L = occipital CTX, C = cingulate CTX, H = hippocampus.

3.6 Quantification of Aβ40/42

In a comparative analysis to the labeling with the anti-amyloid β antibody (clone 6E10), the total intensity of Aβ40 and Aβ42 peptides was quantified using the monoclonal human Aβ antibody (clone MOAB-2). MOAB-2 specifically recognizes the Aβ residues 1-4.

Since the antibody does not label human tissue, maybe due to the paraffin embedding of the samples, the evaluation was just performed in mice.

3.6.1 Aβ40/42 Immunofluorescence in Mouse Sections

Values in nTg mice derive from autofluorescent particles, particularly LF, a clear morphological attribute. Six months old APP_{SL} mice did not have high amounts of Aβ40/42 peptides compared to nTgs in both investigated regions. At the age of nine months, and even more at twelve months, tg mice antly (CTX: at least $p < 0.01$, HC: at least $p < 0.05$) accumulated high amounts of Aβ40/42 compared to six months old APP_{SL} mice (see Figure 49). Representative images of the immunolabeling are shown in Figure 50 (nTg) and Figure 51 (Tg).

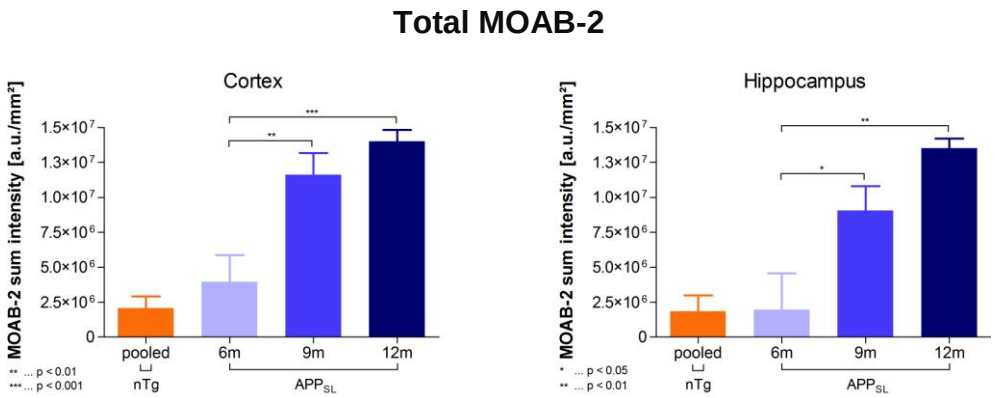

Figure 49: Graphs show normalized sum intensity of MOAB-2 immunolabeling in the CTX and the HC of nTg (orange bars) and APP_{SL} mice at different ages (6, 9 and 12 months; blue bars). In tg animals MOAB-2 signal was increased age-dependently. The values in nTg derive solely from LF, and nTgs were therefore excluded from statistic analysis. Data are presented as means + SEM. Group size of nTg: n = 18; Group size of Tg: n = 6.

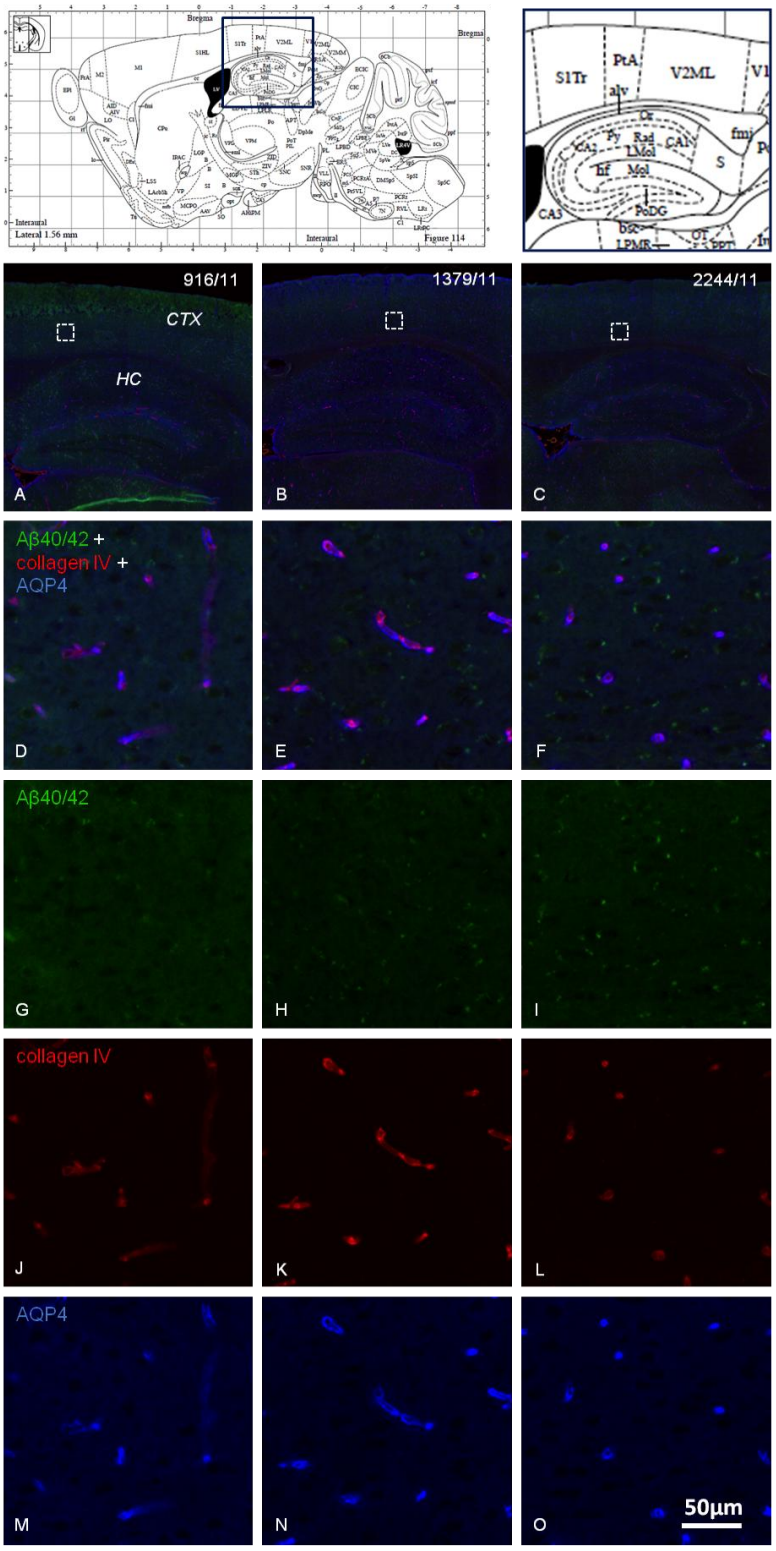

Figure 50: Triple-staining of Aβ40/42, collagen IV and AQP4 in 6 (A, D, G, J and M), 9 (B, E, H, K and N) and 12 (C, F, I, L and O) months old nTg mice. Cut-outs of each animal show no labeling of Aβ40/42 (green, G-I), a basic level of collagen IV (red, J-L) and unchanged intensity of AQP4 (blue, M-O). Layouts on the head of the images give an overview of the coordinates of the presented images. Schemes were taken from[57]. CTX = cortex, HC = hippocampus, AQP4 = aquaporin 4.

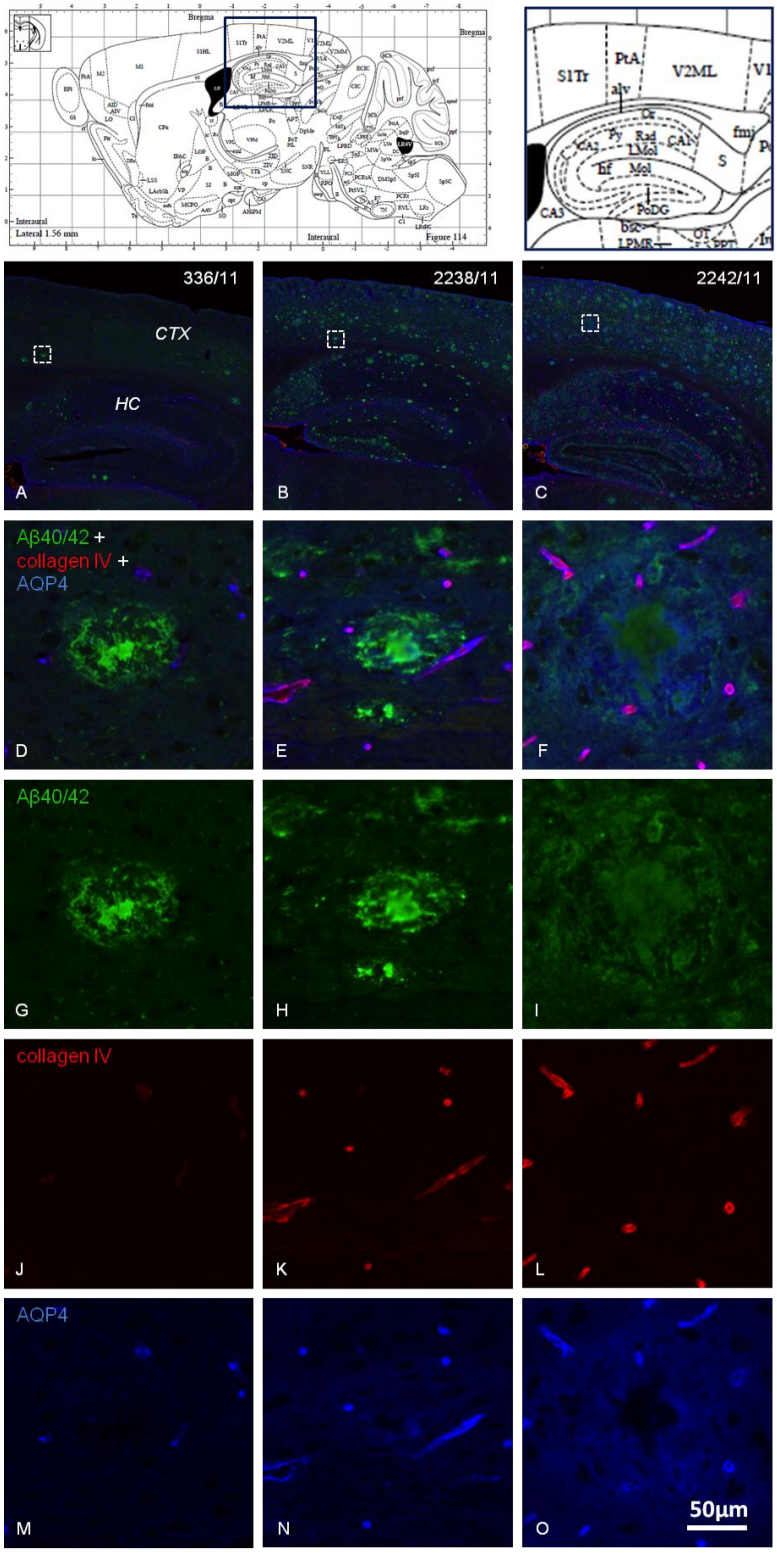

Figure 51: Aβ40/42 + collagen IV + AQP4 immunohistochemical labeling in the CTX and HC of 6 (A, D, G, J and M), 9 (B, E, H and K) and 12 (C, F, I and L) months old APP_{SL} mice. Cut-outs show the detailed merged labeling (D-F) and the individual color channels (G-O). Aβ40/42 concentration was increased with age in tg mice (green, G-I). Further vascular related AQP4 was significantly decreased with age in the HC. In the CTX a trend of lowering AQP4 was observable. The parenchymal AQP4, in contrast seems to increase in the HC, and significantly rises in the CTX. Layouts on the head of the images give an overview of the coordinates of the presented images. Schemes were taken from[57]. CTX = cortex, HC = hippocampus, AQP4 = aquaporin 4.

3.7 Quantification of AQP4

AQP4 water channels in mice and in human sections were labeled and quantified using a specific anti-AQP4 antibody. Immunofluorescence of vascular and parenchymal AQP4 was quantified separately. Representative images of the immunolabeling are shown in Figure 50 (nTg) and Figure 51 (tg).

3.7.1 AQP4 Immunofluorescence in Mouse Sections

3.7.1.1 *Total AQP4*

Tg mice showed no significant changes in normalized sum intensity of total AQP4 in any investigated region. However, a slight trend of increasing AQP4 IR in the CTX could be observed in aging APP_{SL} mice compared to coeval nTgs (see Figure 52).

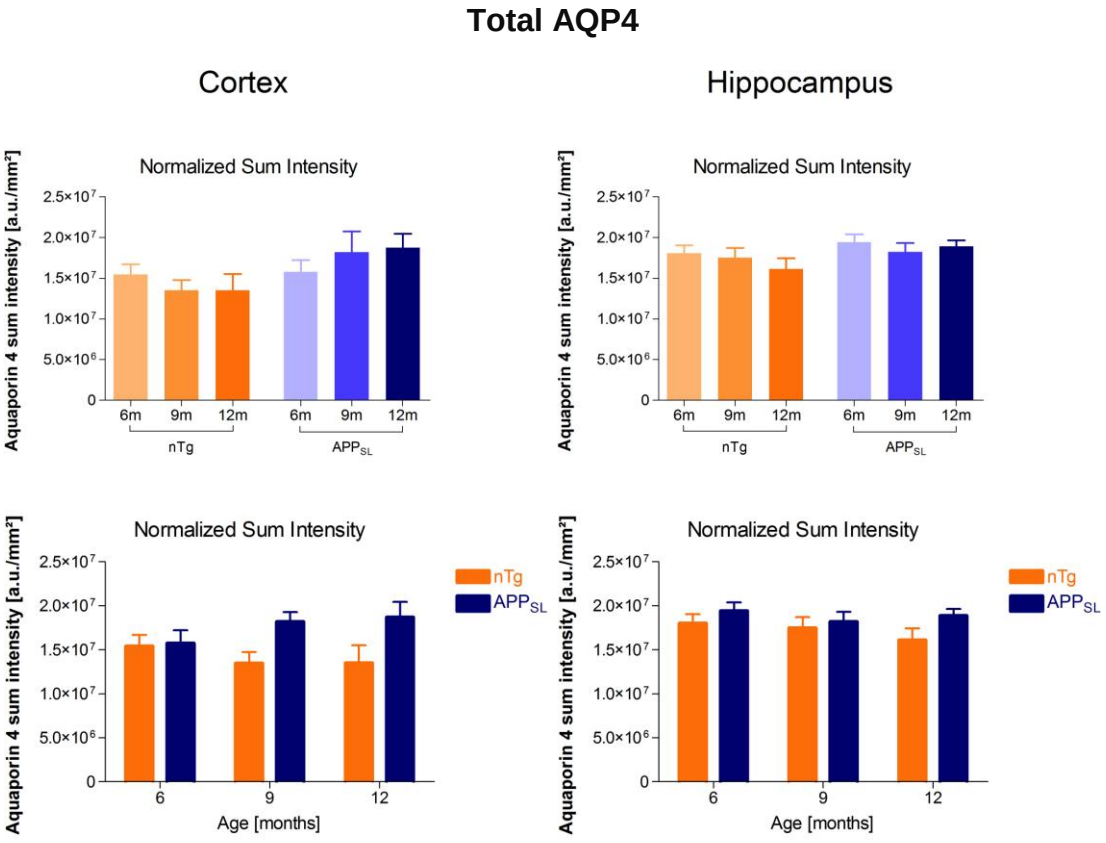

Figure 52: Graphs show normalized sum intensity of AQP4 immunolabeling in mouse sections comparing either nTg (orange bars) and tg (blue bars) animals at ages of 6, 9 and 12 months (upper graphs), or nTg and coeval APP_{SL} mice (lower graphs). A trend of increased AQP4 sum signal in the CTX of APP_{SL} mice compared to age-matched nTgs could be observed. Data are presented as means + SEM. Group size: n = 6.

3.7.1.2 *Vascular Related AQP4*

In contrast to the total AQP4 level, APP_{SL} mice had significantly ($p < 0.01$) decreased AQP4 signal in the HC at higher age and compared to coeval nTg animals ($p < 0.05$). The CTX showed only a non-significant trend towards lower AQP4 levels in tg animals compared to coeval nTg mice.

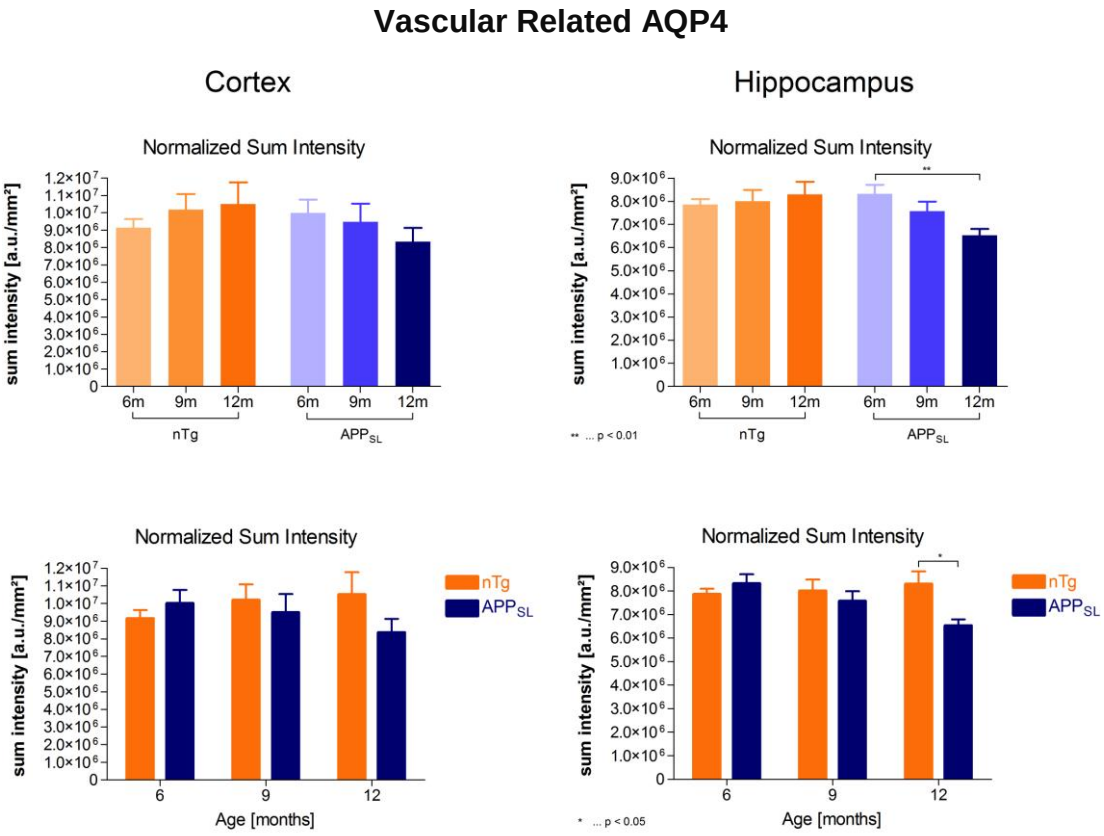

Figure 53: Graphs show the normalized sum intensity of vascular related AQP4 in the CTX (left) and HC (right) of 6, 9 and 12 months old nTg (orange bars) and APP_{SL} mice (blue bars). The sum intensity of AQP4 was significantly decreased with age in the HC in APP_{SL} mice. Additionally, sum hippocampal signal was significantly lower in the HC of 12 months old APP_{SL} mice than in age-matched nTgs. Within the CTX, the data indicates the same insignificant trend. Data are presented as means + SEM. Group size: n = 6.

3.7.1.3 *Parenchymal AQP4*

Separate to vascular AQP4, I determined the quantity of AQP4 levels in brain parenchyma. AQP4 was significantly ($p < 0.05$) reduced in twelve months old nTgs compared to six months old nTg mice. Further, the AQP4 level was significantly (at least $p < 0.05$) increased in the CTX of older APP_{SL} mice, compared to six months old tg animals. The age-matched comparison indicates that the amount of parenchymal AQP4 was significantly (at least $p < 0.01$) higher in the CTX of nine

and twelve months old APP_{SL} mice, as well as in the HC ($p < 0.05$) of twelve months old tgs (see Figure 54).

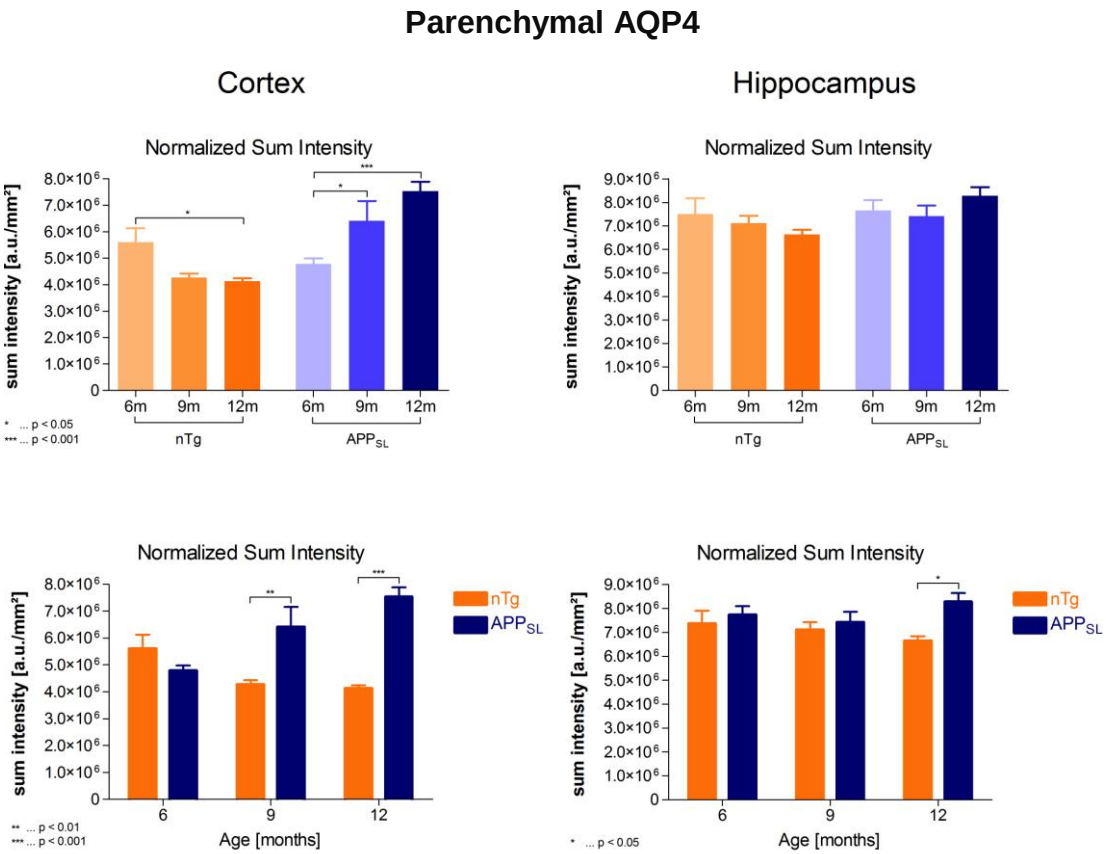

Figure 54: Graphs represent the results of the parenchymal AQP4 quantification in the CTX (left) and HC (right) of nTg (orange bars) and tg (blue bars) animals at three ages (6, 9 and 12 months). The normalized sum intensity in the CTX was significantly decreased in 12 months old nTgs compared to 6 months old nTg animals. The age-matched comparison of nTg and APP_{SL} mice showed a significant increase in parenchymal AQP4 levels. The CTX of 9 and 12 months old APP_{SL} mice had significantly higher AQP4 levels. Also the HC showed higher amounts of AQP4 in tg mice at 12 months. Data are presented as means + SEM. Group size: n = 6.

3.7.2 AQP4 Immunofluorescence in Human Sections

Evaluations in human sections also include the total AQP4 and the vascular and parenchymal AQP4 levels. Representative examples of the labeling are presented in Figure 61.

3.7.2.1 *Total AQP4*

The total AQP4 signal was not significantly altered in any human cortical region. However, the data adumbrate that the total AQP4 quantity may be lower at stage I/II compared to the control group, but increases with disease progression (see Figure 55).

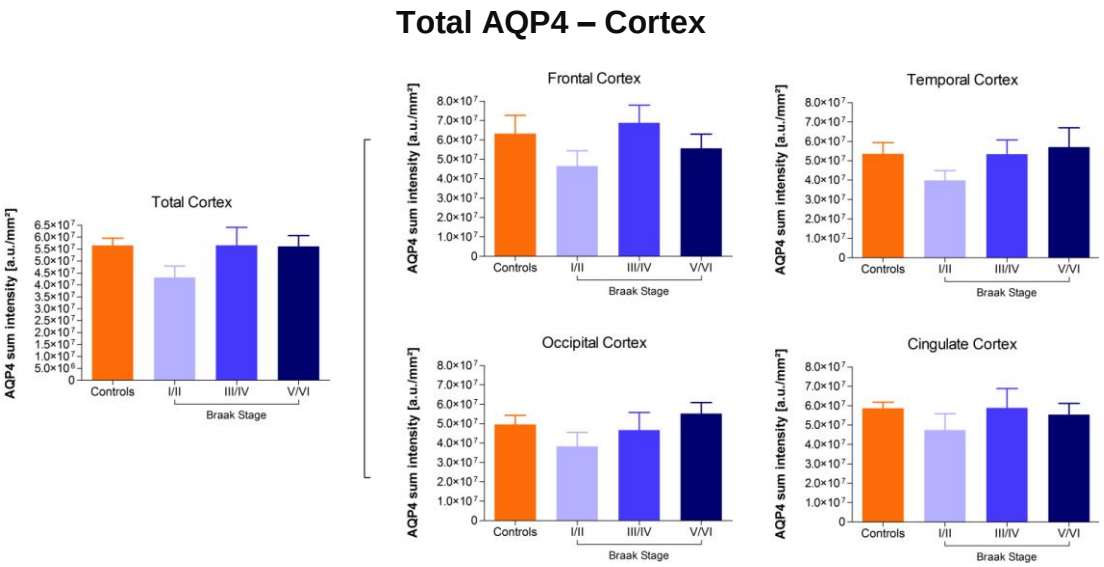

Figure 55: Quantification of total AQP4 in total human CTX and distinct cortical areas in the control group (orange bars) versus the groups of different Braak stages (I/II, III/IV and V/VI; blue bars). No statistically significant alterations in AQP4 levels could be observed. Nevertheless, the result suggests that, compared to controls, levels of AQP4 were lower at Braak stage I/II and increase in advanced Braak stages. Data are presented as means + SEM. Group size: n = 5

The total AQP4 intensity was significantly ($p < 0.05$) lower in the HC at a Braak stage of I/II compared to both the control group and Braak stage V/VI (see Figure 56). This result suggests that the intensity of AQP4 may be reduced in early AD but increases with advanced Braak stage to the level of the control group.

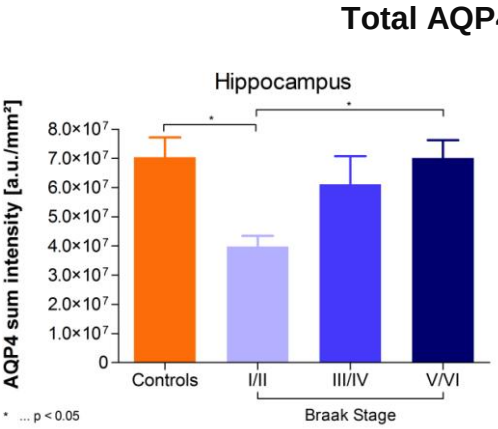

Figure 56: Quantification of total AQP4 in the HC of the control group (orange bars) versus different Braak stages (I/II, III/IV and V/VI; blue bars). The AQP4 intensity was significantly reduced in the HC at stage I/II compared to either the control group and otherwise Braak stage V/VI. Data are presented as means + SEM. Group size: n = 5.

3.7.2.2 *Vascular Related AQP4*

The quantification of cerebral blood vessel-associated AQP4 showed that only the temporal CTX features any significant ($p < 0.05$) alterations – the total AQP4 signal was lower at the Braak stage I/II compared to advanced AD stages. Results of the other cortical areas and the summarized CTX suggest that vascular AQP4 tends to increase at later stages (see Figure 57).

Vascular Related AQP4 – Cortex

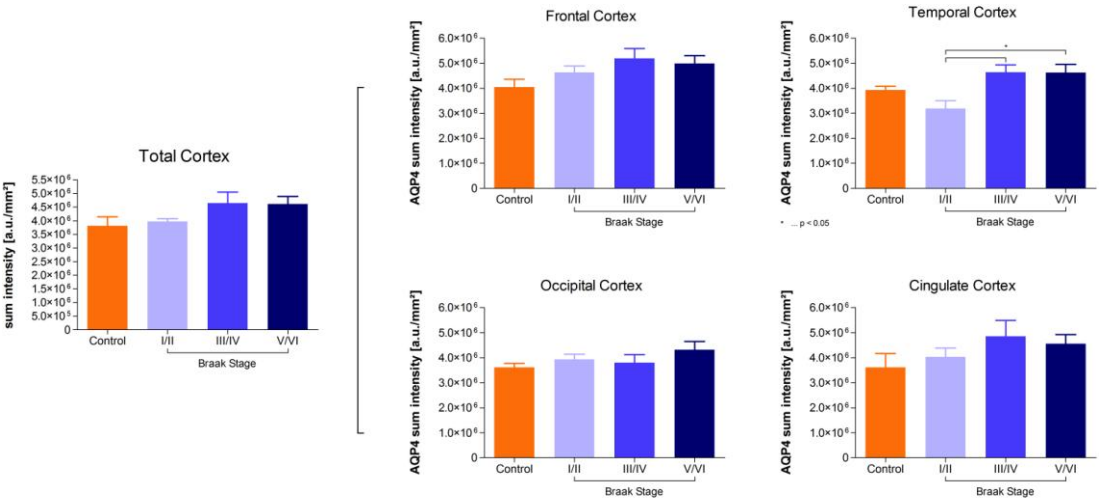

Figure 57: Quantification of vascular AQP4 in total human CTX and distinct cortical areas in the control group (orange bars) versus the groups at different Braak stages (I/II, III/IV and V/VI; blue bars). Within the temporal CTX the amount of AQP4 intensity was decreased at a Braak stage I/II in comparison to advanced stages. AQP4 intensity was not altered in other areas or in the total CTX (pooled data). Nevertheless, the result indicates that the total signal seems to increase with higher Braak stage. Data are presented as means + SEM. Group size: n = 5.

In contrast to the temporal CTX, the vascular AQP4 sum was significantly (at least $p < 0.05$) increased with advanced stages (see Figure 58).

3.7.2.3 *Parenchymal AQP4*

As in mouse sections, the amount of parenchymal AQP4 was evaluated. No significant change was detected in cortical regions, although the trend to lower AQP4 levels at early stage was also observed in the parenchyma (see Figure 59).

Vascular Related AQP4 – Hippocampus

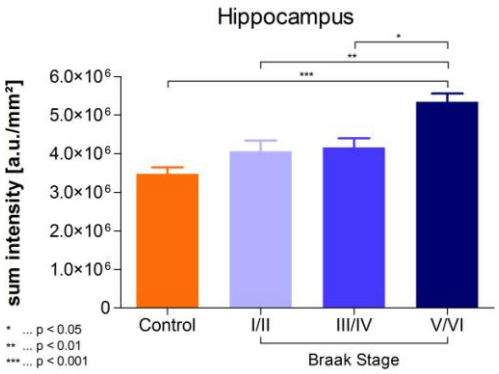

Figure 58: Quantification of vascular AQP4 in the HC of the control group (orange bars) versus the groups at different Braak stages (I/II, III/IV and V/VI; blue bars). Vascular related AQP4 was significantly increased with advanced stage. Data are presented as means + SEM. Group size: n = 5.

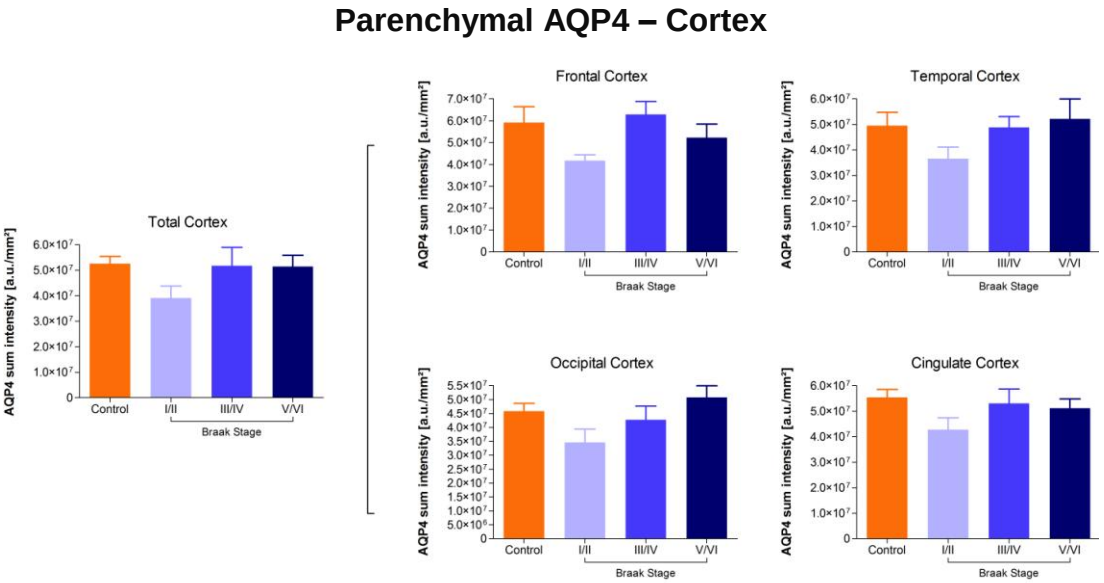

Figure 59: Quantification of parenchymal AQP4 in total human CTX and distinct cortical areas in the control group (orange bars) versus the groups at different Braak stages (I/II, III/IV and V/VI; blue bars). AQP4 was not significantly altered in human brain samples. Nevertheless the level seems to decrease at Braak stage I/II, except in the occipital CTX, and then tends to increase stage-dependently, except in the frontal CTX. Data are presented as means + SEM. Group size: n = 5.

In the HC, the intensity of parenchymal AQP4 was significantly ($p < 0.05$) decreased in comparison to the control group. At stage III/IV the signal rises and with stage V/VI it was significantly ($p < 0.01$) higher compared to early stage (see Figure 60).

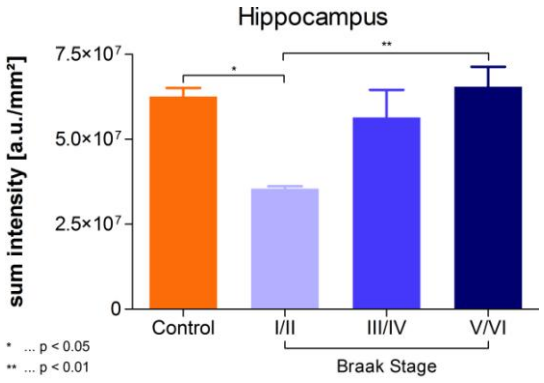

Figure 60: Quantification of parenchymal AQP4 in the HC of the control group (orange bars) versus the groups at different Braak stages (I/II, III/IV and V/VI; blue bars). At Braak stage I/II, the level of AQP4 was significantly lower than in the control group (orange bar). Thereafter, the level was significantly increased with advanced stage. Data are presented as means + SEM. Group size: n = 5.

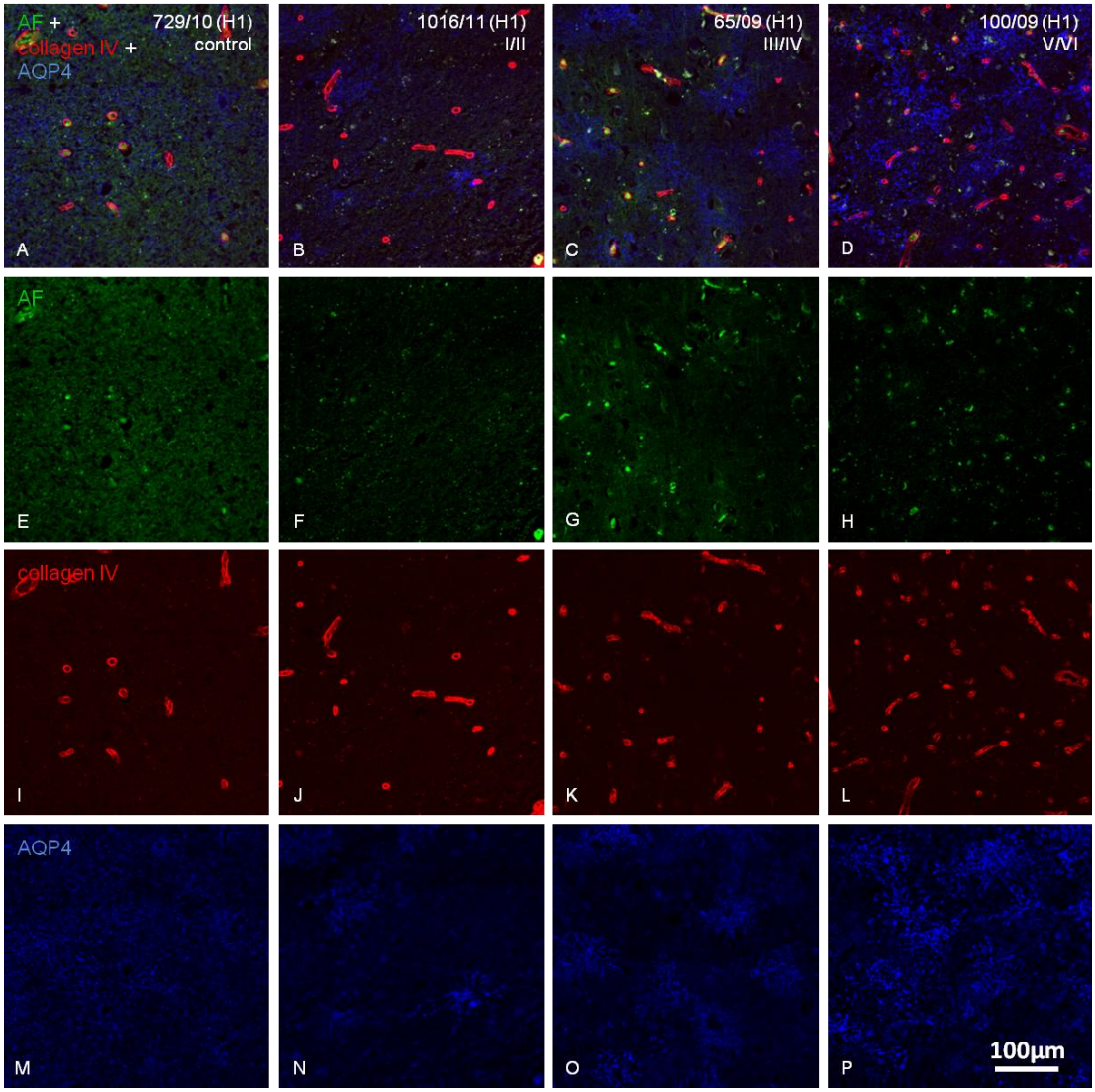

Figure 61: Representative images of the collagen IV and AQP4 immunolabeling in the HC of a control (A, E, I and M) and three different Braak stages. Control shows the basal level of collagen IV (red, I) and AQP4 (blue, M). AD patients, in contrast, had increased collagen IV IR (J-L), based on increased blood vessel density in the HC. Further, the level of vascular AQP4 was significantly decreased at early Braak stage (M-P), and the quantity of parenchymal AQP4 was lower at stage I/II, however stage-dependently increases. E-H show imaged green AF. AF = autofluorescence, H = hippocampus, AQP4 = aquaporin 4.

4 DISCUSSION

The main pathological features of AD are the occurrence of neurofibrillary tangles and amyloid plaques[6], however, significant alterations of the vascular structure are also frequent findings[59]. They come more and more into focus as probable upstream events, all the more since a vascular factor, specifically the ε4 allele of *APOE*, is so far the only common accepted genetic risk factor for AD beside the imperative effects of APP and Presenilin mutations. One of those vascular features is also cerebral amyloid angiopathy (CAA)[6], and vascular amyloid β (Aβ) deposition was therefore analyzed within this master's thesis in addition to deposition of Aβ in the brain parenchyma. Also general parameters, such as the density and the mean size of blood vessels, were determined and compared between samples of human AD cases and a mouse model for AD.

Furthermore very little knowledge exists about the role of astroglia, which are crucially involved in cerebral blood flow (local blood pressure) and homeostasis[39]. Astrocytes have a direct connection to brain vasculature via their end-feet that contain water channels such as aquaporin 4 (AQP4) enabling active water transport[39,44]. Beside this a typical feature of AD is astrogliosis, which is mainly defined by increased occurrence and high activity of astrocytes[60]. The associated chronic change of morphology may impair fundamental astrocytic functions. APQ4 distribution is consequently a matter of interest and was quantified in brain parenchyma as well as around blood vessels in a parallel approach on brain sections of both an AD mouse model and in human AD samples.

This study further investigated the feasibility and validity of a quantitative methodological approach for disease scoring, since *post mortem* analysis of human brain tissue is routinely done in numerous laboratories around the world, but procedures may differ widely between facilities. Starting with different sampling methods and variable protocols, mostly semi-quantitative analyses are performed, and the results are therefore commonly rater-dependent. These circumstances make any comparison of data difficult at least. Furthermore, any translation of findings obtained from animal models of AD is hard because, again, data from directly comparable approaches in humans and mouse models are rare. Therefore, the current study was designed to investigate and compare AD-related

histopathology in human and mouse brain samples using the same methods and rater independent analysis tools.

According to the “Amyloid Cascade Hypothesis”, deposition of Aβ is an initial event in the pathology of AD and generally represents its main pathological feature[20]. By applying the widely used 6E10 antibody, which detects human Aβ as well as full length APP and its C-terminal fragments[61], I observed that levels of insoluble 6E10-positive objects in mouse cortex (CTX) and hippocampus (HC) increase over age. This result is consistent with Havas et al.[55] who analyzed in 2012 plaque load and the relative number of plaques in APP_{SL} mice using the same antibody. Additionally, Löffler et al.[62] recently published that brain tissue of APP_{SL} mice show age-dependently increasing levels of labeling with LOC, a monoclonal antibody recognizing amyloid fibrils and fibrillar oligomers. They further reported increasing levels of Aβ40 and Aβ42 fragments analyzed with a biochemical approach (MSD™ 96-well MULTI-SPOT™ 4G8 Abeta Triplex) in samples of the CTX and the HC. Using immunofluorescence and a different antibody—MOAB-2 which selectively detects Aβ40/42—a similar increase of Aβ40/42 levels was observed in this study. In conclusion, APP_{SL} mice show a robust age-dependent increase of APP, fibrillar Aβ, Aβ40/42, and plaque load. In addition, Havas et al.[55] found that this accumulation of different amyloid species correlates with spatial memory deficits in these animals.

An early report by Davies et al.[63] concluded that immunohistological labeling of amyloid is more sensitive and therefore superior to conventional techniques such as Congo red staining or silver impregnation, since it increases the age-related prevalence of AD. The current results support these findings, even more because modern multi-channel immunofluorescence approaches allow more precise classification of histopathology by being able to easily separate Aβ on extracellular plaques from intracellular labeling of APP and amyloid species. My results also show that the detection and classification can be further refined by correcting for autofluorescence deriving from lipofuscin and other sources. Concentrating on extracellular Aβ depositions, the amount of 6E10-labeling in human CTX and HC increases with disease progression. Nevertheless, I only observed this increase of 6E10 in the HC at intermediate stage III/IV and in the isocortex at stage V/VI. This result suggests that 6E10 preferentially binds to matured Aβ and therefore can be considered as a late marker for amyloidosis in AD. Other markers, such as LOC or

Aβ antibodies also detect immature fibers and show significant increases already at early Braak stage I/II (LOC analyses were done within another project with the same subjects; data are available in the master´s thesis of Schmied 2015, unpublished).

Besides *post-mortem* analyses, different neuroimaging tools enable *in vivo* visualization of AD-associated pathological changes in the brain. For instance, magnetic resonance imaging allows the diagnosis of AD based on identifying atrophy in the entorhinal cortex and hippocampus[64]. Positron emission tomography (PET), another main neuroimaging method, enables the detection of amyloid pathology *in vivo*[65,66]. ^{11}C-PiB (Pittsburgh compound B) is currently the most widely used tracer for PET imaging, which is thought to bind to fibrillar Aβ and leads to a specific pattern in subjects with AD compared to healthy controls[67]. Recent PET studies have shown that Aβ deposition is a slow process. The accumulation of Aβ starts in the preclinical phase, increases with disease progression, and reaches a plateau at the final stage, correlating with the development of cognitive deficits[68,69,70]. However, the analyses of those publications have low correlation coefficients, non-linear regression lines and little predictability of the pertinent AD state. Cummings and Cotman[71], who—using automated quantitative immunohistochemical methods and adaptive threshold-based image analysis—already showed in 1995 that the Aβ deposition in humans correlates with dementia. Of note, the authors determined a very strong and linear correlation of Aβ load and the cognitive impairment evaluated by the Blessed IMC Test. Driscoll et al.[72] compared in 2012 ^{11}C-PiB-PET amyloid imaging with 6E10 immunohistochemistry (IHC) of *post-mortem* tissue. Both methods lead to the conclusion that Aβ load was low in the HC, was higher in the posterior cingulate gyrus, was even higher in the precuneus, and was highest in the orbitofrontal CTX and anterior cingulate CTX.

In the current study I could reproduce only some of the reported findings, such as relative low binding of 6E10 in the HC, higher concentration in stage V/VI in the frontal CTX, and the highest level in the cingulate CTX. However, no significant increase in 6E10 binding was evident in the occipital CTX. Interestingly, Thal et al.[22] reported that the distribution of Aβ in the temporal lobe is representative for the time-dependent deposition of Aβ throughout the entire brain. This result is not at all supported by our findings, since a significant increase in the temporal CTX started not until late stage V/VI compared to healthy controls and was therefore identified as the region with the latest plaque deposition and maturation. The methods used by

Driscoll et al.[72] and Thal et al.[22] differ substantially from the current approach, and this may explain many if not most of the inconsistencies: Driscoll et al.[43] used stereology for detection of plaques, but the variable size of plaques is poorly compatible with the use of stereological principles. Thal et al.[22] worked with a different amyloid marker (4G8) and used silver staining, a method that is inferior for amyloid detection[63]. Thal et al.[22] only evaluated the presence or absence of deposits but did not use parametric quantification of amyloid load.

The reported findings on CAA are also heterogenous. Generally it can be stated that defects in Aβ clearance are thought to lead to the Aβ deposition in brain parenchyma and blood vessel walls, the latter resulting in CAA[73]. In order to better understand this feature, I evaluated the rate of CAA in the CTX and HC of APP_{SL} mice and found an age-associated increase. Such findings are present in several mouse models, such as APP23 mice that also show aging-associated vascular Aβ-deposition in vessels of the pia mater, and in the thalamus, isocortex, and hippocampal formation[74]. In contrast to mice, severe CAA was only evident in a few of the investigated human subjects, and the distribution differed between individuals. One AD case showed high CAA in all isocortical areas and the HC at Braak V/VI, whereas in a second Braak V/VI subject CAA occurred everywhere except in the temporal cortex, and one early case (Braak I/II) showed strong CAA only in the occipital cortex. However, it turned out to be generally difficult to determine the occurrence of CAA, since pial and cortical arteries are predominantly affected[33] and the entire pia mater was routinely removed at the brain bank prior to embedding and sectioning of the human samples. Also the imaged region was chosen randomly, and therefore the presence of arteries in the AOI was left to chance. While at least one artery was present in all quantified images, the overall number was low and arterial CAA had little chance to be detected. The frequency of human subjects with verified CAA might therefore be underestimated, if accidentally no affected vessel was within the area of interest (AOI).

To sum these first results up, I have further characterized a mouse model that, in addition to amyloid plaques, develops cerebrovascular accumulation of Aβ. The APP_{SL} line overexpresses mutated human APP in a mouse background, and the molecular mechanisms leading to amyloid deposition in cerebral vessels in these mice may be different from the etiology of CAA in humans, because the specific

interaction of tg protein with other molecules may be altered by sequence-associated effects.

Several factors are known to contribute to AD, such as age, atherosclerosis, and hypertension[15]. These factors may potentially alter the normal blood flow and accelerate vascular Aβ accumulation. Mattson et al.[75] tested any association of Aβ levels with cerebral blood flow, and found out that higher Aβ load was related to lower cerebral blood flow in several regions, including the precuneus, entorhinal CTX and HC. Today, different hypotheses suggest that vessel pulsation supports the perivascular drainage of interstitial fluid and solutes. As blood vessels alter, the amplitude of pulsation changes and insoluble Aβ is deposited in this pathway, leading to decreased elimination of soluble Aβ. This process has two consequences: 1) vascular deposition of amyloid and 2) limited elimination of Aβ and other soluble metabolites[76]. Additionally, changes of the perivascular Aβ clearance are related to alterations in the vessel wall[77,78], leading to an abnormal BBB at least in the precapillary segment[79,80]. Different studies have indicated that in AD an up-regulation of pro-angiogenic proteins and vascular growth factors occurs[81]. Our finding indicate, that the density of blood vessels is increased in the HC at late stage AD in humans as well as the total signal of collagen IV in the basal membrane, which is in line with previous findings[82]. Since this collagen type prevents Aβ-protein fibril formation[83], increased collagen IV expression may also be part of a protective mechanism.

The present study also investigated Collagen IV in mouse and human brain samples. In contrast to humans, APP_{SL} mice show constant vascular density in the CTX and the HC. In turn, the mean size of vessels significantly increases with age in both regions, which hints at a different protective strategy when Aβ derives from a genetic overexpression. I did not find differences in vascular density in the CTX of human AD patients compared to healthy controls, which is in line with the observations by Hunter et al.[84]. However, this result is controversial to the findings of Kitaguchi et al.[43], who reported that the capillary density is decreased in the frontal and parietal CTX[85]. The authors analyzed these two regions from eight AD patients with the grid method, in which the number of vascular intersections is counted in a test grid of 400 x 400 µm; today this seems like an inadequate approach, all the more since it was found that the features of grid lines can delicately bias results. The literature is generally inconclusive, since several studies[86,85,87] also suggested a

decrease in microvascular density, while others reported an increase[88,89,90]. Variations in age, disease stage, brain region and differences in methods of analysis and investigated regions of the brain may explain the inconsistent results. It has been shown repeatedly that cerebral blood flow in AD is decreased in functional *in vivo* measures, e.g. by MRI imaging and ultrasound technologies[91,92,93,94]. It therefore seems likely that alterations in the blood circulation in AD are a robust finding and that associated changes in the density of cerebral blood vessels will likely occur. Additional research is required to elucidate the direction and extend of blood vessel-related change. The results of the current study are limited because the relevant pial and submeningeal arteries being most affected by CAA were removed during processing of the brain tissue. However, the method that was established in my project represents an objective and largely rater-independent approach that may be useful for additional investigations.

The deposition of Aβ in the vasculature is related to alterations in the BBB and probably also in water homeostasis, therefore I went on to investigate the expression and distribution of AQP4 in astrocytic end-feet of mice and humans. APP_{SL} mice and nTg controls showed no difference in total AQP4. However, in quantifications of vascular versus parenchymal AQP4 I observed that the expression of vascular AQP4 decreases with age in the HC (with a similar trend in the CTX), whereas it age-dependently increases in the brain parenchyma in both investigated regions. It has already been reported that AQP4 loses its distinctly polarized distribution in relation to blood vessels in the APPSwDI[95] and Tg-ArcSwe[96] mouse models. The reduction of AQP4, detected by quantifying overlap of astrocytic end-feet and vasculature, might result from reduced AQP4 in end-feet or from increased AQP4 expression in parenchymal membranes[45]. The easiest explanation would be astrogliosis, however.

Previous studies have shown that AQP1 and AQP4 are enhanced in accumulated reactive astrocytes at distinct lesions and in diseases such as cerebral infarction and multiple sclerosis. It has also been reported that AQP4 gets delocalized in epilepsy and traumatic brain injury[97].

With regards to AD, Pérez et al.[43] published in 2006 that AQP1 was increased at early stages. They also investigated expression of AQP4, but did not detect any alterations. In contrast to Pérez et al.[43] and the total AQP4 expression in mice, our study in human samples surprisingly showed a reduced level of parenchymal

hippocampal AQP4 at early stage I/II that returned back to baseline level at late stage V/VI. The hippocampal AQP4, in contrast, significantly increased with advanced Braak stage. Within the CTX, I could not detect any significant alterations besides a lower level of total AQP4 in the temporal CTX at stage I/II. The present results suggest that cortical AQP4 expression could be subject to dynamic regulation during the progression of AD, but higher numbers of human subjects are required to test this idea. Wilcock et al.[94] also analyzed the AQP4 level in *post-mortem* section of AD subjects and detected a reduced AQP4 level in individuals at late stage with concomitant CAA. Since they only analyzed tissue from subjects with advanced Braak stage (IV-V) there is no comparison to the early stage measured here. And in turn, since I only have a few subjects with clear CAA, I cannot compare the present data to the results from Wilcock et al.[94].

In any case, if the AQP function is impaired, the water balance may be disturbed and transport of water molecules across the BBB may be altered[98]. By today, the role of AQP4 in the perivascular space and the BBB structure is rather unexplored[44]. Considering that vascular changes are a main feature of AD and that AQPs regulate homeostasis in CNS[38], there is an essential need for further investigations on the physiology and pathology of AQPs and their role in basic astrocytic function and functional change with gliosis.

Some hints on this come from Fukuda et al.[44], who showed that the absence of AQP4 in astrocytic end-feet and the migration of astrocytes themselves to the site of injury might lead to decreased water entry into the cell, leading to decreased cell hypertrophy which results in impaired astrocytic function. This is not only important in term of homeostasis and microvascular blood flow, but also since astrocytes play an essential role in the uptake and clearance of Aβ from the brain. They are involved in Aβ clearance from the parenchyma through the BBB and also Aβ degradation[39]. With regard to the alterations of AQP4 level and localization in the human cortex at the beginning of the disease, the function of astrocytes might be impaired very early, which can consequently result in a reduced clearance from Aβ in the parenchyma and the cerebral vessels, in turn CAA and plaque deposition. On the other hand, the increase of vascular AQP4 in the human HC might be an early and fast reaction to the rising Aβ levels to quickly lower Aβ level in this brain region. It seems that this whole process is not totally translatable from mice to humans, since they consistently show an increase of parenchymal AQP4 and a decrease of

vascular AQP4 in both investigated regions. However, again the situation in the genetically engineered mice is *a priori* different and might be closer comparable to the chronic Aβ production in familiar AD.

Lastly, it should also be mentioned that astrocytes in human brain are generally larger and more complex than those of mice[99], which might as well contribute to the inequalities in AQP4 level and localization in human and mice.

5 CONCLUSION

The data collected within this master thesis are part of a larger FFG-supported research project that aims at providing specific information on the advantages and disadvantages of individual AD animal models to the customers of QPS Austria. This information is crucial to define criteria for the selection of a certain animal model (and rejection of other models) and the associated experimental readouts, considering the molecular target of a specific pharmaceutical compound.

In conclusion, the comparison of APP_{SL} mice and human samples shows that age- and stage-dependent increase of 6E10-positive amyloid load in cortical and hippocampal areas was similar. Nevertheless, not all data are translatable and not for all read-outs the method is optimal in human samples. To note, mice showed an increase of blood vessel size, whereas human tissue exhibited higher density of blood vessels. CAA was not equally well determined as in mice due to standard sampling procedures in humans that removed many potentially CAA-positive vessels. The here presented data provide first evidence that AQP4 is decreased at early stages of AD and returns to baseline level at late stage. This decrease yields the possibility that AQP4 might be used as an early marker for the diagnosis of AD. Finally, the data of AQP4 evaluation showed that the mouse model differs in some way from human AD.

Taken together the present study indicates that the APP_{SL} mouse model is a valuable tool for some aspects of AD-related research. However, it also calls for the attention that AD is a complex disease and that objective and optimized measurement procedures need to be in place to gather consistent, reproducible and reliable results. This study tries to contribute to this development and underlines that interpretations have to consider the used methods and their limitations.

REFERENCES

1. Burns, A., Byrne, E. J. & Maurer, K. Alzheimer's disease. *Lancet* **360,** 163–165 (2002).

2. Roth, M. The natural history of mental disorder in old age. *J. Ment. Sci.* **101,** 281–301 (1955).

3. Humpel, C. Chronic mild cerebrovascular dysfunction as a cause for Alzheimer's disease? *Exp. Gerontol.* **46,** 225–232 (2011).

4. Redaktion Gesundheitsportal. Öffentliches Gesundheitsportal Österreich. (2014). at <https://www.gesundheit.gv.at/Portal.Node/ghp/public/content/demenz-formen.html>

5. Takeda, S., Sato, N. & Morishita, R. Systemic inflammation, blood-brain barrier vulnerability and cognitive/non-cognitive symptoms in Alzheimer disease: relevance to pathogenesis and therapy. *Front. Aging Neurosci.* **6,** 1–8 (2014).

6. Serrano-Pozo, A., Frosch, M. P., Masliah, E. & Hyman, B. T. Neuropathological alterations in Alzheimer disease. *Cold Spring Harb. Perspect. Med.* **1,** a006189 (2011).

7. Thal, D. R. & Braak, H. Postmortale Diagnosestellung bei Morbus Alzheimer - Stadiengliederungen der kennzeichnenden Hirnveränderungen. *Pathologe* **26,** 201–213 (2005).

8. Kim, D. H. *et al.* Genetic markers for diagnosis and pathogenesis of Alzheimer's disease. *Gene* **545,** 185–193 (2014).

9. Mawrin, C. in *Kurzlehrb. Pathol.* (eds. Krams, M., Frahm, S. O., Kellner, U. & Mawrin, C.) 454 (Georg Thieme Verlag, 2010).

10. Bell, R. D. & Zlokovic, B. V. Neurovascular mechanisms and blood-brain barrier disorder in Alzheimer's disease. **118,** 103–113 (2010).

11. Steurenthaler, J. in *Dementagogik Dementiell erkrankten Menschen neu und Ganzheitl. Begegn.* (ed. Steurenthaler, J.) 35 (Springer-Verlag, 2013).

12. Tang, M. *et al.* Effect of oestrogen during menopause on risk and age at onset of Alzheimer's disease. *Lancet* **348,** 429–432 (1996).

13. Corder, E. *et al.* Gene dose of apolipoprotein E type 4 allele and the risk of Alzheimer's disease in late onset families. *Science.* **261,** 921–923 (1993).

14. Zlokovic, B. V. The blood-brain barrier in health and chronic neurodegenerative disorders. *Neuron* **57,** 178–201 (2008).

15. Farkas, E. & Luiten, P. G. . Cerebral microvascular pathology in aging and Alzheimer's disease. *Prog. Neurobiol.* **64,** 575–611 (2001).

16. Alzheimer, A. Über eine eigenartige Erkrankung der Hirnrinde. *Zeitschrift für Psychiatr. und Psych. Medizin* **64,** 146–148 (1907).

17. Braak, H. & Braak, E. Neuropathological stageing of Alzheimer-related changes. *Acta Neuropathol.* **82,** 239–259 (1991).

18. Bekris, Lynn, M., Yu, C.-E., Bird, Thomas, D. & Tsuang, D. W. Genetics of Alzheimer Disease. *J. Geriatr. Psychiatry Neurol.* **23,** 213–227 (2010).

19. Marques, F., Sousa, J. C., Sousa, N. & Palha, J. A. Blood-brain-barriers in aging and in Alzheimer's disease. *Mol. Neurodegener.* **8,** 38 (2013).

20. Armstrong, R. A. The molecular biology of senile plaques and neurofibrillary tangles in Alzheimer ' s disease. *Folia Neuropathol.* **47,** 289–299 (2009).

21. Lowe, J., Mirra, S. S., Bradley, H. & Dickson, D. in *Greenfield's Neuropathol. 2-Volume Set* (eds. Love, S., Louis, D. & Ellison, D. W.) 1047–1048 (CRC Press, 2008).

22. Thal, D. R., Rüb, U., Orantes, M. & Braak, H. Phases of A beta-deposition in the human brain and its relevance for the development of AD. *Neurology* **58,** 1791–1800 (2002).

23. Jellinger, K. A. & Attems, J. Prevalence and pathogenic role of cerebrovascular lesions in Alzheimer disease. *J. Neurol. Sci.* **229-230,** 37–41 (2005).

24. Berislav V., Z. Neurovascular pathways to neurodegeneration in Alzheimer's disease and other disorders. *Nat. Rev. Neurosci.* **12,** 723–738 (2014).

25. Zealand, N. On the mode of entry of blood vessels into the cerebral cortex. *J. Anat.* **106,** 507–520 (1970).

26. Rennels, M. & Nelson, E. Capillary innervation in the mammalian central nervous system: an electron microscopic demonstration. *Am. J. Anat.* **144,** 233–241 (1975).

27. Cohen, Z. V. I., Bonventot, G., Lacombe, P. & Hamel, E. Serotonin in the Regulation of Brain Microcirculation. *Prog. Neurobiol.* **50,** 335–362 (1996).

28. Cipolla, M. J. *Anatomy and Ultrastructure - The Cerebral Circulation*. (Morgan & Claypool Life Sciences, 2010).

29. Iadecola, C. Neurovascular regulation in the normal brain and in Alzheimer's disease. *Nat. Rev. Neurosci.* **5,** 347–360 (2004).

30. Cipolla, M. J., Li, R. & Vitullo, L. Perivascular Innervation of Penetrating Brain Parenchymal Arterioles. *J. Cardiovasc. Pharmacol.* **44,** 1–8 (2004).

31. Nishimura, N., Schaffer, C. B., Friedman, B., Lyden, P. D. & Kleinfeld, D. Penetrating arterioles are a bottleneck in the perfusion of neocortex. *Proc. Natl. Acad. Sci. U. S. A.* **104,** 365–370 (2007).

32. Zlokovic, B. V. Neurovascular mechanisms of Alzheimer's neurodegeneration. *Trends Neurosci.* **28,** 202–208 (2005).

33. Morris, A. W. J., Carare, R. O., Schreiber, S. & Hawkes, C. a. The Cerebrovascular Basement Membrane: Role in the Clearance of β-amyloid and Cerebral Amyloid Angiopathy. *Front. Aging Neurosci.* **6,** 251 (2014).

34. Wei, L. *et al.* The velocities of red cell and plasma flows through parenchymal microvessels of rat brain are decreased by pentobarbital. *J. Cereb. Blood Flow Metab.* **13,** 487–497 (1993).

35. Klein, B., Kuschinsky, W., Schröck, H. & Vetterlein, F. Interdependency of local capillary density, blood flow, and metabolism in rat brains. *Am. J. Physiol.* **251,** H1333–H1340 (1986).

36. Saunders, N. R., Ek, C. J., Habgood, M. D. & Dziegielewska, K. M. Barriers in the brain: a renaissance? *Trends Neurosci.* **31,** 279–286 (2008).

37. Wolburg, H., Noell, S., Mack, A., Wolburg-Buchholz, K. & Fallier-Becker, P. Brain endothelial cells and the glio-vascular complex. *Cell Tissue Res.* **335,** 75–96 (2009).

38. Jukkola, P. & Gu, C. Regulation of neurovascular coupling in autoimmunity to water and ion channels. *Autoimmun. Rev.* **14,** 258–267 (2014).

39. Avila-Muñoz, E. & Arias, C. When astrocytes become harmful: Functional and inflammatory responses that contribute to Alzheimer's disease. *Ageing Res. Rev.* **18C,** 29–40 (2014).

40. Xiao, M. & Hu, G. Involvement of Aquaporin 4 in Astrocyte Function and Neuropsychiatric Disorders. *CNS Neurosci. Ther.* **20,** 385–390 (2014).

41. Amiry-Moghaddam, M. & Ottersen, O. P. The molecular basis of water transport in the brain. *Nat. Rev. Neurosci.* **4,** 991–1001 (2003).

42. Verkman, a S. More than just water channels: unexpected cellular roles of aquaporins. *J. Cell Sci.* **118,** 3225–3232 (2005).

43. Pérez, E. *et al.* Aquaporin expression in the cerebral cortex is increased at early stages of Alzheimer disease. *Brain Res.* **1128,** 164–174 (2007).

44. Fukuda, A. M. & Badaut, J. Aquaporin 4: a player in cerebral edema and neuroinflammation. *J. Neuroinflammation* **9,** 279 (2012).

45. Nagelhus, E. A. & Ottersen, O. P. Physiological Roles of Aquaporin-4 in Brain. *Physiol. Rev.* **93,** 1543–1562 (2013).

46. Iliff, J. J. *et al.* A paravascular pathway facilitates CSF flow through the brain parenchyma and the clearance of interstitial solutes, including amyloid β. *Sci. Transl. Med.* **4,** 147ra111 (2012).

47. LeBleu, V. S., Macdonald, B. & Kalluri, R. Structure and function of basement membranes. *Exp. Biol. Med.* **232,** 1121–1129 (2007).

48. Mienaltowski, M. J. & Birk, D. E. in *Prog. Heritable Soft Connect. Tissue Dis.* (ed. Halper, J.) 5–29 (Springer Netherlands, 2014).

49. Hulmes, D. J. S. in *Collagen Struct. Mech.* (ed. Fratzl, P.) 16–19 (Springer Science & Business Media, 2008).

50. Epis, R. *et al.* Searching for new animal models of Alzheimer's disease. *Eur. J. Pharmacol.* **626,** 57–63 (2010).

51. Van Dam, D. & De Deyn, P. P. Animal models in the drug discovery pipeline for Alzheimer's disease. *Br. J. Pharmacol.* **164,** 1285–1300 (2011).

52. Elder, G. A., Sosa, M. A. G. & Gasperi, R. De. Transgenic Mouse Models of Alzheimer ' s Disease. *J. Medizine* **77,** 69–81 (2010).

53. Tayebati, S. K. Animal models of cognitive dysfunction. *Mech. Ageing Dev.* **127,** 100–108 (2006).

54. Rockenstein, E., Mallory, M., Mante, M., Sisk, A. & Masliaha, E. Early formation of mature amyloid-beta protein deposits in a mutant APP transgenic model depends on levels of Abeta(1-42). *J. Neurosci. Res.* **66,** 573–582 (2001).

55. Havas, D., Hutter-Paier, B., Ubhi, K., Rockenstein, E. & Crailsheim, K. A Longitudinal Study of Behavioral Deficits in an AβPP Transgenic Mouse Model of Alzheimer ' s Disease. *J. Alzheimer's Dis.* **25,** 231–243 (2011).

56. Löffler, T. *et al.* Impact of ApoB-100 expression on cognition and brain pathology in wild-type and hAPPsl mice. *Neurobiol. Aging* **34,** 2379–2388 (2013).

57. Paxinos, G. & Franklin, K. B. J. *The Mouse Brain: in Stereotaxis Coordinates.* (Academic Press, 2003).

58. https://www.studyblue.com. (2014). at <https://www.studyblue.com/notes/note/n/neuroanatomy/deck/6751100>

59. Østergaard, L. *et al.* The capillary dysfunction hypothesis of Alzheimer's disease. *Neurobiol. Aging* **34,** 1018–1031 (2013).

60. Sofroniew, M. V. & Vinters, H. V. Astrocytes: Biology and pathology. *Acta Neuropathol.* **119,** 7–35 (2010).

61. Youmans, K. L. *et al.* Intraneuronal Aβ detection in 5xFAD mice by a new Aβ-specific antibody. *Mol. Neurodegener.* **7:8,** (2012).

62. Löffler, T. *et al.* Neuroinflammation and related neuropathologies in APPSL mice: further value of this in vivo model of Alzheimer's disease. *J. Neuroinflammation* **11:84,** (2014).

63. Davies, L. *et al.* A4 amyloid protein deposition and the diagnosis of Alzheimer's disease: prevalence in aged brains determined by immunocytochemistry compared with conventional neuropathologic techniques. *Neurology* **38,** 1688–1693 (1988).

64. Adlard, P. A. *et al.* A review of β -amyloid neuroimaging in Alzheimer ' s disease. *Neuroscience* **8,** 1–23 (2014).

65. Ikonomovic, M. D. *et al.* Post-mortem correlates of in vivo PiB-PET amyloid imaging in a typical case of Alzheimer ' s disease. *Brain* **131,** 1630–1645 (2008).

66. Jagust, W. J. & Mormino, E. C. Lifespan brain activity, β-amyloid, and Alzheimer's disease. *Trends Cogn. Sci.* **15,** 520–526 (2012).

67. Vlassenko, A. G., Benzinger, T. L. S. & Morris, J. C. PET amyloid-beta imaging in preclinical Alzheimer's disease. *Biochim. Biophys. Acta* **1822,** 370–379 (2012).

68. Vlassenko, A. G. *et al.* Amyloid-Beta Plaque Growth in Cognitively Normal Adults: Longitudinal PIB Data. *Ann. Neurol.* **70,** 857–861 (2011).

69. Jack, C. R. *et al.* Brain β-amyloid load approaches a plateau. *Neurology* **80,** 890–896 (2013).

70. Villemagne, V. L. *et al.* Amyloid β deposition , neurodegeneration , and cognitive decline in sporadic Alzheimer ' s disease : a prospective cohort study. *Lancet Neurol.* **12,** 357–367 (2013).

71. Cummings, B. J. & Cotman, C. W. Image analysis of β-amyloid load in Alzheimer's disease and relation to dementia severity. *Lancet* **346,** 1524–1528 (1994).

72. Driscoll, I. *et al.* Correspondence between in vivo 11 C-PiB PET amyloid imaging and post-mortem, region-matched assessment of plaques. *Acta Neuropathol.* **124,** 823–831 (2013).

73. Love, S. Contribution of CAA to Alzheimer's disease. *J. Neurol. Neurosurg. Psychiatry* **75,** 1–4 (2004).

74. Calhoun, M. E. *et al.* Neuronal overexpression of mutant amyloid precursor protein results in prominent deposition of cerebrovascular amyloid. *Proc. Natl. Acad. Sci. U. S. A.* **96,** 14088–14093 (1999).

75. Mattsson, N. *et al.* Association of brain amyloid- b with cerebral perfusion and structure in Alzheimer ' s disease and mild cognitive impairment. **137,** 1550–1561 (2014).

76. Weller, R. O., Subash, M., Preston, S. D., Mazanti, I. & Carare, R. O. Perivascular Drainage of Amyloid- b Peptides from the Brain and Its Failure in Cerebral Amyloid Angiopathy and Alzheimer ' s Disease. *Brain Pathol.* **18,** 253–266 (2008).

77. Weller, R. O. *et al.* Cerebral amyloid angiopathy: amyloid beta accumulates in putative interstitial fluid drainage pathways in Alzheimer's disease. *Am. J. Pathol.* **153,** 725–733 (1998).

78. Utter, S. *et al.* Cerebral small vessel disease-induced apolipoprotein E leakage is associated with Alzheimer disease and the accumulation of amyloid beta-protein in perivascular astrocytes. *J. Neuropathol. Exp. Neurol.* **67,** 842–856 (2008).

79. Grinberg, L. T. & Thal, D. R. Vascular pathology in the aged human brain. *Acta Neuropathol.* **119,** 277–290 (2010).

80. Thal, D. R. The pre-capillary segment of the blood-brain barrier and its relation to perivascular drainage in Alzheimer's disease and small vessel disease. *Sci. World J.* **9,** 557–563 (2009).

81. Strozyka, D. *et al.* Contribution of vascular pathology to the clinical expression of dementia. *Neurobiol. Aging* **31,** 1710–1720 (2010).

82. Kalaria, R. N. & Pax, A. B. Increased collagen content of cerebral microvessels in Alzheimer's disease. *Brain Res.* **705,** 349–352 (1995).

83. Kiuchi, Y., Isobe, Y. & Fukushima, K. Type IV collagen prevents amyloid -β protein fibril formation. *Life Sci.* **70,** 1555–1564 (2002).

84. Hunter, J. M. *et al.* Morphological and pathological evolution of the brain microcirculation in aging and Alzheimer's disease. *PLoS One* **7,** 1–12 (2012).

85. Kitaguchi, H., Ihara, M., Saiki, H., Takahashi, R. & Tomimoto, H. Capillary beds are decreased in Alzheimer's disease, but not in Binswanger's disease. *Neurosci. Lett.* **417,** 128–131 (2007).

86. Buee, L., Hof, P. & Delacourte, a. Brain Microvascular Changes in Alzheimer's Disease and Other Dementias. *Ann. N. Y. Acad. Sci.* **826,** 7–24 (1997).

87. Paris, D. *et al.* Inhibition of angiogenesis by Abeta peptides. *Angiogenesis* **7,** 75–85 (2004).

88. Bell, M. A. & Ball, M. J. Morphometric comparison of hippocampal microvasculature in ageing and demented people: diameters and densities. *Acta Neuropathol.* **53,** 299–318 (1981).

89. Richard, E. *et al.* Morphometric Changes in the Cortical Microvascular Network in Alzheimer's Disease. *J. Alzheimer's Dis.* **22,** 811–8 (2010).

90. West, E. R., Xu, M., Woodruff, T. K. & Shea, L. D. Cardiovascular risk factors affect hippocampal microvasculature in early AD. *J. Neural Transm.* **28,** 4439–4448 (2008).

91. Roher, A. E. *et al.* Transcranial Doppler ultrasound blood flow velocity and pulsatility index as systemic indicators for Alzheimer's disease. *Alzheimer's Dement.* **7,** 445–455 (2011).

92. Alsopa, D. C., Daia, W., Grossmanb, M. & Detre, J. A. Arterial Spin Labeling Blood Flow MRI: Its Role in the Early Characterization of Alzheimer's Disease. *J. Alzheimer's Dis.* **29,** 997–1003 (2012).

93. Reiman, E. M. *et al.* Preclinical evidence of Alzheimer's disease in persons homozygous for the epsilon 4 allele for apolipoprotein E. *N. Engl. J. Med.* **334,** 752–758 (1996).

94. Roher, A., Garami, Z., Alexandrov, A., Kokjohn, T. & Esh, C. Interaction of cardiovascular disease and neurodegeneration: transcranial Doppler ultrasonography and Alzheimer's disease. *Neurol. Res.* **28,** 672–678 (2006).

95. Wilcock, D. M., Vitek, M. P. & Colton, C. a. Vascular amyloid alters astrocytic water and potassium channels in mouse models and humans with Alzheimer's disease. *Neuroscience* **159,** 1055–1069 (2009).

96. Yang, J. *et al.* Loss of astrocyte polarization in the Tg-ArcSwe mouse model of Alzheimer's disease. *J. Alzheimer's Dis.* **27,** 711–722 (2011).

97. Satoh, J. I., Tabunoki, H., Yamamura, T., Arima, K. & Konno, H. Human astrocytes express aquaporin-1 and aquaporin-4 in vitro and in vivo. *Neuropathology* **27,** 245–256 (2007).

98. Van de Haar, H. J. *et al.* Blood–brain barrier impairment in dementia: Current and future in vivo assessments. *Neurosci. Biobehav. Rev.* **49,** 71–81 (2015).

99. Oberheim, N. A., Goldman, S. A. & Nedergaard, M. Heterogeneity of Astrocytic Form and Function. *Methods Mol. Biol.* **814,** 23–45 (2012).

INDEX OF ABBREVIATIONS

2D	two-dimensional
°C	degree Celsius
%	percent
µl	microliter
µm	micrometer
µm^2	square micrometer
A	astrocyte
a.u.	arbitrary unit
Aβ	amyloid β
Aβ40	amyloid β with a size of 40 amino acids
Aβ42	amyloid β with a size of 42 amino acids
AD	Alzheimer´s Disease
AF	autofluorescence
AICD	amyloid intracellular domain
Amyg	amygdala
AOI	area of interest
Aph-1	anterior pharynx-defective 1
APOE	*apolipoprotein E*
APP	amyloid precursor protein
AQP	aquaporin
AQP4	aquaporin 4
BACE-1	β-site amyloid precursor protein cleaving enzyme 1
BBB	blood-brain-barrier
BM	basal membrane
Ca^{2+}	calcium
CA1	cornus ammonis area 1
CAA	cerebral amyloid angiopathy
Cblm	cerebellum
CBS	citrate buffered saline
Cd	caudate nucleus
CERAD	Consortium to Establish a Registry for Alzheimer's Disease
Cg	cingulate cortex
Cl	claustrum

CNS	central nervous system
CO2	carbon dioxide
CSF	cerebrospinal fluid
CTX	cortex
DAPI	4',6-Diamidino-2-Phenylindole (double stranded DNA staining)
Die	diencephalon
EC	entorhinal cortex
EOAD	early onset Alzheimer´s Disease
fi	fimbria
g	gram
GM	gray matter
gt	*guttae* (drop)
Gpe	globus pallidus externus
Gpi	globus pallidus internus
H	hippocampus
HC	hippocampus
Hipp	hippocampus
Histo-ID	histological identification
IHC	immunohistochemistry
Ins	insular cortex
IR	immunoreactivity
IRN	individual registration number
K^+	potassium
LF	lipofuscin
LOAD	late onset Alzheimer´s Disease
LRP-1	low density lipoprotein receptor-related protein 1
LRP-2	low density lipoprotein receptor-related protein 2
m	month/s
m	murine
Med	medulla oblongata
mg	milligramm
Mid	midbrain
ml	milliliter
mm	millimeter
mm^2	square millimeter

ms	millisecond/s
M.O.M.	mouse on mouse
N	neuron
n	number
n.a.	not available
NFT	neurofibrillary tangle
NIR	near infrared
nTg	non-transgenic
O2	oxygen
P	pericyte
PBS	phosphate buffered saline
Pen-2	presinilin enhancer 2
pH	*potentia hydrogenii*
Prec	precuneus
PSEN1	presenilin-1
PSEN2	presenilin-2
Put	putamen
RAGE	receptor for advanced glycation endproducts
S	subiculum
sAPPα	secreted amyloid precursor protein-α
sAPPβ	secreted amyloid precursor protein-β
SEM	standard error of mean
SMA	smooth muscle actin
tg	transgenic
VaD	vascular dementia
WM	white matter

INDEX OF FIGURES

INDEX OF TABLES